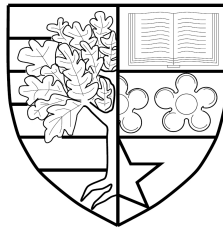# Channel Characterisation and Modelling for Transcranial Doppler Ultrasound

by

Alexander James Weir

A thesis submitted in partial fulfilment for the degree of
Engineering Doctorate

at

Heriot-Watt University
School of Engineering and Physical Sciences

September 2016

Abstract

The detection of micro-embolic signals (MES) is a mature application of transcranial *Doppler* (TCD) ultrasound. It involves the identification of abnormally high-pitched signals within the arterial waveform as a method of diagnosis and prediction of embolic complications in stroke patients. More recently, algorithms have been developed to help characterise and classify MES using advanced signal processing techniques. These advances aim to improve our understanding of the causes of cereberovascular disease, helping to target the most appropriate interventions and quantifying the risk to patients of further stroke events. However, there are a number of limitations with current TCD systems which reduce their effectiveness. In particular, improvements in our understanding of the scattering effects in TCD ultrasound propagation channels will benefit our ability to develop algorithms that more robustly and reliably identify the consistency and material make-up of MES.

This thesis explores TCD propagation channels in three related research areas. Firstly, a method of characterising TCD ultrasound propagation channels is proposed. Isotropic and non-isotropic three dimensional space (3-D) spherical scattering channel models are described in terms of theoretical reference models, simulation models, and sum of sinusoids (SoS) simulators, allowing the statistical properties to be analysed and reported. Secondly, a TCD ultrasound medical blood flow phantom is described. The phantom, designed to replicate blood flow in the middle cerebral arteries (MCA) for TCD ultrasound studies, is discussed in terms of material selection, physical construction and acoustic characteristics, including acoustic velocity, attenuation and backscatter coefficients. Finally, verification analysis is performed on the non-isotropic models against firstly, the blood flow phantom, and secondly, a patient recordings database. This analysis expands on areas of agreement and disagreement before assessing the usefulness of the models and describing their potential to improve signal processing approaches for detection of MES.

The proposed non-isotropic channel reference model, simulation model, SoS simulator, and blood flow phantom are expected to contribute to improvements in the design, testing, and performance evaluation of future TCD ultrasound systems.

I dedicate this thesis to my wonderful wife Helen, who supported me each step of the way, and our beautiful children, Isla and Malcolm.

Acknowledgements

In addition to the endless support I have received from my family, for which I am eternally grateful, completing this thesis would have been impossible were it not for the support of my supervisors, colleagues, and friends. I would like to take this opportunity to express my deepest gratitude to you all.

Firstly, I would like to thank my academic supervisor, Prof. Cheng-Xiang Wang for this opportunity. Your encouragement and guidance meant a great deal to me. I'd like to thank you for your patience throughout this journey. This subject has truly stretched my ability and determination at times, and I really appreciate your generous support and insight.

Secondly, I would like to thank my industrial supervisor Dr Stuart Parks and, the Director of Clinical Physics & Bioengineering at NHS Greater Glasgow & Clyde, Prof. David Keating. I'm deeply grateful to you both for agreeing to support my decision to embark on this study. Stuart, your compelling vision for the future of the Medical Devices Unit at NHS Greater Glasgow and Clyde instantly appealed to me. This work is offered as part of my commitment to that vision. Thank you for the advice and direction, which kept me, more or less, on track over the past five years.

To my friends and colleagues at the MDU; Robin, Stephen, Claire, Duncan, Paul, Gabriel - thanks guys! I appreciate the kind words of support and the offers of help over the years. Particularly, to those of you I frequently cornered and asked to review papers, abstracts etc. I really appreciate your assistance.

I'd also like to thank Dr Amanda Watson for sharing her knowledge and insights in all things related to medical ultrasound phantoms. My thanks also go out to Mr Walter Galbraith and Prof. Tony Gachagan at the Centre for Ultrasonic Engineering (CUE), University of Strathclyde, for lending me various equipments and for inspiring the use of synthetic grass in my phantoms. I'm not ashamed to admit, I first saw this used in the CUE water tanks at their laboratories in George Street, Glasgow.

Finally, to my wife Helen, our children, Isla and Malcolm, and the rest of my family - you frequently had to deal with my frustrations and moods, but you cheered me on and kept me going regardless. Thank you so, so much. This is for you.

Alexander Weir
Edinburgh, September 2016.

'If you only read the books that everyone else is reading, you can only think what everyone else is thinking.' Haruki Murakami, Norwegian Wood

Contents

List of Figures

List of Tables

List of Abbreviations

3-D three dimensional space

AAOA azimuth angle of arrival

ACF auto-correlation function

AFD average fade duration

AOA angle of arrival

AR autoregressive

BMF blood mimicking fluid

CCF cross-correlation function

CW continuous wave

CWT continuous wavelet transform

DAQ data acquisition

DSP digital signal processing

DWT discrete wavelet transform

EAOA elevation angle of arrival

EBR embolus to blood ratio

GBSMs geometry-based stochastic models

GPU graphics processing units

HITS high intensity transient signal

LCR level crossing rate

LoS line-of-sight

LPNM Lp-norm method of parameter computation

MCA middle cerebral arteries

MEDS method of exact *Doppler* spread

MES micro-embolic signals

MEV method of equal volume

MMEA modified method of equal area

NLA non-linear acoustic

PDF probability density function

PRF pulse repetition frequency

PSD power spectral density

PVA-C poly (vinyl alcohol) cryogel

PW pulsed wave

RBC red blood cells

RF radio frequency

RLS recursive least squares

ROC receiver operating characteristics

ROI region of interest

SE standard error

SNR signal to noise ratio

SoS sum of sinusoids

STFT short-time Fourier transform

TCD transcranial *Doppler*

TIA transient ischemic attack

TMM tissue mimicking material

VMF *Von Mises-Fisher*

WHO World Health Organisation

WSS Wide Sense Stationary

List of Symbols

c Estimated speed of sound in tissue ($1500\ ms^{-1}$).

c_s Acoustic velocity measured in TMM sample.

c_w Reference acoustic velocity measured in degassed water.

C_n Amplitude associated with the nth propagation channel.

d_n The path length associated with the nth propagation channel.

f_c Insonation frequency.

f_D Doppler frequency.

f_{D_n} *Doppler* frequency associated with the nth propagation channel.

$f_{D_{max}}$ Maximum *Doppler* frequency.

k VMF concentration parameter.

K *Rician* K-factor.

$L_\zeta(r)$ LCR of *Rayleigh* process.

$\hat{L}_{\hat{\zeta}}(r)$ LCR of simulated *Rayleigh* process.

$L_\xi(r)$ LCR of *Rice* process.

$\hat{L}_{\hat{\xi}}(r)$ LCR of simulated *Rice* process.

$m(t)$ LoS scattering component in a non-isotropic scattering channel.

$n(t)$ NLoS scattering component in a non-isotropic scattering channel.

N Number of incident scatterers.

$p_\alpha(\alpha)$ PDF of the AOA in the azimuth plane (AAOA).

$p_\beta(\beta)$ PDF of the AOA in the elevation plane (EAOA).

$p_\psi(\psi)$ PDF of the spatial AOA.

$p_\theta(\theta)$ Phase probability distribution.

$p_\xi(z)$ *Rice* amplitude distribution.

$p_\zeta(z)$ *Rayleigh* amplitude distribution.

$r_{\mu_i \mu_i}(t)$ Temporal ACF (reference).

$\hat{r}_{\hat{\mu}_i \hat{\mu}_i}(t)$ Temporal ACF (simulated).

$S_{\mu_i \mu_i}(f)$ *Doppler* PSD (reference).

$\hat{S}_{\hat{\mu}_i \hat{\mu}_i}(f)$ *Doppler* PSD (simulated).

$T_\zeta(r)$ AFD of *Rayleigh* process.

$\hat{T}_{\hat{\zeta}}(r)$ AFD of simulated *Rayleigh* process.

$T_\xi(r)$ AFD of *Rice* process.

$\hat{T}_{\hat{\xi}}(r)$ AFD of simulated *Rice* process.

z_a Acoustic impedance.

α_c Acoustic attenuation coefficient.

α_n Angle of arrival of an incident ultrasound wave in the azimuth plane.

α_0 Mean azimuth angle of arrival.

β_n Angle of arrival of an incident ultrasound wave in the elevation plane.

β_0 Mean elevation angle of arrival.

$\zeta(t)$ *Rayleigh* process.

$\xi(t)$ *Rice* process.

η Acoustic backscatter coefficient.

θ_n Phase shift associated with the n$^{\text{th}}$ propagation channel.

θ_K Phase offset, $arg\,\{m(t)\}$.

$\mu(t)$ Zero-mean *Gaussian* random process.

$\mu_i(t)$ Real *Gaussian* random process (reference).

$\hat{\mu}_i(t)$ Real stochastic process (simulated).

ρ Material density.

σ Standard deviation (SD), the dispersion of a set of values.

σ^2 Variance, how far a set of values are spread out from their mean.

τ_n Time delay associated with the n$^{\text{th}}$ propagation channel.

ψ_n The spatial angle of arrival, formed between the incident ultrasound wave and the direction of motion of blood flow.

Glossary

A-mode Amplitude mode is the simplest type of ultrasound system. A single transducer scans a line through a region of interest (ROI). The echoes are plotted on a screen to produce an image. The image has depth information on one axis and received echo amplitude on the other. 10

axial resolution This is the minimum reflector separation required along the direction of sound travel (along the scan line) to produce separate echoes. Axial resolution is equal to one half the spatial pulse length, i.e. $(n\lambda)/2$. 38

B-mode Brightness mode uses a linear array of transducers to simultaneously scan a plane through a ROI. The pulse from each transducer in the array creates a scan line. Along this scan line, the encoded brightness is proportional to the amplitude of the returned echo as the depth increases. By combining multiple scan lines, where each scan line is a one-dimensional image, a two dimensional image is created. 10

circle of Willis Named after the 17th century physician and neuroanatomist, this term is used to describe the system of arteries formed near the centre of the base of the brain. 15

embolism An obstruction or blockage in a blood vessel caused by an embolus while traveling through the bloodstream. 1

embolus A blood clot, gas bubble, piece of fatty deposit, calcified plaque, or other object which has been carried in the bloodstream to lodge in a vessel and cause an embolism, pl. emboli. 5

erythrocytes Red blood cells. They are biconcave and discoidal. They are approximately 8 μm in diameter and 2 μm thick. 14

haemodynamics The study of the movement and forces of circulating blood flows. 11

infarcation The process of tissue damage and death due to the lack of blood flow and the resulting shortage of oxygen and glucose. 1

insonate To expose to ultrasound waves. 15

ischemia A restriction or blockage of the vascular system leading to a reduction in blood and a shortage of oxygen and glucose resulting in tissue damage. 1

leukocytes White blood cells. These are approximately spherical and 5 to 20 μm in diameter. 14

M-mode Motion mode is derived from a B-Mode scan. It captures a ROI corresponding to a single scan line which is displayed relative to time so that tissue along the ROI can be seen to change over time. 18

mechanical index The mechanical index (MI) is proportional to an ultrasound beam's peak negative pressure. It is an indication of an ultrasound beam's ability to cause cavitation-related bio-effects (micro mechanical damage). A higher mechanical index means a larger bio-effect. 38

plasma A clear yellow cell-free fluid that contains no objects bigger than platelets cells that are approximately 1 to 3 μm in diameter and are responsible for the clotting reaction in blood. 14

platelets Discoid or irregularly shaped, colourless, refractile bodies, much smaller than red blood cells. 14

rheography A method used to analyse blood flow by recording fluctuations in resistance of a region of the body under ultrasonic insonation. 11

stenosis An abnormal narrowing in a blood vessel. 17

thrombosis A blood clot. The final product of blood coagulation in the haemostasis process in which the bleeding process stops and the blood changes from a fluid to a solid state. 22

Chapter 1

Introduction

1.1 Background & Motivation

Stroke, or cereberovascular disease, is the term used to describe the effect when blood flow in a localised region of the brain is interrupted by ischemia, a blockage of the vascular system caused by an arterial embolism, or blood loss due to haemorrhage. If part of the brain is deprived of blood, brain cells are damaged or die due to a combined lack of oxygen and glucose. This can lead to infarction and may result in a number of different possible effects, most of which are significantly life changing, depending on the part of the brain affected and the amount of brain tissue that is damaged.

In 2004, the World Health Organisation (WHO) stated that stroke is the third most common cause of death in developed countries, exceeded only by coronary heart disease and cancer [1]. It went on to estimate that globally, 5.5 million people die from stroke each year and a similar number are permanently disabled. Further, it was estimated that in the USA, someone dies of a stroke every three minutes. A staggering statistic.

In Scotland, stroke is one of the most common causes of death, behind cancer, heart disease, and respiratory system disease. The Registrar General's Annual Review of Demographic Trends in 2009 examined the most common causes of death

1

in Scotland (summarised in Table 1.1) and found that cereberovascular disease accounts for approximately 10% of the total number of deaths each year [2]. There are approximately 13,000 strokes in Scotland each year. Of these approximately 3,000 are in someone under 65 and one third of the total number of strokes will result in death. Stroke is the greatest single cause of severe disability in adults in Scotland.

Table 1.1: The most common causes of death, Scotland, 2009 [2].

Causes of Death	% of All deaths	All age groups
All cancers	31.78%	15,187
Trachea, bronchus and lung	8.68%	4,147
Bowel	3.30%	1,578
Breast	2.11%	1,010
Lymphoid, haematopoietic etc.	2.06%	986
Urinary tract	1.72%	821
Oesophagus	1.56%	746
Prostate	1.65%	790
Pancreas	1.45%	691
Stomach	1.12%	535
Other cancers (e.g. bladder, liver)	8.13%	3,883
Ischemic heart disease	17.31%	8,274
Respiratory system diseases	14.91%	7,125
Cereberovascular disease	**10.27%**	**4,906**
Mental & behavioural disorders	6.96%	3,327
Diseases of the digestive system	6.29%	3,006
Diseases of the nervous system	3.46%	1,652
Accidents	2.79%	1,332
Diseases of the genitourinary system	2.66%	1,269
Endocrine, nutritional and metabolic diseases	1.83%	873
Certain infectious and parasitic diseases	1.75%	838
Total deaths		47,789

As well as the physical cost of stroke, the financial costs are also thought to be significant but notoriously difficult to estimate accurately. In Europe in 2010 the cost has been estimated at €64.1 billion [3]. In the UK in 2008-09, the National Audit Office estimated the direct care cost of stroke was at least £3 billion annually in England alone [4], within a wider economic cost of about £8 billion once indirect costs are considered, and it is likely that it incurs proportionate amounts in Scotland, Wales and Northern Ireland. In terms of hospital occupancy, stroke patients occupy around 20% of all acute hospital beds and 25% of long term stay beds [5].

It is against this background that prevention of stroke has been the key focus behind the progress made in the ultrasound evaluation of cereberovascular disease during the last thirty years. Yet there is still significant untapped potential in such systems as we explore and apply new methods of signal analysis and machine learning with the potential to offer greatly improved risk evaluation, particularly in asymptotic patients.

1.2   Aims & Objectives

The main topic of this thesis is TCD ultrasonography, a method of *Doppler* ultrasound that was first described by *Aaslid et al* in 1982 [6]. *Aaslid* discovered that low frequency (2 MHz) ultrasound could be used to perform non-invasive investigations of the intra-cranial arterial system by insonating an area where the temporal bone thins. This made it possible to detect ultrasound reflections of blood flow from which haemodynamic information could be derived. Using this technique, blood flow velocities (mean flow velocity, peak systolic flow velocity, and end-diastolic flow velocity) in the middle cerebral arteries can be studied, the cerebral CO_2 reactivity can be derived and, most importantly for this study, MES can be detected. The details of this process are described in more detail in Chapter 2.

The aim of this thesis is to build upon existing research involving the detection and

characterisation of cerebral micro-embolus by exploring TCD ultrasound propagation channels in three related research areas; namely the development of theoretical channel models and corresponding simulation models for TCD ultrasound propagation channels, the development of a blood flow phantom for TCD studies, and the verification of simulations with measured results from a patient recordings database.

In the first of these research areas, a method of characterisation of a TCD ultrasound propagation channel is proposed. Isotropic and non-isotropic 3-D spherical scattering channel models are described in terms of theoretical models, simulation models, and SoS simulations, allowing the spatial-temporal statistical properties to be analysed and reported.

In the second research area a TCD ultrasound medical blood flow phantom is described. The blood flow phantom, designed to replicate the human physiology associated with blood flow in the MCA for TCD ultrasound studies, is discussed in terms of material selection, physical construction and acoustic characteristics, including acoustic velocity, attenuation and backscatter coefficients.

Finally, the third research area provides verification analysis for the non-isotropic models against firstly the blood flow phantom, then secondly a patient recordings database. The analysis expands on areas of agreement and disagreement before assessing the usefulness of the models and describing the potential to improve signal processing approaches for detection, classification, and characterisation of MES. The proposed channel models and blood flow phantom are expected to contribute to improvements in the design, testing, and performance evaluation of future TCD ultrasound systems, leading to the development of an ambulatory TCD ultrasound system that is capable of improved automatic micro-embolus detection. In particular, it is hoped this project will lead to the development of 3-D scattering channel models that can be used to develop and improve algorithms for classifying micro-emboli detected by TCD ultrasound systems by investigating and, where appropriate, combining existing techniques using a combination of signal processing methods,

including statistical signal analysis based on machine learning.

1.3   Contributions & Original Publications

This thesis explores TCD propagation channels in three related research areas. Firstly, a method of characterising TCD ultrasound propagation channels is proposed. Isotropic and non-isotropic three dimensional (3-D) spherical scattering channel models are described in terms of theoretical reference models, simulation models, and sum of sinusoids (SoS) simulators, allowing the statistical properties to be analysed and reported. Secondly, a TCD ultrasound medical blood flow phantom is described. The phantom, designed to replicate blood flow in the middle cerebral arteries (MCA) for TCD ultrasound studies, is discussed in terms of material selection, physical construction and acoustic characteristics, including acoustic velocity, attenuation and backscatter coefficients. Finally, verification analysis is performed on the non-isotropic models against firstly, the blood flow phantom, and secondly, a patient recordings database. This analysis expands on areas of agreement and disagreement before assessing the usefulness of the models and describing there potential to improve signal processing approaches for detection of MES.

The key contributions of the thesis are summarised as follows:

i. **3-D non-isotropic spherical theoretical reference model, simulation model, and a corresponding SoS channel simulator:** A new method of characterisation of a TCD ultrasound propagation channel has been proposed; based on 3-D non-isotropic spherical scattering channel models. This work includes mathematic derivations of the statistical properties, in terms of the amplitude probability density function (PDF), phase PDF, temporal auto-correlation function (ACF), *Doppler* power spectral density (PSD), envelope level crossing rate (LCR) and average fade duration (AFD).

ii. **A new flow phantom for TCD ultrasound studies:** A novel wall-less *Doppler* flow phantom has been designed for analysis of the 3-D TCD ultrasound channel model. The flow phantom can synthesise blood flow and

occurrences of micro-emboli within the MCA as a result of cerebrovascular disease.

iii. **Verification of the 3-D non-isotropic TCD ultrasound propagation channel models:** A patient measurements database has been created for verification of the channel models. The 3-D non-isotropic spherical channel models have been optimised and fitted to the statistical average of the patient measurements database.

The work presented in this thesis has led to the following publications:

Referred Journals Papers

1. **A.J. Weir**, C-X. Wang, and S. Parks, "Novel 3D Stochastic Propagation Channel Models for Transcranial *Doppler* Ultrasound", *IEEE-UFFC Transactions on Ultrasonics, Ferroelectrics and Frequency Control*, submitted for publication.

Referred Conference Papers

2. **A.J. Weir**, C-X. Wang, and S. Parks, "3-D Half-Spheroid Models for Transcranial *Doppler* Ultrasound Propagation Channels", *IEEE-EMBS International Conference on Biomedical and Health Informatics*, June 1-4, 2014, Valencia, Spain, pp. 728–731.

3. **A.J. Weir**, R. Sayer, C-X. Wang, and S. Parks, "A wall-less poly (vinyl alcohol) cryogel flow phantom with accurate scattering properties for transcranial *Doppler* ultrasound propagation channels analysis", *Engineering in Medicine and Biology Society (EMBC), 2015 37th Annual International Conference of the IEEE*, August 25-29, 2015, Milan, Italy, pp. 2709–2712.

4. **A.J. Weir**, C-X. Wang, and S. Parks, "Pre-clinical investigations of multipath propagation in transcranial *Doppler* ultrasound flow phantom", *Engineering in Medicine and Biology Society (EMBC), 2016 38th Annual International Conference of the IEEE*, August 16-20, 2016, Orlando, USA, pp. 3586–3589.

1.4   Thesis Organisation

The remainder of the thesis is organised as follows:

Chapter 2 provides an introduction to *Doppler* ultrasound and its use as a non-invasive modality for the interrogation and monitoring of blood flow in the intra-cranial arterial system. It describes the detection algorithms used for micro-embolic signal detection, discusses the challenges of performing long term ambulatory monitoring of the MCA, and provides a summary of existing medical ultrasound modelling techniques. The motivation and research gaps are addressed in this chapter.

Chapter 3 investigates 3-D isotropic spherical scattering channel models for TCD ultrasound, including the characteristics and statistical properties; amplitude and phase PDFs, temporal ACF, *Doppler* PSD, envelope LCR and AFD. In this chapter, a theoretical reference model, simulation model, and SoS simulator are defined. The usefulness and limitations of this approach are discussed.

Chapter 4 extends the investigations of Chapter 3 by defining 3-D non-isotropic spherical scattering channel models for TCD propagation channels, including the characteristics and statistical properties; amplitude and phase PDFs, temporal ACF, *Doppler* PSD, envelope LCR, and AFD. These models will form the basis of the comparison with the flow phantom and patient measurements in Chapter 6.

Chapter 5 describes a flow phantom for TCD ultrasound studies, detailing the design and measurement results, to include acoustic velocity, attenuation and backscatter coefficients.

Chapter 6 introduces an information governance approved patient recordings database and provides comparison of the 3-D non-isotropic spherical scattering channel models, flow phantom, and patient measurements in terms of the amplitude and phase PDFs, ACF, LCR, and AFD. The discussion will expand on areas of agreement and

disagreement before assessing the usefulness of the model and its potential applications for further study of TCD.

Finally, Chapter 7 concludes the thesis and gives some suggestions for future research topics.

Chapter 2

Principles of Transcranial *Doppler* Ultrasound

2.1   Introduction

Ultrasound is an imaging modality that uses piezoelectric crystal transducer(s) to transmit and receive sound waves between 1 MHz and 12 MHz, well above the audible frequency range of humans (below 20 kHz). At these high frequencies, sound waves act more like electromagnetic waves; they propagate in straight lines and reflect off objects or tissue interfaces in their path. The strength of reflection is dependent on a number of factors; the frequency of transmission, the acoustic impedance of the medium at the object or tissue interface, and the depth (distance) of the reflection from the transducer.

There are many types of ultrasound system. Although ultrasound was originally developed as a medical imaging modality, it has emerged in many other applications; for example, material science and industry for inspection and non-destructive testing. Early ultrasound imaging systems were simple A-mode systems which provided depth information on one axis and received echo amplitude on the other. These progressed to more familiar B-mode systems which generate a two-dimensional image using a linear array of transducers to simultaneously scan a plane through a ROI. Along this scan line, the encoded brightness is proportional to the ampli-

tude of the returned echo as the depth increases. By combining multiple scan lines, where each scan line is a one-dimensional image, a two dimensional image is created.

Doppler ultrasound and colour flow imaging have emerged more recently. These methods differ from standard methods of ultrasonography in that they provide information of function of the insonated region rather than a simple two-dimensional image. This is achieved by analysing the phase and frequency of the reflected pulse using the *Doppler* effect. However, like the more traditional forms of ultrasound, the same fundamental rules of sound wave propagation and reflection are applicable.

2.2 History: The *Doppler* Effect

The *Doppler* effect (or *Doppler* shift) was named after *Christian Andreas Doppler* (1803–1853), an Austrian mathematician and physicist. In his famous paper *"Uber das farbige Licht der Doppelsterne"* (on the coloured light of double stars) published in 1843 [7], *Doppler* introduced the idea that the observed frequency of light from a source can change relative to the velocity of the observer and vice-versa. In appendix (A.1) the expression for the *Doppler* frequency (f_D) in an ultrasound system is derived as

$$f_D = \left(\frac{2v_o \times \cos(\theta)}{c} \right) \times f_c \qquad (2.1)$$

from classical physics theory (A.12), where v_o becomes the velocity of blood flow, c is the velocity of sound in the medium, θ is the insonation angle, and f_c is the insonation frequency. Equation (2.1) is used as the foundation of analysis of the *Doppler* effect in ultrasound systems.

2.3 *Doppler* in Medical Ultrasound

Doppler ultrasound involves a group of ultrasound techniques that use the *Doppler* effect to image moving tissue and blood flow velocity. The use of *Doppler* ultrasound to measure blood flow velocity was first established in the 1960s [8] as part of pioneering work studying haemodynamics using rheography and has since become

an important tool for the measurement and analysis of haemodynamics in a wide range of clinical applications.

2.3.1 Obtaining Ultrasound images of blood flow

Ultrasound images of blood flow are obtained from measurements of movement. Fig. 2.1 shows a simple view of *Doppler* ultrasound measurement of blood flow in a vessel. The ultrasound beam is transmitted by a transducer. In the simplified model presented, echoes received from stationary tissue can be considered to exhibit the same frequency and phase as the transmitted signal. Echoes from scatterers (i.e. moving tissue and fluids) will exhibit slight differences in the time and/or phase. From these differences the '*Doppler*' frequency difference is obtained which can then be processed to produce either a colour flow display or a *Doppler* sonogram.
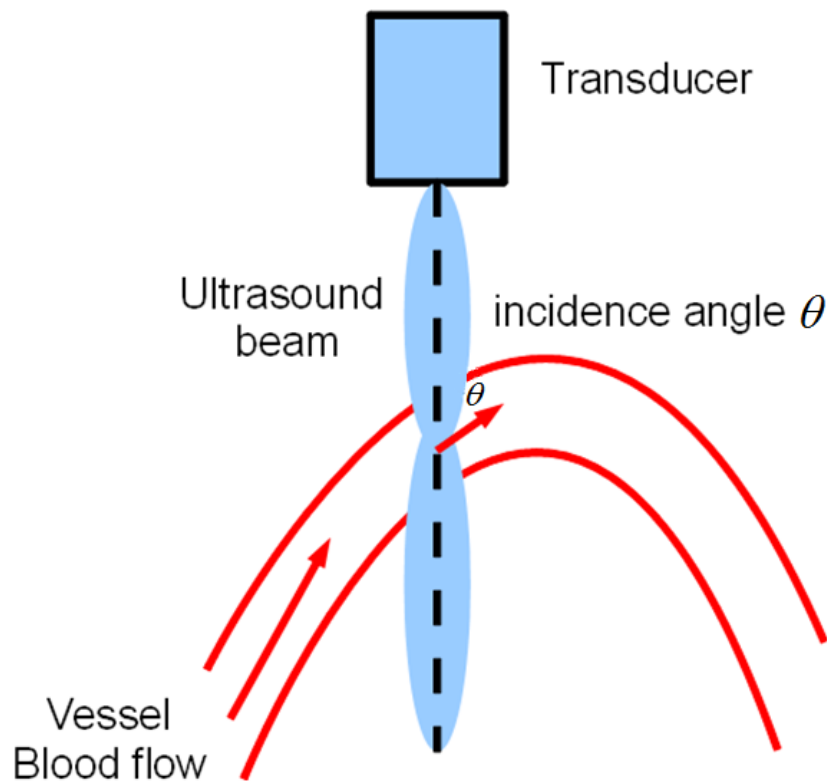
Figure 2.1: *Doppler* ultrasound measurement of blood flow.

As the *Doppler* frequency equation shows (2.1), in order to detect blood flow, there has to be flow within the direction of the ultrasound beam. If the incidence angle of the ultrasound beam is orthogonal to the flow, no relative motion can be detected. If the incidence angle is less than 90°, the blood flow detected will be towards the direction of insonation and the *Doppler* frequency change detected will be positive relative to the transmit frequency, i.e. greater than the transmit frequency. Conversely, if the incidence angle is greater than 90°, the blood flow detected will be away from the direction of insonation and the *Doppler* frequency change detected will be negative relative to the transmit frequency, i.e. less than the transmit frequency. However, the simple model described by Fig. 2.1 is further complicated by the acoustic properties of tissue and the scattering of ultrasound in blood flow.

2.3.2 Acoustic Properties of Tissue

Human tissue is not homogeneous, but consists of various tissue types which have differing acoustic impedance. Ultrasound signals reduce as a function of distance and attenuation due to acoustic impedance. Acoustic impedance Z is related to tissue density ρ and the velocity of sound in the tissue type v such that; $Z = \rho v$. The amount of energy R reflected at the normal interface of two different tissue types is defined by

$$R = \left[\frac{(Z_2 - Z_1)}{(Z_2 + Z_1)} \right]^2 \tag{2.2}$$

where Z_1 and Z_2 are the respective impedances of the different tissue types on either side of the interface [9]. R is termed the reflection coefficient.

The acoustic properties of some tissue types at a frequency of 1 MHz are described in Table 2.1. Note that although the biological tissues listed have high acoustic impedance, they have low half 50% signal levels. For example, water is not very 'lossy' and exhibits a 50% signal decrease for a depth of 41 m. However, fat, which has a slightly lower acoustic impedance, exhibits a 50% signal decrease for a depth of only 3.8 cm. Furthermore, lthough not described by Table 2, it should also be

noted that the rate of attenuation increases with frequency.

Table 2.1: Acoustic properties of some tissue types at 1 MHz [9].

Tissue Type	Speed of Sound v, ms^{-1}	Acoustic Imped. $Z, \mathrm{g/cm^2 s}$	Atten. Coeff. dB/cm	50% Power cm	Interface	Reflect. Coeff.
Water	1496	1.49×10^5	0.0022	4100	Air/ Water	0.999
Fat	1476	1.37×10^5	0.63	3.8	Water/ Fat	0.042
Muscle	1568	1.66×10^5	0.96–1.4	2.5	Water/ Muscle	0.054
Brain	1521	1.58×10^5	0.75 ± 0.17	2.5	Water/ Brain	0.029
Bone	3360	6.20×10^5	14.2–25.2	0.23	Water/ Bone	0.614
Air	331	4.13	12	1.1	Tissue/ Air	0.999

2.3.3 Scattering of Ultrasound in Blood Flow

Blood is a highly complex fluid that is composed of objects of differing shapes and sizes, such as plasma, leukocytes, erythrocytes and platelets. The overwhelmingly dominant ultrasonic scatterers are the erythrocytes or red blood cells (RBC) [10]. These are biconcave and discoidal cells are approximately 8 μm in diameter and 2 μm thick [11]. At typical ultrasonic frequencies, an individual RBC is two orders of magnitude smaller than the ultrasound wavelength and can therefore be considered to be a *Rayleigh* scatterer, for which the backscattered power increases as the fourth power of the frequency [10]. Various models have been developed over the years to describe the scattering process. However, it is recognised that ultrasound backscattering by blood is highly complex due to the tendency of RBCs to aggregate. It is sufficient in the context of this project to consider the ultrasound backscattering of RBCs as a stochastic process; RBCs can be considered to behave as a random array of targets and it can be assumed that the backscattered power is proportional to the number of RBCs that interact with the ultrasound insonation [10]. Since the backscattering efficiency of blood increases with frequency, the choice of the opti-

mal ultrasound frequency to achieve the best signal to noise ratio (SNR) becomes a compromise with the desired penetration depth.

2.3.4 Operating Modes

Doppler ultrasound has two fundamental operating modes; continuous wave (CW) and pulsed wave (PW). CW systems use continuous transmission and reception of ultrasound. *Doppler* signals are obtained from all scatterers in the path of the ultrasound beam (until the ultrasound beam becomes sufficiently attenuated due to depth). Continuous wave *Doppler* ultrasound cannot be used to determine the specific location of velocities within the beam and, as a result, cannot produce colour flow images or a *Doppler* sonogram for a specified range. PW systems send pulsed transmissions at a pre-defined pulse repetition frequency (PRF), also referred to as the sampling frequency. This allows PW systems to measure the depth (or range) of the flow site and permits a variable sample volume (or range gate) to be defined which allows the user to select the desired depth for insonation of a particular vessel. PW ultrasound systems can therefore produce *Doppler* sonograms and colour flow images.

2.4 Transcranial *Doppler* Ultrasonography

Development of an ultrasound method to interrogate the intracranial arterial system lagged behind the evaluation of the extracranial arterial systems. It was not until the 1980s that the techniques described in section 2.2 were used to successfully insonate the MCA [6] using an intracranial ultrasound system. This delay in the application of ultrasound to the intracerebral vessels occurred largely because it was originally thought that insufficient ultrasound could pass through the skull to allow recording at the required depth of human tissue [12]. However, it was discovered that a low frequency transducer operating at around 2 MHz could penetrate within the transtemporal acoustic window, a region of the skull where the bone thins to around 2-3 mm (shown in Fig. 2.2). This region provides access to the intracerebral vessels in the *circle of Willis*, the cerebral arterial circle at the base of the brain

which includes the MCA.

A: Transtemporal window; used to insonate the middle cerebral artery (MCA), the anterior cerebral artery (ACA) and the posterior cerebral artery (PCA).

B: Transorbital window; used to insonate the ophthalmic artery (OA) and the ICA (siphon).

C: Suboccipital window; used to insonate the distal vertebral arteries (VA) and the basilar artery (BA).

D: Submandibular window; used to insonate the distal portions of the ICA.

Figure 2.2: Transcranial *Doppler* probe acoustic windows [13].

The underlying principles of ultrasound dictate that the choice of operating frequency imposes a trade-off between spatial resolution and desired penetration depth. Low frequency ultrasound waves have a longer wavelength and achieve less resolution, but can penetrate deeper into the body. Higher frequency sound waves are capable of reflecting or scattering from smaller structures and can therefore achieve a greater resolution. As discussed in section 2.2.2, higher frequency sound waves also have a larger attenuation coefficient and are thus more readily absorbed in tissue, limiting the depth of penetration of sound into the body. At 2 MHz, the spatial resolution is poor and the ultrasonography techniques adopted at this operating frequency are primarily useful for *Doppler*. Hence these acoustic windows permit sufficient insonation to use intracranial ultrasound techniques to analyse blood flow.

TCD is a PW intracranial ultrasound technique. From the definition of a PW *Doppler* ultrasound described in section 2.2.4, it permits hemodynamic information

of a region to be analysed at a selected depth. The depth of insonation is established by gating the transmitted pulse at a given PRF. This information can be combined with an anatomical understanding of the intracranial arteries, enabling the accurate identification of a ROI. However, the choice of operating frequency in TCD ultrasound systems also imposes a trade-off between SNR and desired penetration depth. Whilst, from the Nyquist-Shannon sampling theory, the maximum *Doppler* frequency (f_D) that can be measured unambiguously is half the PRF.

These operating characteristics limit the use of TCD to a small number of specialised clinical applications. Examples of application areas where TCD is currently being used for research and investigation include:

i. Detection of intra-cranial stenosis.

ii. The analysis of blood flow in the secondary channels after an obstruction or narrowing of the principal channel i.e. collateral flow.

iii. Measurement of dynamic cerebrovascular responses.

iv. Intra-operative monitoring.

v. Detection of cerebral embolus.

The focus of the system proposed in this project is long term ambulatory detection and monitoring of cerebral embolus.

2.4.1   Embolic signal detection using TCD

Embolic signal detection is a mature application of *Doppler* ultrasound. It involves the detection of abnormally high-pitched signals within the arterial waveform as a method for diagnosis and prediction of embolic complications in at-risk patients. These emboli produce unidirectional high intensity transient signal (HITS) which give a distinctive 'popping' sound when observed by *Doppler* ultrasound.

2.4.2 Patient Examination Procedure

In an Acute Stroke Unit, clinicians will normally perform a TCD ultrasound recording of a patient within 24 hours of admittance following a significant stroke event or as part of an outpatients appointment when a patient is suspected of having a transient ischemic attack (TIA) or "mini stroke". The assessment results will inform a risk stratification process. At the Acute Stroke Unit in Glasgow's Queen Elizabeth University Hospital the system employed for this purpose is a ST3 PMD150 Digital Transcranial *Doppler* System[i]. Typical commercial TCD systems are capable of separating embolic events from noise and other artefacts and can support automatic embolus detection at depths of between 30 mm and 80 mm, providing an automated count of embolic events.

Typically, TCD systems display *Doppler* information in two standard colour displays; M-mode and Spectrogram. A ST3 TCD System display is shown in Fig. 2.3.

---

[i]Spencer Technologies, Seattle, WA, USA.
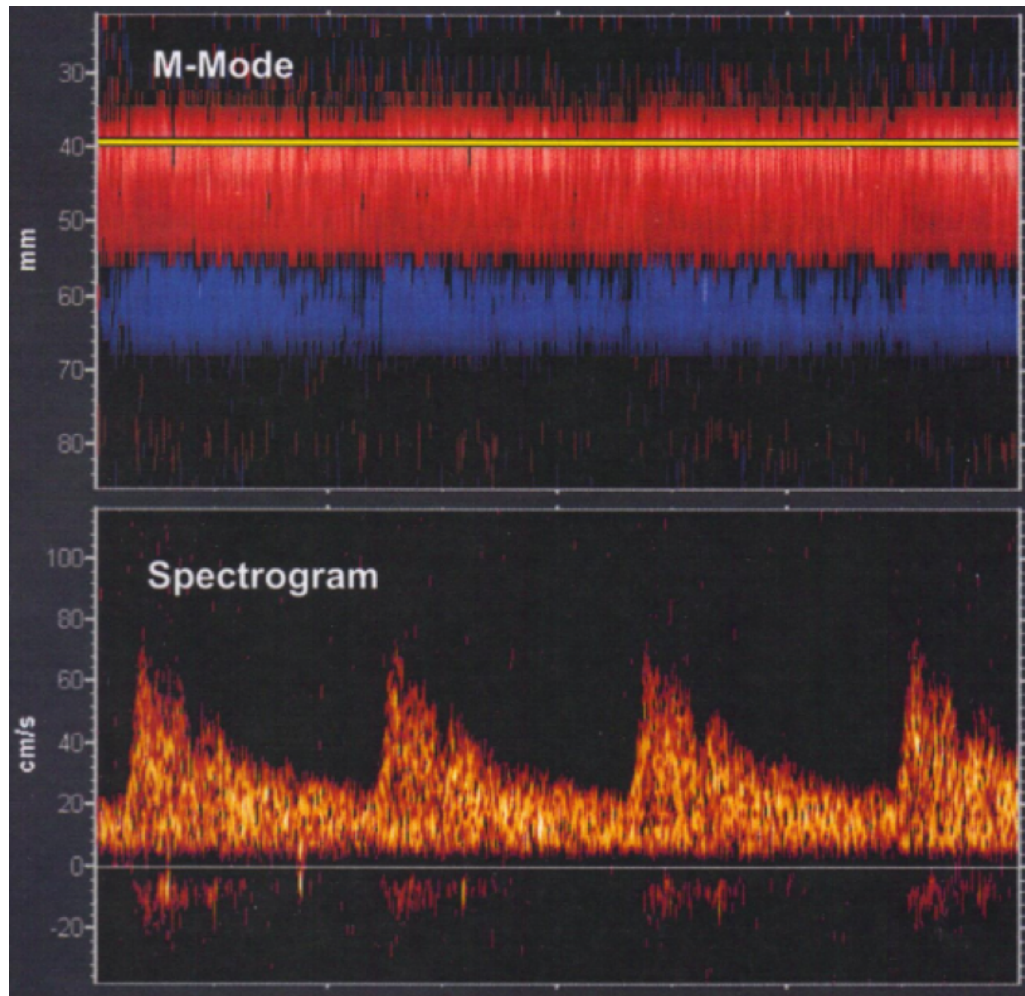
Figure 2.3: TCD M-mode and spectrogram displays[i].

The M-Mode display shows all blood flow in terms of *Doppler* signal power within a specified depth range against time. The flow is colour coded using a standard convention such that blood flowing away from the transducer is shown blue, whilst blood flow towards the transducer is shown red. The Spectrogram shows the *Doppler* spectral waveform, indicating the velocity profile of blood flow at the selected depth on the M-mode display against time.

Under normal monitoring conditions, the patient is required to lie on a bed adjacent to a trolley mounted TCD unit. A headset is fitted on the patient providing a fixation for up to two transducer channels (left and right side). Once fitted it is normally necessary to perform a short system set up procedure during which a blood flow wave is acquired from the MCA, normally located at a depth of between 35

mm and 60 mm. Acquisition of an adequate signal is largely down to the skill and experience of the operator. Once a strong signal is acquired, the patient is ready to undergo monitoring for up to one hour during which time the system will capture and record the blood flow waveform. The system is normally configured to automatically detect and count embolus events during a recording. The operator can then browse and analyse recordings of embolus events post-examination and provide an assessment of the findings. In combination with other patient observations, the number and classification of emboli detected will inform a risk assessment and will be used to devise a course of treatments and interventions.

2.4.3 Limitations of Current TCD Systems

There are a number of issues and limitations with current TCD systems which reduce the effectiveness of the TCD observations.

i. TCD recordings are highly sensitive to movements by the patient and require very accurate setup and alignment of the transducer. As shown in section 2.2.1, optimal recordings are obtained with an insonation angle of 0° and perfect lateral alignment with the direction of blood flow in the vessel. If a misalignment occurs during a test procedure the readings captured are likely to be incomplete or corrupt.

ii. As a result of (i), frequent monitoring of the patient and test procedure is required. Operators and clinicians often need to perform fine adjustments of the transducer during the patient examinations.

iii. A transducer probe fixation head-clamp is required to maintain accurate alignment of the transducer probe. However, patients find these to be very uncomfortable, particularity if worn for long periods.

iv. Embolus events are counted, not characterised in terms of size, velocity, material consistency etc.

v. Movement artefacts and other noise can frequently be misinterpreted as embolus.

vi. TCD systems are trolley mounted, and are therefore not sufficiently portable to allow patients to be moved during testing.

These issues are the key limiting factors which prevent patients undergoing longer term monitoring for embolus events. Since it is thought that embolisation is a dynamic process and may show marked variability when short recordings of 30 to 60 minutes are performed, the inability to make longer, more reliable recordings may be a limiting factor in determining the appropriate level of risk that a patient may experience further stroke events [14, 15]. This may impede the appropriate intervention strategy and limit the volume of patient data that could be acquired for both research and audit of patient care.

Furthermore, in the case where a TCD system were employed as part of a wider research or clinical trials program, the ability to perform much longer ambulatory monitoring would be highly advantageous. For example, this could be the case when monitoring patients with asymptomatic embolic signals [15], or when determining the effectiveness of particular surgical or pharmacological therapies.

In order to understand more about the dynamics of embolus events, clinicians require the ability to perform longer, more reliable TCD examinations, with improved levels of reporting accuracy. This requires a system level re-design such that, whilst the models proposed in the later chapters of this work can contribute to improvements in the performance of future TCD ultrasound systems, a holistic approach is required to ensure that an optimal solution is delivered to meet all the requirements of patients and clinicians.

2.5 Microembolic Signal Detection Algorithms

MES signal detection is a standard feature of TCD systems, however not all emboli are easy to detect. There are two distinctive characteristics of emboli in blood flow which contribute to this detection problem; motion characteristics and relative reflectivity. Of these, the relative reflectivity of the emboli has the highest bearing on

detectability. For example, if the emboli is a weak scatterer in comparison to the surrounding blood flow, it may not be possible to analyse its motion characteristic. Consider a 20 μm diameter emboli consisting of a clot of red blood cells travelling in the centre of the MCA. The reflectivity will be nearly indistinguishable from the reflectivity of background blood flow. However, a 20 μm diameter gaseous bubble travelling at the same velocity and position in the MCA will stand out dramatically due to its far greater level of reflectivity. The system sensitivity is therefore dependent on the size, composition and location of emboli.

Due to the complexities of their formation, emboli can be corpuscular (e.g. lipid droplets, calcified particles etc.) or gaseous (e.g. artificially inserted gas or as the result of micro-cavitation). The exact nature of the formation and development of embolus is not fully understood. However, it is known that emboli can occur in the blood stream as the result of a number of complex haemodynamic effects and in a number of different locations in the body. Those most likely to cause ischemia occur in the chambers or valves of the heart as a result atrial fibrillation or atherosclerotic plaques.

Atrial fibrillation or AF is a type of irregular heartbeat (arrhythmia) that reduces or limits the pumping action of the heart. As a result, thrombosis are more likely to form in the heart chambers, increasing the risk of a stroke. AF can be asymptotic and thrombosis can form microemboli from small clusters of RBCs.

Atherosclerosis is a disease where plaque (made from calcium, cholesterol and fatty deposits) builds up inside the arteries over a period of time, where it can harden and narrow the artery walls. These deposits can generate embolus of varying size and consistency. From relatively large thrombus or pieces of calcified plaque which would lead to significant and devastating stroke events, to microscopic microemboli, typically less than 100 μm in diameter, which can cause micro-infarction in the small arteriolar branches and vessels of the brain.

Microemboli are of particular interest, as they can be a crucial indicator or symptom of stroke risk and can be detected in asymptotic patients. There have been many studies of microembolic signal detection in the cerebral arteries in the last twenty years. At the core of these studies has been the objective of not only achieving reliable detection of MES using TCD, but also development of the ability to accurately discriminate the size and composition of microemboli, since this can provide the clinician with crucial information from which to prescribe the most appropriate intervention strategy. Indeed, it is thought that understanding the composition of microemboli using TCD can help clinicians better understand the development and source of microemboli. This section discusses current and emerging approaches to microembolic signal detection in TCD.

2.5.1 Embolic *Doppler* Signal Characteristics

The *Doppler* shift observed by TCD systems lies within the human audible range and, as mentioned in section 2.3.1, when MES are observed they have a distinctive 'popping' sound. This sound is not uniform, but can be described as similar to *Gaussian* white noise, that is to say it has a peak central frequency and a bell shaped *Gaussian* profile. In signal processing terms, *Girault et al* [16] described an embolic *Doppler* signal in the terms of a time varying signal $x(t)$ as the summation of a background signal representing the backscatter by blood, background noise and a brief duration random high intensity signal, given by

$$x(t) = r(t) + \sum_{i=1}^{N_i} E_i(t - \theta_e) + B(t) \tag{2.3}$$

where $r(t)$ represents the background signal resulting from the backscatter by blood and $B(t)$ is the background noise in the observation. For each instance i, E_i represents an embolus, a high intensity signal of brief duration at time occurrence $(t - \theta_e)$. This signal description can be further elaborated by providing consideration for motion artefacts A_k, such as patient movement and probe motion, as shown by

$$x(t) = r(t) + \sum_{i=1}^{N_e} E_i(t - \theta_e) + \sum_{k=1}^{N_k} A_k(t - \theta_k) + B(t). \tag{2.4}$$

However, (2.4) is not normally used in practice since a technique developed by *Smith et al* [17] based on dual gated *Doppler* ultrasound can be used to simultaneously range-gate at two separate depths, in order to distinguish between emboli and artefacts. This technique is used as justification for ignoring motion artefacts A_k and, as a result, (2.3) is used for all practical situations.

2.5.2 Embolus to Blood Ratio

There are a number of commercial TCD systems available that can automatically detect and count emboli in human blood. Typically, these systems use power spectrum analysis based on a classical *Fourier* approach (described in section 2.4.3) and the HITS characteristic of MES in *Doppler* signals to identify emboli backscatter in blood. This backscatter can be quantified using the embolus to blood ratio (EBR), as developed by *Moehring et al* [18, 19, 20]. The HITS occur randomly and in order to detect them in the *Doppler* signal, the *Doppler* response is sampled at regular intervals and the EBR is calculated. *Moehring* showed that "if the *Doppler* sample volume is made large enough to include the transverse section of the vessel" the EBR can be expressed as

$$EBR = \frac{\sigma_E}{\sigma_B} = 10 log_{10} \left[\left(\frac{\sigma_B + \sigma_E}{\sigma_B} \right) - 1 \right] dB \qquad (2.5)$$

where σ_E is the backscattering cross section of emboli flowing in the sample volume and σ_B is the backscattering cross section of the RBC flowing in the sample volume.

A decibel thresholding technique is then used where the calculated EBR is compared to a pre-determined detection threshold. If the calculated EBR is greater than or equal to the threshold, embolus detection is declared and the embolus detection count is incremented.

Using the EBR model, *Moehring et al* went on to predict an important aspect of EBR relating to microemboli detection, sizing and characterisation [20]. Through exploration of the backscattered power from embolus, the EBR model predicts that

backscattered power will have a region over which embolus are non-*Rayleigh*.

This is demonstrated in Fig. 2.4 where line (a) shows the anticipated backscattered power from blood and curve (b) shows the EBR model prediction of backscattered power from an embolus. The important feature of curve (b) is that it predicts that at an insonation frequency above approximately 2.5 MHz, embolus begin to have a non-*Rayleigh* region where the backscattered power no longer increases as a fourth power of frequency. This observation reinforces the importance of selecting an insonation frequency below 2.5 MHz for TCD ultrasound, where *Rayleigh* scattering is predicted and the relative backscattered power against frequency plot in Fig. 2.4 remains linear.
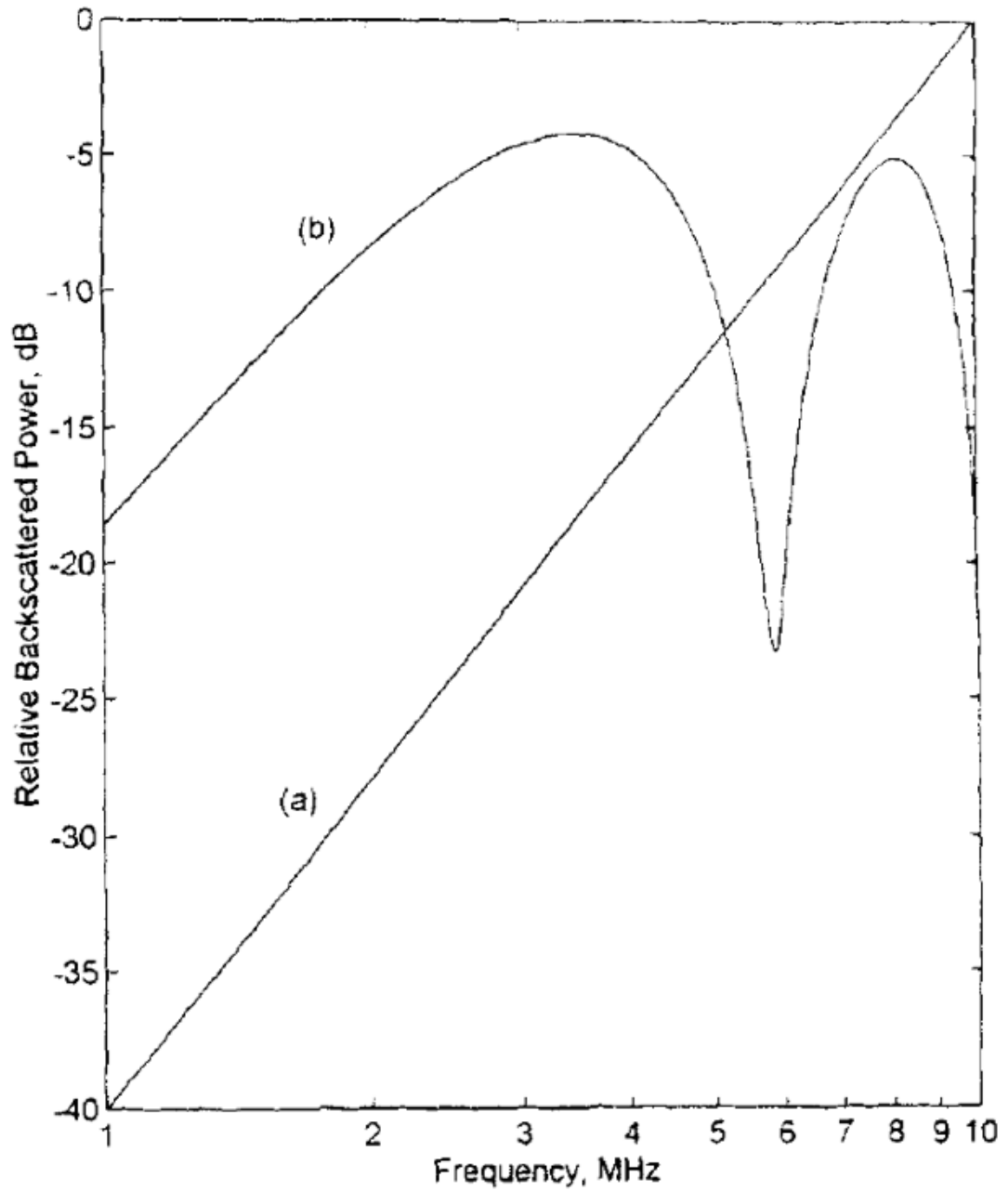
Figure 2.4: EBR model predication of relative backscattered power; line (a) shows the anticipated backscattered power from blood and curve (b) shows the EBR model prediction of backscattered power from an embolus [20].

2.5.3   Classical *Fourier* Based Approach

In the classical *Fourier* based approach a spectrogram is created to find the power spectral density of the signal at time t. The power spectral density is calculated

from the time-varying signal using a short-time Fourier transform (STFT).

In the continuous time case, a *Fourier* transform of the detected signal taken at time t is given by

$$X(\tau, \omega) = \int_{-\infty}^{\infty} x(t)w(t-\tau)e^{-j\omega t}dt \qquad (2.6)$$

where $w(t)$ is a window function and $x(t)$ is the time varying signal, given by the summation of the background signal representing the backscatter by blood and any brief duration random high intensity signals representing backscatter by emboli (2.3). Equation (2.6) can be approximated in the discrete time case to

$$X(m, \omega) = \sum_{n=-\infty}^{\infty} x[n]w[n-m]e^{-j\omega n}. \qquad (2.7)$$

where the sequence $f_m[n] = x[n]w[n-m]$ is a short-time section of the received signal $x[m]$ at time n. The spectrogram (power spectral density of the windowed signal) is given by the modulus of the STFT squared

$$P(m, \omega) = |X(m, \omega)|^2 = \left| \sum_{n=-\infty}^{\infty} x[n]w(n-m)e^{-j\omega n} \right|^2. \qquad (2.8)$$

Fig. 2.5(a) shows a spectrogram created using Matlab$^{\text{TM}}$(*MathWorks, Inc.*) from a TCD recording captured using a ST3 Digital TCD System. In this figure it is possible to clearly distinguish the high frequency ridge caused by a HITS generated as the result of an embolus. Fig 2.5(b) shows the HITS in the time domain, where it can be seen to correspond to an approximate duration 20 msec.
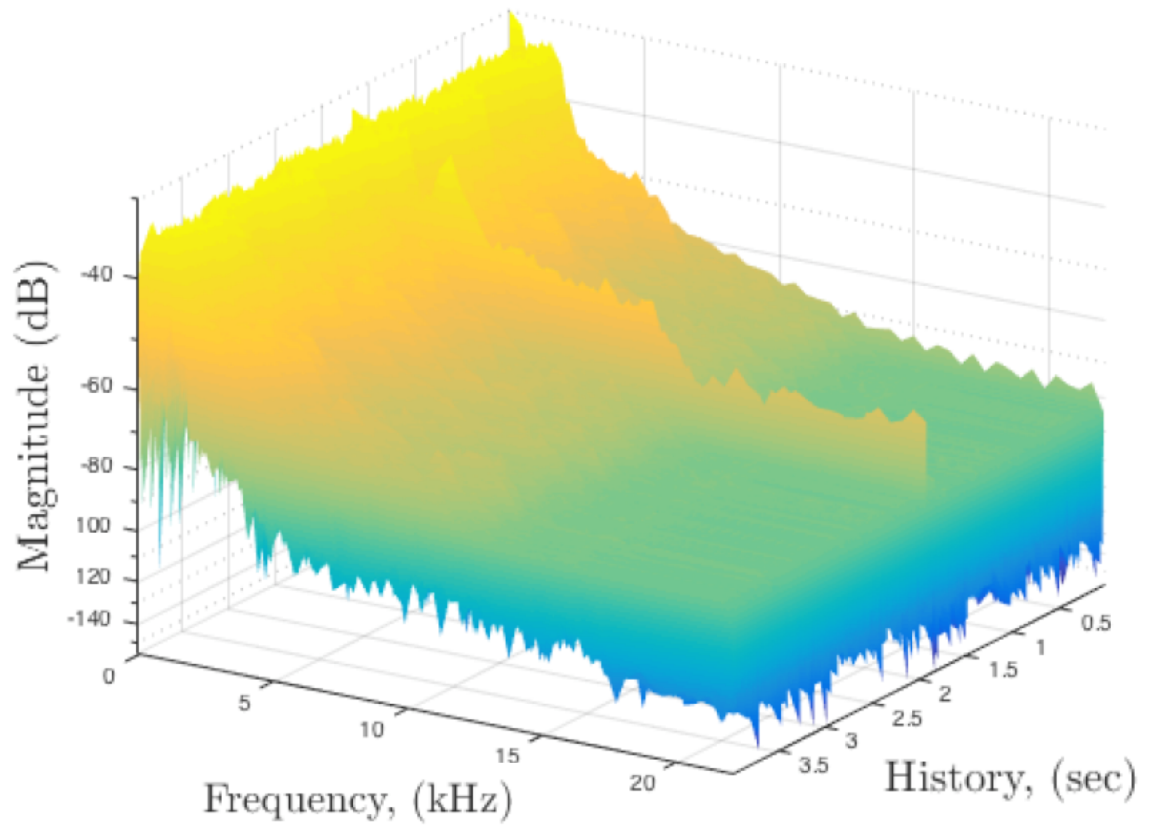
(a)
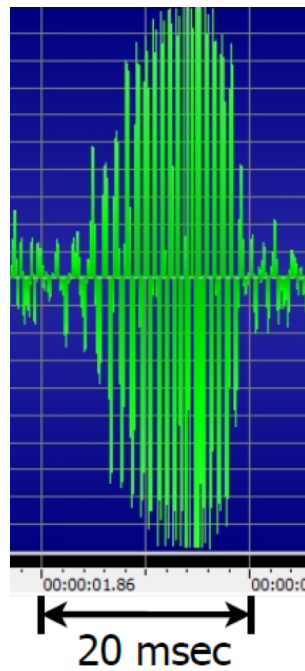
(b)

Figure 2.5: (a) A 3-D spectrogram of an embolus detected in a TCD recording. (b) The same embolus detection in the time domain.

The limitations of STFT as a signal processing technique are well documented. The STFT is a linear approach that decomposes the signal into elementary components. The main drawback is the fixed nature of the time / frequency resolution and its relationship with the windowing function. The selection of the fixed duration of the windowing function establishes a trade-off in the *Fourier* transform, determining whether there is a good frequency resolution or a good time resolution. If the analysis window is too narrow, the frequency resolution may be poor but the time resolution may be good. Conversely, if the analysis window is too wide, the time resolution may be poor, but frequency resolution may be good. This presents a major problem for analysis of MES which, by their nature, are short duration narrowband signals that are easily compromised by this time-frequency resolution dilemma.

Due to variations in implementation methods such as window size, the number of FFT points and the detection thresholds used in *Fourier* based emboli detection systems, a marked variability was observed in the performance of some early commercial systems [21]. More recently, studies of emboli detection in TCD ultrasound have focused on a migration from *Fourier* based signal processing techniques towards other signal processing techniques in an effort to resolve the limitations described.

2.5.4 *Wigner-Ville* Distribution

The *Wigner* distribution (WD) was derived by the Hungarian-American physicist *Eugene Wigner* in the 1930s [22] and is defined as

$$W_x(t,f) = \int_{-\infty}^{\infty} x(t+\frac{\tau}{2})x^*(t-\frac{\tau}{2})e^{-j2\pi f\tau}d\tau. \tag{2.9}$$

It is a time-frequency representation used for the analysis of non-stationary time-varying signals, where non-stationary refers to the frequency content of the signal which may change over time and cannot be predicted. Functionally, it is similar to the *Fourier* based spectrogram, however it offers better temporal and frequency resolution.

The *Wigner-Ville* distribution (WVD), or *Wigner-Ville* spectrum, is the *Wigner* distribution using the analytical associate of the detected signal. In the continuous time case, the WVD of the detected signal $x(t)$ taken at time t is given by

$$W_z(t, f) = \int_{-\infty}^{\infty} z(t + \frac{\tau}{2}) z^*(t - \frac{\tau}{2}) e^{-j2\pi f \tau} d\tau \qquad (2.10)$$

where $z(t)$ is the analytic associative of $x(t)$, and $z^*(t-\tau/2)$ is the complex conjugate of $z(t-\tau/2)$. Signal $z(t)$ is analytic if $Z(f) = 0$ for $f < 0$, where $Z(f) = \mathcal{F}\{z(t)\}$. The discrete *Wigner-Ville* distribution (DWVD) [23] can be approximated by

$$W_z(\frac{n}{f_s}, f) = \frac{2}{f_s} \sum_{m=-N/2+1}^{N/2-1} z[n+m] z^*[n-m] e^{-j4\pi f(n/f_s)} \qquad (2.11)$$

where f_s is the sampling rate, N is the number of samples and z[n] is analytic.

The first use of the WVD for detection of emboli in blood is thought to be in the mid-nineties [24], when it was used to discriminate emboli in blood flow using measures of instantaneous frequency and power. However there have been more recent examples where DWVD has been used to determine the frequency modulation index of a *Doppler* signal to assess the ability of frequency modulation techniques to discriminate solid and gaseous emboli [25]. As well as better temporal and frequency resolution, the main motivation for using the WVD is the ability to calculate the instantaneous frequency and energy spectra at any time within the selected window.

Although the WVD offers potentially a better detection performance based on peak energy threshold, one of the drawbacks of the *Wigner-Ville* distribution is the introduction of interference terms (cross-terms) which add noise to the spectrogram. Since WVD is a quadratic time-frequency analysis method, when there is more than one frequency component in the received signal cross-terms occur between the auto-terms, indicating the false existence of signal components. It is possible to smooth these interference terms by, for example, convolving the *Wigner-Ville* distribution with a smoothing function, e.g. the Modified *Wigner-Ville* distribution

function. However, the computational efficiency and resulting performance of such interference mitigation strategies must be balanced against other approaches, such as wavelet filtering and parametric signal processing.

2.5.5 Wavelet Theory

Although the origins of wavelet theory can be traced back to the 1930s, it was not until the early 1980s that it emerged as an area of digital signal processing. It is thought that the first studies of wavelet theory for the application of emboli detection in blood were made in the late 1990s [26, 27]. Like the application of *Wigner-Ville* to emboli detection, the motivation behind applying wavelet theory to improve the detection of emboli in blood flow was driven by the need to overcome the inherent trade-off between temporal and spacial resolution in the classical *Fourier* based approach. Wavelet theory provides a method for analysing transient or non-stationary signals and is particularly useful when signals are both non-stationary and of very short duration. MES fit this description well.

In wavelet theory, signals are analysed in terms of wavelet basis functions. These wavelets can be composed by scaling and shifting a 'mother function' or 'analysing wavelet' to describe a signal $x(t)$. Wavelets are obtained from the 'mother function' through modification of scaling (dilation or compression) and shifting (translation) parameters, as defined by

$$\psi_{a,b}(t) = \frac{1}{\sqrt{a}}\psi^*\left(\frac{t-b}{a}\right), \text{for } \{a \neq 0, b \in \Re\} \tag{2.12}$$

where ψ^* denotes the complex conjugate of ψ, a is the scaling factor and b is the shifting parameter, and belongs to the real set. The continuous wavelet transform (CWT) is given by

$$W_f(a,b) = \int_{-\infty}^{\infty} x(t)\psi_{a,b}(t)dt \tag{2.13}$$

and the inverse continuous time wavelet transform is given by

$$x(t) = \frac{1}{C} \int_0^\infty \int_{-\infty}^\infty W_f(a, b)\psi_{a,b}(t)db\frac{da}{a^2} \tag{2.14}$$

where

$$C = \int \frac{|\psi(\omega)|^2}{\omega}d\omega < \infty. \tag{2.15}$$

In the discrete time case, a wavelet series can be obtained by sampling the continuous-time input signal $x(t)$. For fast computation of the discrete time wavelet transform, the discrete wavelet transform (DWT) is used. The DWT is based on sub-band coding, a method of transform that breaks the signal into a number of individual frequency bands. This is achieved using the *Mallat* algorithm [28] where the discrete-time signal is passed through a series of low and high pass filters as described in Fig. 2.6. The discrete signal sequence $x[n]$ is shown to pass through a high pass
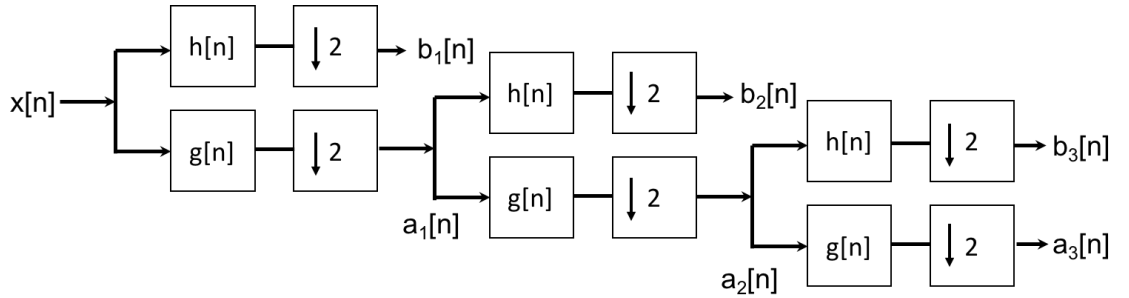
Figure 2.6: A 3-level wavelet filter bank.

filter $h[n]$ and a low pass filter $g[n]$ at the first level in a cascading filter bank and the output of these filter stages are shown to pass through a sub-sampling stage, where they are sub-sampled by 2 (denoted by the sub-sampling operator $\downarrow 2$). The high pass filter stage produces detail coefficients $b_1[n]$. The low pass stage produces coarse approximation coefficients $a_1[n]$ associated with the scaling function. For the first stage, $b_1[n]$ and $a_1[n]$ can be expressed by

$$a_1[n] = \sum_{k=\infty}^\infty x[n]g[2n - k] \tag{2.16}$$

and

$$b_1[n] = \sum_{k=\infty}^{\infty} x[n]h[2n-k]. \qquad (2.17)$$

At the next level in the filter bank the coarse approximation $a_1[n]$ is used as the input to the next filtering stage and the process repeats.

It can be seen from Fig. 2.6 that at each level in the filter bank the filter stages produce coefficients spanning only half the frequency band. This has the effect of doubling the frequency resolution at each stage in the decomposition. The number of levels required depends on the length of the input sample and the sampling rate. The DWT of the input signal is obtained by concatenating the coefficients from each filtering level.

The choice of the 'mother function' from which to derive the wavelet and scaling coefficients is of crucial importance and is driven by the desired signal characteristics in the wavelet transform. Examples of 'mother functions' chosen in previous emboli studies include the *Morlet* wavelet [26, 27].

More recently, there has been considerable interest in the application of wavelet theory and DWT to embolic signal detection. *Marvasti et al* demonstrated that intelligent wavelet filtering approaches based on a DWT and *Daubechies* 8th order wavelet may provide a 2 dB increase in observed EBR and a 10-20% improvement in detection accuracy compared to commercial based systems using a STFT based approach [29]. More recently, this technique has been adapted to enhance the detection of emboli signals using wavelet de-noising in order to improve classification performance and noise tolerance in TCD systems [30].

2.5.6 Parametric Signal Processing

Parametric signal processing methods have been used in studies to detect emboli in simulated signals [16, 26]. In each case an autoregressive (AR) model has been used to provide a method of linear prediction of an output signal based on previous

outputs. The AR model is a stochastic process in which future values are estimated based on a weighted sum of past valses, i.e. past values effect future values. Using this approach, the *Doppler* signal can be modelled as the output of a linear filter driven by white noise [16]. At sample time n, the discrete-time *Doppler* signal $x(n)$ can be described by

$$x(n) = \sum_{i=1}^{p} a_i x(n - p) + \eta(n) \tag{2.18}$$

where $\eta(n)$ is white noise, a random signal that is assumed to have a constant power spectral density, zero mean, and a variance of σ^2. The order of the AR model is given by p, and $a_1...a_i$ are the AR parameters or filter coefficients. It is usually sufficient for $p = 2$.

There are a number of possible algorithms that could be used to calculate the AR parameters. One approach is to use the recursive least squares (RLS) algorithm. As shown in [26], (2.18) can be re-written as

$$x(n) = \varphi_n^T \theta + \eta(n) \tag{2.19}$$

where

$$\varphi_n^T = [x(n - 1), ...x(n - p)] \tag{2.20}$$

$$\theta = [a_1, ...a_p]^T \tag{2.21}$$

If $\hat{\theta}$ is the estimate of θ, obtained at each sampling time using the RLS algorithm, the *Doppler* signal can be estimated at each sampling time using

$$\hat{x} = \varphi_n^T \hat{\theta} \tag{2.22}$$

and the prediction error can then be calculated using

$$e(n) = x(n) - \hat{x}(n). \tag{2.23}$$

The AR model therefore provides an error at each sample time based on the difference between the predicted *Doppler* signal and the actual *Doppler* signal. In normal conditions where no embolic signal is present, the AR model will produce only slow variations of predicted error due to the phases of blood flow in the insonated vessel [16]. When an emboli is present in the *Doppler* signal, the predicted error shows a significant change, due to the high intensity nature of the emboli signal (Fig. 2.5(a)). This change can be compared to a pre-determined threshold. The threshold level can be determined through analysis of recorded *Doppler* signals with an acceptable SNR and no emboli present. As the system is a binary classifier (embolus detection is either true or false), receiver operating characteristics (ROC)s can then be plotted to establish the probability of false positive detection and an optimal relative threshold can be determined.

In the results presented in the studies discussed [16, 26], for the simulated embolic *Doppler* signals, parametric signal processing techniques based on the autoregressive model were demonstrated to have the ability to detect smaller MES (embolus with smaller EBR) than STFT, DWVD and wavelet based systems. Further, *Girault et al* observed that, whilst classical STFT based methods were only able to reliably detect embolus when $EBR_{min} \geq 12$ dB, DWVD and Wavelet approaches can reliably detect embolus when $EBR_{min} \geq 10$ dB. However, parametric methods were able to out perform these methods and achieve reliable embolus detection with $EBR_{min} \geq 5$ dB.

2.5.7 Summary of Microembolic Signal Detection Techniques

In this section a number of signal processing techniques have been discussed in the context of MES detection using TCD ultrasound. The traditional *Fourier* approach using STFT is used widely by commercial systems but has significant disadvantages. These disadvantages are centred on the fixed nature of the time / frequency resolution and its relationship with the windowing function. This establishes a trade-off in the *Fourier* transform between good frequency resolution and good time resolution.

The *Wigner-Ville* distribution is functionally similar to the *Fourier* based spectrogram, but offers better temporal and frequency resolution. However, one of the drawbacks of the *Wigner-Ville* distribution is the introduction of interference terms which add noise to the spectrogram. Although there are techniques that can be used to smooth this interference, the performance of the mitigation strategies must be balanced against other approaches, such as wavelet theory and parametric signal processing techniques.

Wavelet theory is a particularly good approach for MES detection since it overcomes the inherent trade-off between temporal and spacial resolution in the classical *Fourier* based approach and provides an excellent technique for detecting signals that are both non-stationary and of very short duration. Studies using DWT and a *Daubechies* 8th order wavelet have demonstrated a 2 dB increase in observed EBR and a 10-20% improvement in detection accuracy when compared to commercial based systems using a *Fourier* based approach.

Similarly, techniques based on parametric signal processing using an autoregressive model have shown significant potential and may actually out perform all the other techniques described for detection of small MES.

Wavelet theory and parametric signal analysis techniques seem to have some distinct advantages over the other approaches discussed and may provide features which significantly improve the capabilities for detection of emboli in *Doppler* signals. However, it seems clear that no single technique is likely to offer the ability to both robustly detect and accurately discriminate the size and composition of MES in *Doppler* signals. A hybrid technique based on a weighted combination of two or more approaches may offer the best solution to the MES detection problem.

2.6 Enhanced DSP Techniques

TCD ultrasound developers and researchers have sought to improve methods of MES detection and classification using complex signal processing techniques. For example, there has been much recent interest in the use of chirp signals (pulse compression), coded excitation and pseudo noise (PN) codes [31, 32, 33, 34] which use coded pulse sequences and digital signal processing (DSP) methods to improve the sensitivity and reliability of detection, and subsequently the ability to track blood flow and emboli motion. In the subsections that follow, the history behind emergence of these techniques are introduced, and the relation to TCD ultrasound is discussed.

2.6.1 Chirp Signals (Pulse Compression)

Chirp signals are a form of pulse compression where the frequency of the signal is modulated (FM chirp) in order to create a modified transmit pulse in which the duration of the pulse is shortened whilst the energy in the pulse is preserved such it that can be used to increase the resolution and SNR of the received signal. This technique was pioneered in the development of pulse compression techniques for early RADAR systems by teams at the Sperry Gyroscope Company and the M.I.T. Lincoln Laboratory in the 1950s [35]. However, it wasn't until the late 1970s when pulse compression and coded excitation (Golay code) methods first emerged in medical ultrasound. *Takeuchi* was the first to adapt these techniques to the signal processing requirements of ultrasound [36, 37], when he observed that in RADAR, the *"main subject of their signal processors seems to be 'clutter suppression' rather than object detection itself"*. However, this work was limited by the capabilities of ultrasound hardware systems at that time and it would require the emergence of DSP techniques and more advanced micro-processors overcome these early limitations.

Interest in chirp signals in medical ultrasound rose again in the early 1990s when *O'Donnell* demonstrated that major improvements in SNR (15–20 dBs) of an ultra-

sound phased array system were possible when using coded excitation (pseudo-chirp) and pulse compression techniques [38]. In TCD ultrasound, methods of improving conventional pulse compression techniques lag behind conventional ultrasound imaging systems. More recent publications addressing the use of chirp pulses in TCD systems have demonstrated that amplitude-modulated chirp pulse 'shaping' can be used to vastly improve the axial resolution [31], i.e. the discrimination of multiple scatterers on a single scan-line. However, discussions on the use of chirp signals have more recently merged into wider efforts on coded-excitation.

2.6.2 Coded Excitation & Pseudo Noise Codes

The concept of using coded excitation in ultrasound imaging to improve the balance of resolution and penetration depth was established in the early 2000s [39], however it is relatively new in TCD ultrasound. Within this area of research, techniques such as pseudo noise (PN) [32, 34] and *Barker* codes [33] are investigated. These techniques use coded pulse sequences and signal processing methods to improve the sensitivity and reliability of detection, and subsequently the ability to track embolus within blood flow.

In TCD ultrasound systems, to obtain adequate SNR from blood flow in the MCA a long transmit pulse is required. However, long transmit pulses reduce the sensitivity of emboli detection through decreased EBR and also result in poor axial resolution, a problem that is acutely sensitive in TCD since MCA typically have a diameter of 3-4 mm and a length of approximately 20 mm.

Although it is possible to improve both EBR and axial resolution by increasing the pressure amplitude to compensate for the reduced transmitted pulse length, this cannot be achieved safely since there is a corresponding increase in the systems mechanical index, leading to the possibility of undesirable biological effects from cavitation.

Pulse compression and shaping using coded excitation methods is a potential solution to this problem. There are a number of methods which can be employed for this purpose based on phase or frequency modulation approaches and differing the coding sequences (*e.g., Barker, Golay*, m-sequences, *etc.*). For TCD systems, *Barker* code excitation has been demonstrated to both improve the sensitivity and reliability of detection, and the ability to track embolus in blood flow [31, 32, 33]. A *Barker* code is a finite sequence of N values of $+1$ and -1. For $j = 1, 2, 3...N$ the sequence has ideal autocorrelation properties, such that the off-peak (non-cyclic) autocorrelation coefficients are given by

$$c_v = \sum_{j=1}^{N-v} a_j a_{j+v}. \tag{2.24}$$

There are known *Barker* codes of lengths 2, 3, 4, 5, 7, 11, and 13, however it is generally accepted that no longer codes exist. In TCD systems the sequence of desired code length N would be modulated with the base pulse to compress and shape the transmitted pulse and achieve a shortened sample volume length. The compression process is normally achieved using a matched filter whilst an inverse filter can be used to process the received signal.

2.6.3   Summary of Enhanced DSP Techniques

The latest advances in embedded micro-processor performance and software DSP techniques provide an exciting opportunity for the next generation of TCD systems. The potential improvements in sensitivity and reliability of MES detection offered by the use of coded pulse techniques and the latest DSP technology, can deliver systems capable of precisely tracking blood flow and emboli motion in TCD systems. In order to achieve an optimal design, a thorough knowledge of TCD ultrasound propagation channel is required. This can only be achieved by using channel propagation models which accurately predict the statistical properties of the channel and the received signal.

2.7 Modelling Wave Propagation in Medical Ultrasound

The modelling of wave propagation in medical ultrasound has concentrated on numerical mathematical models and the majority of this effort in the past twenty years has involved the development of linear and non-linear acoustic wave equations [40]. More recently, intra-body ultrasonic communications has begun to generate interest in stochastic modelling of ultrasound. However, at the time of writing the author is unaware of any existing literature related to the development or investigation of stochastic modelling of TCD ultrasound. This section summarises current approaches to acoustic wave modelling, then introduces and describes stochastic propagation channel modelling of TCD ultrasound.

2.7.1 Acoustic Wave Modelling

In parallel with the rapid advancement in performance of computer processors, memory peripherals, and graphics processing units (GPU)[ii], computationally intensive linear and non-linear acoustic (NLA) model equations such as *Westervelt* [41] and *Khokhlov-Zabolotskaya-Kuznetsov* (KZK) (modifications of models from underwater acoustics), and the k-space pseudospectral method [42] (or simply the k-space method - a set of analytical and conceptual tools for the analysis of ultrasound in k-space) are being used in biomedical applications. These model equations are used in areas such as the design of phased transducer arrays, optimisation of imaging performance, and treatment planning for therapeutic applications. The accuracy and utility of these numerical mathematical models and their ability to accurately predict the propagation of ultrasound in heterogeneous tissue is typically dependent on the management of three important factors; the acoustic properties of tissue, non-linear wave propagation, and the power-frequency law of attenuation. It should be noted that the discussions on numerical mathematical models that follows are included as part of a review of current acoustic wave modelling techniques. Acous-

---

[ii]GPUs are used together with a CPU to markedly increase computational efficiency.

tic wave models and their associated mathematical expressions are not suitable for stochastic analysis of the received signal and will not be used in this study.

2.7.1.1 *Westervelt*

The generalised form of the *Westervelt* wave equation is given by

$$\rho \nabla \cdot \left(\frac{1}{\rho} \nabla p \right) - \frac{1}{c^2} \frac{\partial^2 p}{\partial t^2} + \frac{\delta}{c^4} \frac{\partial^3 p}{\partial t^3} = -\frac{\beta}{\rho c^4} \frac{\partial^2 p^2}{\partial t^2} \tag{2.25}$$

where p is the sound pressure, c is the small signal sound speed, δ is a measure of sound diffusion, β is the non-linearity coefficient, and ρ is the ambient density. The non-linearity coefficient is a function of the pressure-density relation and produces distortion in the travelling wave [43]. Sound diffusion δ can be considered as a measure of the even scattering of sound energy in a medium, and is a function of the viscosity, thermal conductivity, and specific heat capacity [44]. There are several alternative forms which can be derived from (2.25), such as (2.26), the *Westervelt* equation for homogeneous media [40],

$$\nabla^2 p - \frac{1}{c_0^2} \frac{\partial^2 p}{\partial t^2} + \frac{\delta_0}{c_0^4} \frac{\partial^3 p}{\partial t^3} = -\frac{\beta_0}{\rho_0 c_0^4} \frac{\partial^2 p^2}{\partial t^2} \tag{2.26}$$

where p_0, c_0, δ_0 and β_0 become the acoustic parameters for the medium. Further, by setting the non-linearity coefficient β_0 in (2.27) to 0, we can derive the linear variant of the *Westervelt* acoustic wave equation,

$$\nabla^2 p - \frac{1}{c_0^2} \frac{\partial^2 p}{\partial t^2} + \frac{\delta_0}{c_0^4} \frac{\partial^3 p}{\partial t^3} = 0 \tag{2.27}$$

The *Westervelt* wave equations are used to characterise acoustic fields for transducer design and to study acoustic field estimations in biological tissue. The non-linear versions are used in applications of high intensity, high pressure ultrasound when the linear approximation begins to introduce inaccuracies due to tissue harmonics, the thermal effect, and cavitation.

2.7.1.2 *Khokhlov-Zabolotskaya-Kuznetsov* (KZK)

Although the numerical ultrasound community is gradually migrating towards the *Westervelt* equation in recent years [40] on account of its greater accuracy in the near field and at positions off the beam axis, KZK is currently the most popular acoustic wave equation because of its simplicity whilst also supporting the effects of diffraction, absorption and non-linearity. The KZK equation is given by

$$\frac{\partial^2 p}{\partial z \partial \tau} - \frac{c_0}{2}\nabla_\perp^2 p - \frac{\delta_0}{2c_0^3}\frac{\partial^3 p}{\partial \tau^3} - \frac{\beta_0}{2\rho_0 c_0^3}\frac{\partial^2 p^2}{\partial \tau^2} = 0 \qquad (2.28)$$

where the nominal axis of the beam is the z-axis and τ is retarded time, i.e. the time when the acoustic field began to propagate ($\tau = t - (z/c_0)$) [40]. Like the *Westervelt* equation, the KZK equation includes the non-linearity coefficient and is used to model non-linear acoustics. The main advantage over the *Westervelt* equation is computational efficiency, however as the KZK equation is less accurate in the near field and at positions off the main insonation axis [40], the classic version of the KZK equation cannot be used to accurately model wide angle or beam steering ultrasound systems [45].

2.7.1.3 *k*-space Method

The k-space method is a solution to a system of coupled acoustic wave equations using an exact finite difference scheme that reduces to an operator in the spatial frequency domain or 'k-space' [42]. It creates a frequency domain description of an ultrasound system that can be used to gain insight into linear acoustic propagation. The k-space representation of an imaging system makes system analysis easier as image translation, rotation, and shearing transformations are more computationally efficient in the spatial frequency domain than the time domain [46]. Originally developed for the analysis of experiments involving anisotropic scattering and for the design of acoustic tomography systems, k-space ultrasound frequency domain processing techniques have also found utility in pulse echo ultrasound systems [47]. The k-space method is limited to linear system analysis, although there are a number of recent modified approaches based on k-space which may be used to model non-

linear propagation [42, 48]. Furthermore, *Anderson et al* also states that the k-space method has no obvious means of representing non-laminar flow or non-*Rayleigh* scatterers [49] in blood, such as contrast agent, micro-bubbles or MES. This may be a limiting factor for the use of k-space methods in TCD *Doppler* ultrasound.

2.7.2 Ultrasonic Communications

More recently, studies of channel modelling in ultrasound are emerging within investigations of ultrasonic communications for intra-body networks [50, 51]. In this special case, experimental observations using a kidney phantom at insonation frequencies of 4-5 MHz were performed, and received ultrasonic signals were measured to establish the extent of interference from multi-path fading. In this case the statistical characteristics of the channel fading coefficient were modelled using the *Nakagami* distribution [52] and a good match to measured results was reported. However, this analysis was performed at insonation frequencies much higher than that used for TCD ultrasound, and interest was focused on the effects of interference on point-to-point communications. No attempt was made to investigate a stochastic propagation channel model using first and second order statistics.

2.7.3 Stochastic Propagation Channel Modelling

Stochastic analysis is the study of random probability distributions or patterns that may be analysed statistically but may not be predicted precisely. The NLA wave equations and k-space methods described in section 2.6.1 are highly accurate methods that can be used to analyse complex acoustic wave propagation in heterogeneous media, however they are less suitable for channel modelling, where the capacity for information transfer is analysed. When advanced signal processing techniques such as coded excitation are used (section 2.5), channel modelling can inform the design of ultrasound equipments, and the development of signal and image processing algorithms. In this section stochastic propagation channel modelling is considered in relation to multi-path propagation in TCD ultrasound.

2.7.3.1   Multi-path Propagation in TCD Ultrasound

As with imaging and therapeutic applications of ultrasound, in TCD ultrasound a pulse is transmitted through tissue and the received echo is the sum of scattered, diffracted, and reflected components of that pulse as shown in Fig. 2.7.
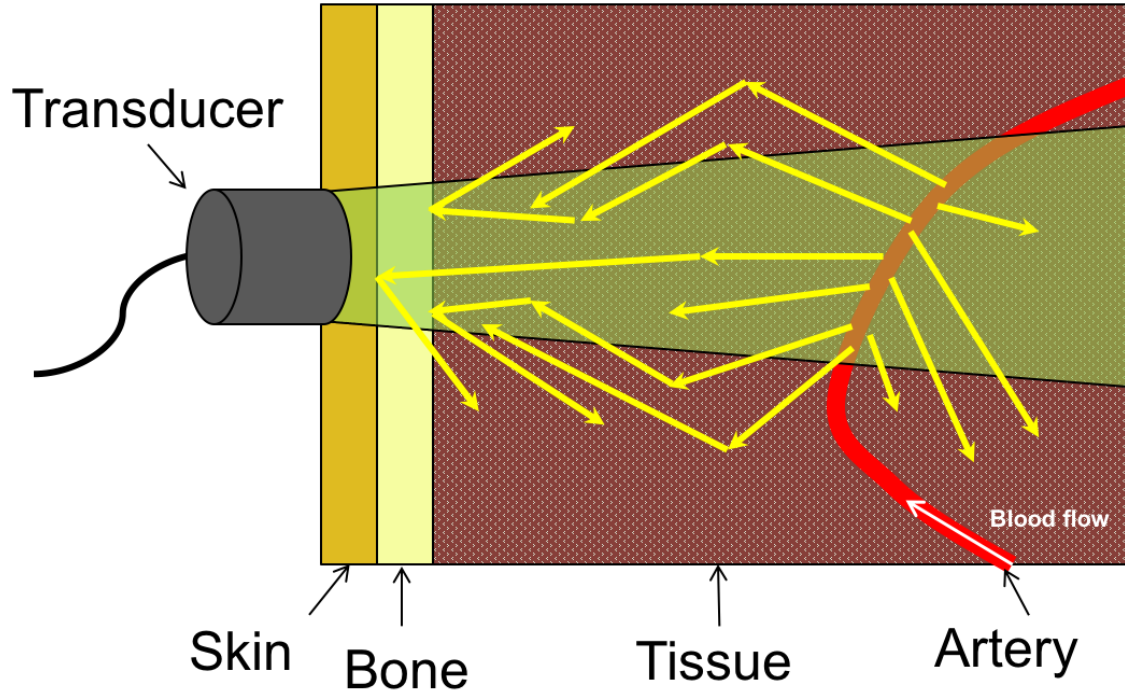
Figure 2.7: A schematic showing the effects of scattering, diffraction and reflection on TCD ultrasound propagation channel.

This effect is known as multi-path propagation and although ultrasound waves are longitudinal compression waves as opposed to two dimensional transverse waves, the end result is similar to the effects observed in radio channels. It can be considered as the constructive and destructive superposition of an infinite sum of attenuated, delayed, and phase-shifted replicas of the transmitted signal [53]. The degree to which this scattering occurs is a function of the transmission frequency and the acoustic properties of the tissue in the insonation path. The acoustic properties of the major tissue classes (fat, muscle, brain, and water; Table 2.1) are weakly inhomogeneous with low acoustic impedance at the tissue interfaces. In contrast the velocity of sound in bone is much higher (over 2×) and has a significantly greater acoustic

impedance at the tissue interface. It is the presence of these inhomogeneous layers and the non-linear scattering effects of RBCs that cause artefacts in ultrasound B-mode images. Similarly, and as discussed in section 2.5, it is this same scattering effect of RBCs in blood flow that leads to the *Doppler* frequency and phase shift that allows us to study haemodynamics and embolisation.

Multi-path fading resulting from these scattering effects can also have a significant impact on the design of algorithms for the detection and characterisation of MES. For example, signal distortion resulting from fading and the associated delay spread (the difference between the time of arrival of the earliest significant scattering reflection and the latest significant scattering reflection) can reduce or negate the ability of an algorithm to detect and analyse a MES. It is therefore crucially important to understand the fading characteristics of the channel and the degree to which some form of fading mitigation may be appropriate. Such analysis would then inform algorithm design.

2.7.3.2 Analysis of the Received Signal

If we consider a perfect system and a normal observation, where no emboli, artefacts or background noise are present, the received band-pass signal $r(t)$ will be the amplified radio frequency (RF) signal resulting from the backscatter of blood. In terms of the complex envelope, the received signal $r(t)$ may be expressed as

$$r(t) = Re[g(t)e^{j2\pi f_c t}] \qquad (2.29)$$

where $g(t)$ is the multi-path fading channel response and f_c is the ultrasound insonation frequency. The channel response comprises of N propagation paths and can be expressed as [54]

$$g(t) = \sum_{n=1}^{N} C_n e^{j\theta_n(t)} \qquad (2.30)$$

where C_n is the signal amplitude and $\theta_n(t)$ is the time-variant phase associated the nth path. The later is given by

$$\theta_n(t) = \theta_n - 2\pi[(f_c + f_{D_n})\tau_n - f_{D_n}t]. \tag{2.31}$$

In (2.31), θ_n is the phase shift randomly introduced by the reflection of the acoustic wave from the nth scatterer and can be uniformly distributed between $-\pi$ and π. The time delay, τ_n is the delay of the nth propagation path, and f_{D_n} is the *Doppler* frequency shift. The magnitude C_n depends on the cross sectional area of the scatterer and its properties; RBCs are the most significant scattering bodies in the insonation region. With the assumptions that the insonation frequency is unmodulated and the channel is flat fading, the received band-pass signal $r(t)$ can be expressed as [54]

$$r(t) = Re[(g_I(t) + jg_Q(t)).(\cos(2\pi f_c t)j\sin(2\pi f_c t))], \tag{2.32}$$

where the in-phase and quadrature components $g_I(t)$ and $g_Q(t)$ are

$$g_I(t) = \sum_{n=1}^{N} C_n \cos(\theta_n(t)) \tag{2.33}$$

and

$$g_Q(t) = \sum_{n=1}^{N} C_n \sin(\theta_n(t)). \tag{2.34}$$

In (2.33) and (2.34), as $N \to \infty$ the central limit theorem states that $g_I(t)$ and $g_Q(t)$ can be treated as *Gaussian* random processes and the phase angles are continuous independent random variables with PDF $p(\theta)$.

A block diagram showing the simplified receive signal processing chain of a PW *Doppler* system is shown in Fig. 2.8. Transmitted pulses are reflected by stationary structures and blood flow. The analogue received signal passes through a filter and RF amplifier, and is digitised by the analogue to digital converter. Pulse-echo receive range gating is used to select *Doppler* signals from blood flow according to

distance from the ultrasound probe [10].

For spectrogram and M-mode processing, quadrature phase detection and phase filtering are used to separate the in-phase (I) and quadrature (Q) side-bands which correspond to blood flow direction; forward (systole; U) and reverse (diastole; L). These outputs feed into the digital signal processing functions used to generate the M-mode and spectrogram displays.
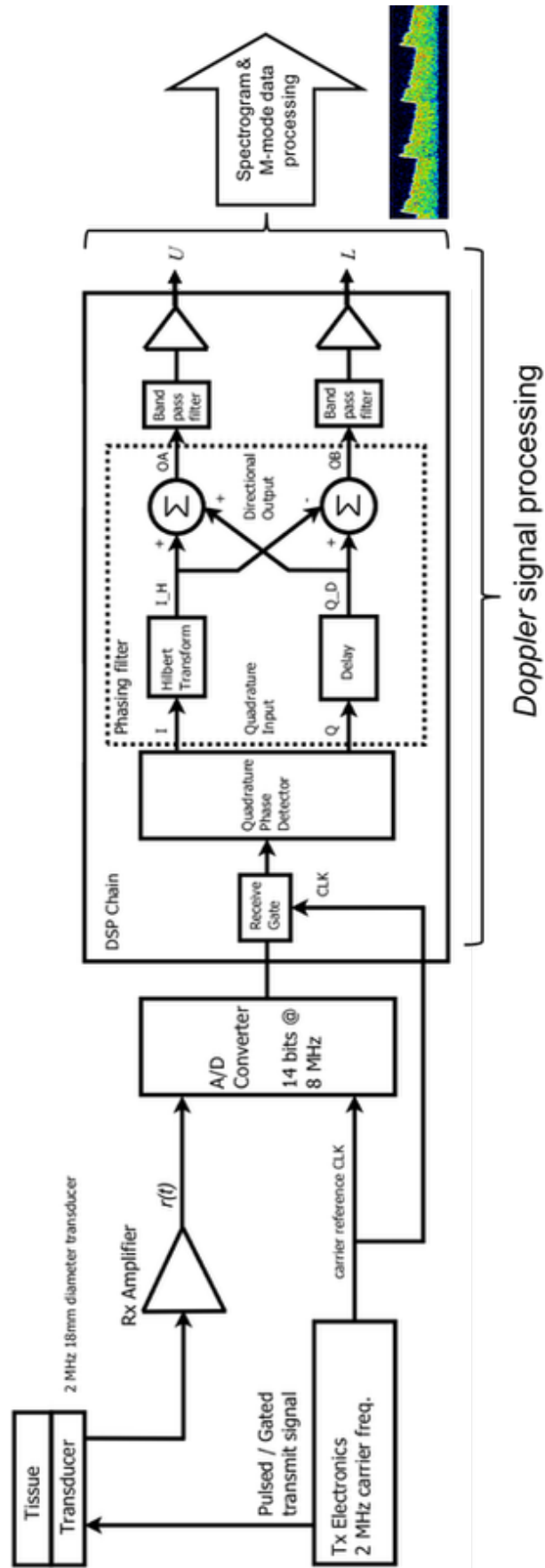
Figure 2.8: A block diagram of a TCD system receive signal processing chain.

2.8 Summary

This chapter began by providing a review of the principles of *Doppler* ultrasound in section 2.2, taking the classical theory developed by *Christian Doppler* and relating this directly to the problem of obtaining ultrasound images of blood flow and MES detection. From this starting point, the fundamental operating principles of *Doppler* ultrasound were explored in section 2.3 and the challenges of obtaining ultrasound images of blood flow were described. Importantly, the acoustic properties of tissue and the scattering properties of blood were also introduced.

In section 2.4, TCD ultrasound was discussed and its use as a non-invasive modality for the interrogation and monitoring of blood flow in the intra-cranial arterial system was described. The key challenges of performing long term ambulatory monitoring of the MCA were also discussed and the limitations of current TCD systems were highlighted.

Using this basic system description as our starting point, a technology survey was performed in section 2.5 in which the four main signal processing approaches for MES detection were described; STFT, *Wigner-Ville*, wavelet theory and parametric signal processing. From the results summarised in section 2.5, parametric signal processing techniques based on an AR model out performed the other methods. Classical STFT based methods are only able to reliably detect embolus when $EBR_{min} \geq 12$ dBs, whilst DWVD and Wavelet approaches can reliably detect embolus when $EBR_{min} \geq 10$ dBs. Parametric methods were reportedly able to achieve reliable embolus detection with $EBR_{min} \geq 5$ dBs. From this comparison, although parametric techniques show considerable promise, the suggestion was made that a hybrid technique based on a weighted combination of two or more approaches may offer the most reliable and robust method of MES detection in blood flow.

Additionally, a summary of the emerging applications of coded excitation and pulse compression in TCD ultrasound have been included and the basic principles of these

techniques were explained in section 2.6. These signal modulation schemes are based on the migration of signal processing approaches first developed in radio communications systems. Analysis of these techniques found that chirp signals can increase the SNR of ultrasound phased array systems by 15–20 dBs using coded excitation, whilst chirp pulse 'shaping' using coded excitation and PN codes may also improve axial resolution. However, lessons from radio communications [53] have shown that successful design and integration of such techniques relies upon a thorough knowledge of the channel and the multi-path propagation effects resulting from reflection, diffraction, and scattering of the received signal by the medium. This fundamental analysis is missing from current TCD system design. In order to design an optimal TCD system that can take full advantage of the complex signal processing algorithms that are available, it is crucial that a framework is established through development of theoretical and simulation models with which to explore and describe the propagation channel.

This problem was highlighted further in section 2.7, when current methods of modelling wave propagation in medical ultrasound were described and reviewed. These methods include the traditional NLA wave equations and the k-space method. Although these techniques can provide highly accurate models of ultrasound propagation in heterogeneous media, they do not support stochastic analysis of the propagation channel and cannot be used to analyse the deleterious effects of multi-path fading. Since it is understood that multi-path fading can have a significant impact on the design of algorithms for the detection and characterisation of MES, there is a fundamental requirement to develop methods of channel characterisation and modelling for TCD ultrasound. The translation of stochastic channel propagation techniques from communications technology may provide a solution to this problem.

From the analysis presented in sections 2.5, 2.6, and 2.7, it is apparent that improvements in robust and reliable MES detection rates are possible if hybrid signal processing techniques can be combined with suitable modulation schemes. This should permit reliable and robust MES detection at $EBR_{min} \geq 5$ dBs or less, and

may be capable of precise emboli motion tracking. However, since existing acoustic wave modelling methods do not support analysis of the channels information transfer characteristics, a stochastic propagation channel model is required in order to design and develop an optimal TCD ultrasound system for this purpose.

In summary, as in many other regions of the developed world, it is widely accepted that the financial burden of an ageing population in the UK is likely to become unsustainable. To meet this challenge, new and improved methods of preventive and anticipatory healthcare are being investigated and developed across a broad range of medical applications. TCD ultrasound can be one of those transformative technologies. It can provide our clinicians with the ability to diagnosis and predict embolic complications in stroke patients. Indeed, TCD ultrasound may offer the only way to monitor asymptomatic embolisation and, therefore, must play an important role in assessing risk and preventing strokes in the future. However, there are a number of important aspects of current TCD ultrasound system design, as highlighted in this chapter, that should be improved before it can be fully utilised within a proactive and preventive use case. Most notably, we need to re-consider our understanding of the channel characteristics of TCD ultrasound by developing TCD ultrasound propagation channel models, and use this knowledge to develop new and improved algorithms that can be optimised to take advantage of this insight. This strategy would appear to offer the most effective route to delivering more accurate and reliable levels of MES detection. If this can be achieved, TCD ultrasound can help to further our understanding of cerebrovascular disease and significantly improve outcomes for patients.

The key motivation of this thesis will be the development of a suitable TCD ultrasound propagation channel model to support the development and design of the next generation of TCD ultrasound systems. In Chapter 3 an initial approach to this problem will be discussed by investigating and analysing 3-D isotropic spherical scattering channel models for TCD ultrasound.

Chapter 3

3-D Isotropic TCD Ultrasound Propagation Channel Models

3.1 Introduction

In this chapter, 3-D isotropic spherical scattering channel models for TCD ultrasound are developed. Firstly, using a 3-D half-spheroid geometry, the characteristics of a theoretical reference model are described. Then the statistical properties are investigated in terms of the PDFs, temporal ACF, *Doppler* PSD, envelope LCR, and AFD. These investigations then extend beyond the theoretical model by defining a simulation model, for which the characteristics and statistical properties are once again defined. From this simulation model a SoS [55] flat fading channel simulator is developed. The chapter concludes by summarising and comparing the characteristics and statistical properties of the theoretical reference model, simulation model, and SoS channel simulator, analysing the extent to which the models agree, their usefulness, and limitations.

3.2 Theoretical Reference Model

The study of multi-path effects and the design of wireless communications systems has evolved through many theoretical 2-D and 3-D channel models [56, 57, 58]. Taking the signal received at the RF amplifier, as shown in Fig. 2.8, and considering the

envelope correlation for a fading channel in ultrasound to be analogous to that of a baseband signal in a radio communications system, we can apply a similar approach to the characterisation of a *Doppler* ultrasound propagation channel.

In the sub-sections that follow, a model geometry is developed based on a 3-D half-spheroid geometry. A single element ultrasound transducer is assumed to be stationary and positioned at the origin of the *Cartesian* coordinates. The ultrasound system is simplified to consider only the returning reflection from a strong isotropic scattering region within blood flow of an insonated vessel. Tissue is assumed to be homogeneous with uniform acoustic impedance.

3.2.1   Model Geometry

The scattering geometry can be elaborated by considering the propagation channel as a 3-D isotropic half-spheroid [54, 59, 60, 61, 62], as shown in Fig. 3.1. Strong scatterers are assumed to exist within and around the periphery of the half-spheroid region. The intersection of the scatterers with the $x - z$ plane is a semi-ellipse with axial lengths $2a$ and b, along the x and z axis respectively, such that a is the radius of the base and b is the height of the half-spheroid. The direction of blood flow in the insonation region is, without any loss of generality, assumed to be in the direction of the x axis with velocity v.
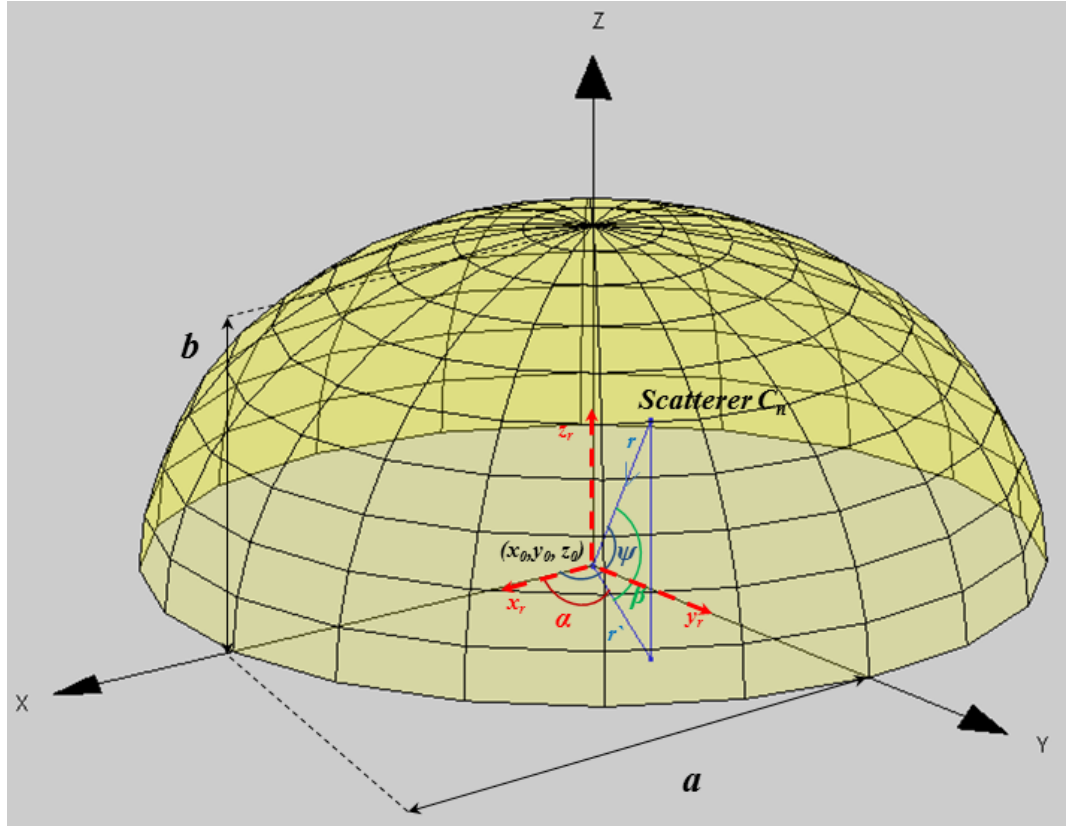
Figure 3.1: An illustration of the 3-D plane within a hemispherical model.
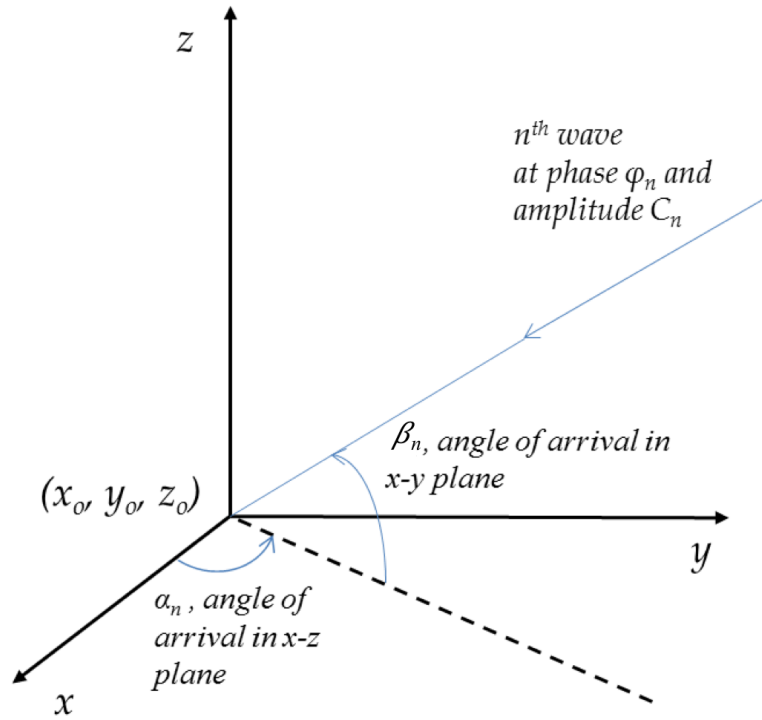
Figure 3.2: An illustration of a component wave in a 3-D plane.

Fig. 3.1 and Fig. 3.2 show illustrations of the nth component wave in a 3-D plane. Each plane wave has a phase θ_n, a magnitude C_n, and an angle of arrival (AOA). The spatial AOA ψ_n is formed between the incident wave and the direction of motion of blood flow and consists of two components; an azimuth angle of arrival (AAOA) α_n to the $x - z$ plane and an elevation angle of arrival (EAOA) β_n to the $x - y$ plane. The model parameters α_n, β_n, θ_n and C_n are all random and statistically independent. The nth incident plane wave in a 3-D plane can be described by

$$E_n(t) = C_n e^{j(\theta_n t - k_w \hat{A})} \tag{3.1}$$

where

$$\hat{A} = [x_0 \cos(\alpha) \cos(\beta) + y_0 \cos(\alpha) \cos(\beta) + z_0 \sin(\beta)] \tag{3.2}$$

and k_w is the wave propagation constant, or wave number, determined by

$$k_w = \frac{2\pi}{\lambda_c}. \tag{3.3}$$

The sum of N statistically independent plane waves is given by

$$E(t) = \sum_{n=1}^{N} E_n(t). \tag{3.4}$$

The scattered components can be modelled by a zero-mean complex-valued *Gaussian* random process

$$\mu(t) = \mu_1(t) + j\mu_2(t) \tag{3.5}$$

where μ_1 and μ_2 are the in-phase and quadrature components respectively. In the isotropic case, the sum of scattered components do not include a line-of-sight (LoS) component and (3.5) leads to a *Rayleigh* process such that

$$\zeta(t) = |\mu(t)| = |\mu_1(t) + j\mu_2(t)| \tag{3.6}$$

3.2.2 Statistical Properties of the Theoretical Model

3.2.2.1 Amplitude & Phase PDF

The marginal PDFs of AAOA and EAOA, i.e. $p_\alpha(\alpha)$ and $p_\beta(\beta)$, can be used to define the PDF of the spatial AOA, $P_\psi(\psi)$. The derivations of the 3-D half-spheroid PDFs are provided in Appendix B.1. In the case of the PDF of the AAOA $p_\alpha(\alpha)$, it can be assumed that scatterers are distributed uniformly around the transducer, as shown by (B.45),

$$p_\alpha(\alpha) = \frac{1}{2\pi}, 0 \leq \alpha \leq 2\pi. \tag{3.7}$$

However, the PDF of the EAOA $p_\beta(\beta)$ can be derived as (B.46),

$$p_\beta(\beta) = \frac{\left(\frac{b}{a}\right)^2 \cos(\beta)}{\left[\sin^2(\beta) + \left(\frac{b}{a}\right)^2 \cos^2(\beta)\right]^{\frac{3}{2}}}, 0 \leq \beta \leq \frac{2}{\pi}. \tag{3.8}$$

In (3.8), $p_\beta(\beta)$ can be seen to depend only on the ratio of $\frac{b}{a}$, and for the special case where $a = b$, the PDF simplifies to $p_\beta(\beta) = \cos(\beta)$. To demonstrate the effect of altering the ratio of $\frac{b}{a}$, $p_\beta(\beta)$ is plotted as a function of the elevation angle for sample values of $\frac{b}{a}$ in the oblate spheroid case ($b \leq a$) in Fig. 3.3 and in the prolate spheroid case ($b \geq a$) in Fig. 3.4.
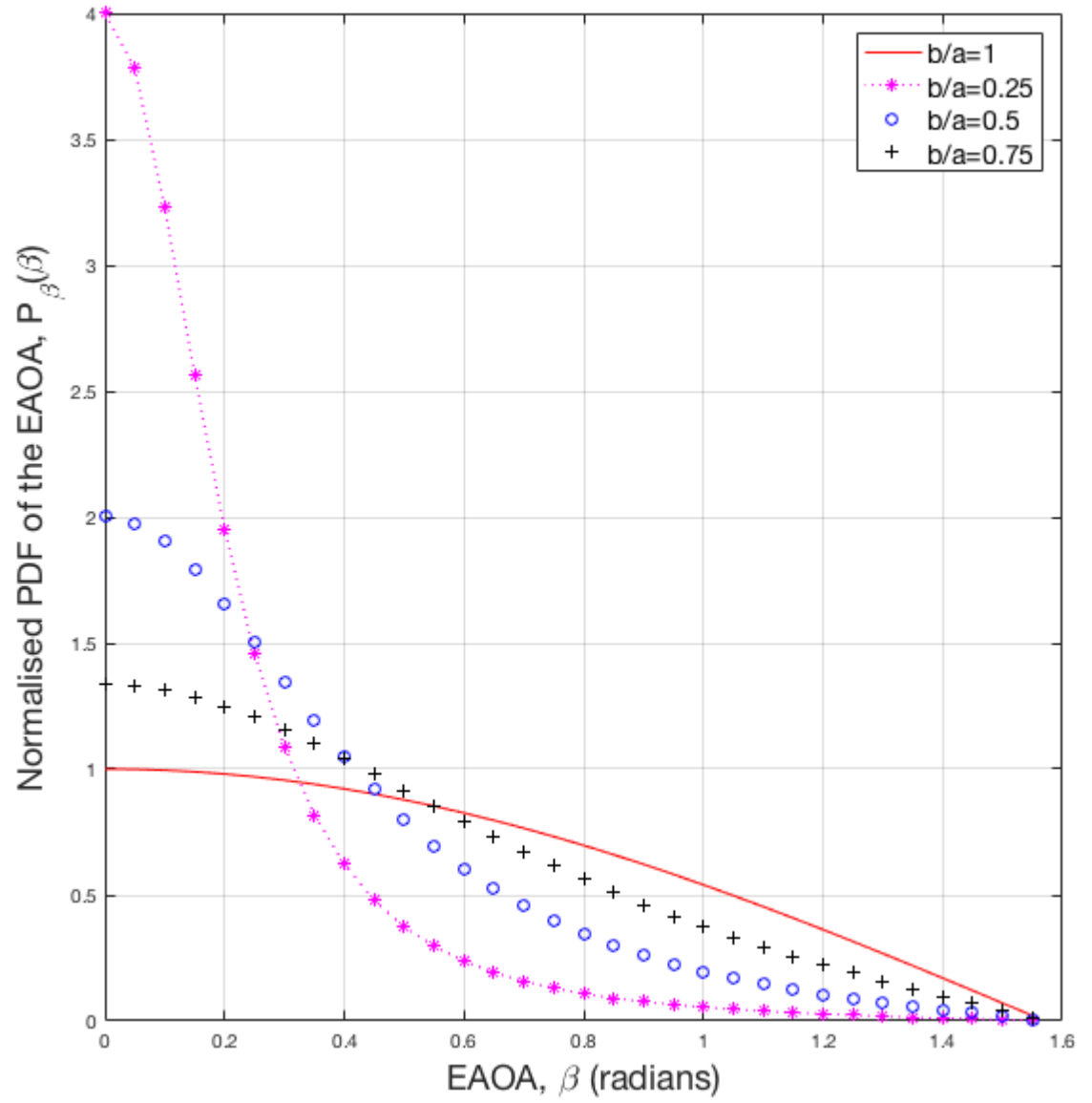
Figure 3.3: The 3-D isotropic half-spheroid PDF of the EAOA seen at the transducer for $\frac{b}{a} = 0.25$, 0.5, 0.75 and 1 (i.e. an oblate half spheroid), where a is the radius of the base and b is the height of the half-spheroid.
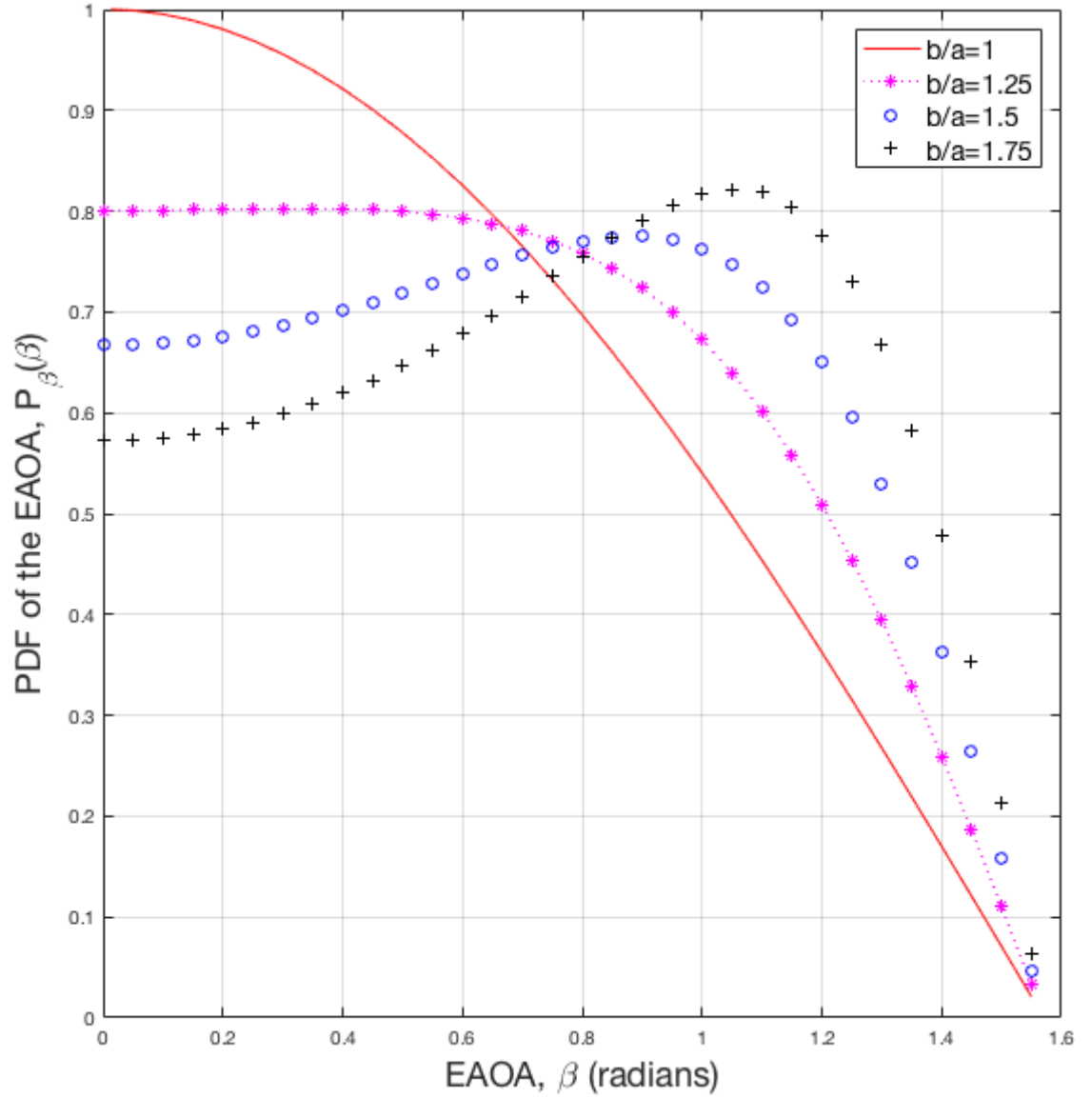
Figure 3.4: The 3-D isotropic half-spheroid PDF of the EAOA seen at the transducer for $\frac{b}{a} = 1$, 1.25, 1.5, and 1.75 (i.e. a prolate half spheroid), where a is the radius of the base and b is the height of the half-spheroid.

Further, if we consider the PDFs of the amplitude and phase of the *Rayleigh* process as defined by (3.6), we know from [53] that the amplitude PDF is given by

$$p_\zeta(z) = \frac{z}{\sigma_0^2} e^{-\frac{z^2}{2\sigma_0^2}}, z \geq 0 \tag{3.9}$$

and the phase PDF may be obtained as the uniform distribution

$$p_\theta(\theta) = \frac{1}{2\pi}. \tag{3.10}$$

3.2.2.2 Temporal ACF

The normalised temporal ACF $r_{\mu_i\mu_i}(\tau)$ of $\mu_i(t)$ where $(i = 1, 2)$ is defined as the ensemble average $E[.]$ of the received band pass signal $\mu_i(t)$ with itself at a time separation τ when $\mu_i(t)$ is Wide Sense Stationary (WSS) [54]. As shown by (C.12) in Appendix C, the temporal ACF can be derived as [61]

$$r_{\mu_i\mu_i}(\tau) = \int_0^{\frac{\pi}{2}} J_0(2\pi f_{D_{max}}\tau \cos\beta) \cdot \left[\frac{\left(\frac{b}{a}\right)^2 \cos(\beta)}{\left[\sin^2\beta + \left(\frac{b}{a}\right)^2 \cos^2\beta \right]^{\frac{3}{2}}} \right] d\beta \tag{3.11}$$

where $f_{D_{max}}$ is the maximum *Doppler* frequency, β is the EAOA and $J_0(.)$ denotes the zeroth-order Bessel function of the first kind.

The normalised theoretical temporal ACF is plotted in Fig. 3.5 for $\frac{b}{a}$ values of 0.5, 0.75, 1, 1.25 and 1.5. The plot demonstrates how the ACF changes over a range of oblate and prolate half-spheroid model configurations.
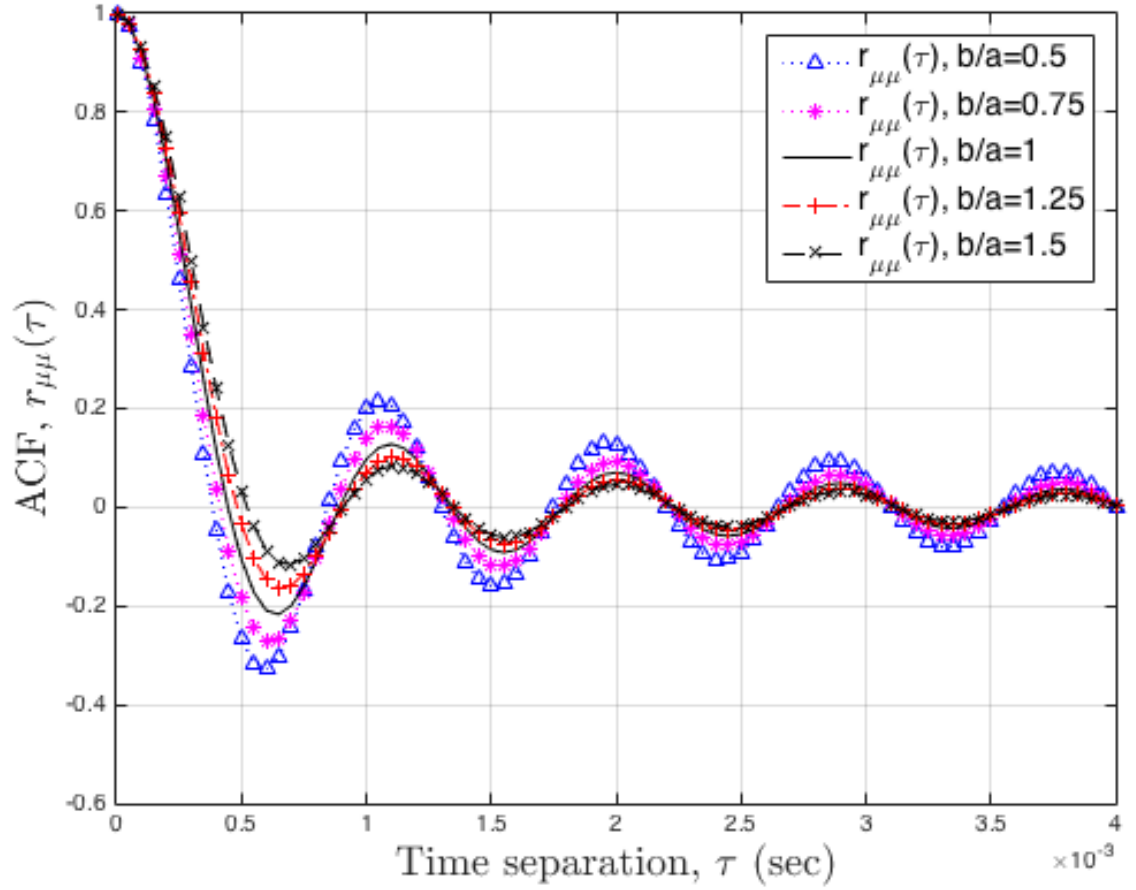
Figure 3.5: The 3-D isotropic half-spheroid theoretical ACF for $\frac{b}{a} = 0.5$, 0.75, 1, 1.25, and 1.5, where a is the radius of the base and b is the height of the half-spheroid.

In the remaining analysis, the special case $a = b$ will be used. In this case, (3.11) becomes

$$r_{\mu_i \mu_i}(\tau) = \int_0^{\frac{\pi}{2}} J_0(2\pi f_{D_{max}} \tau \cos \beta) \cdot \cos(\beta) \mathrm{d}\beta \tag{3.12}$$

Using the definitions at 6.681.1 and 8.411.11 of [63] gives us

$$r_{\mu_i \mu_i}(\tau) = \frac{\pi}{2} J_{\frac{1}{2}}(\pi f_{D_{max}} \tau) \cdot J_{-\frac{1}{2}}(\pi f_{D_{max}} \tau) \tag{3.13}$$

where

$$J_v(x) = \frac{2}{\pi} \int_0^\infty sin(x \cosh t - \frac{v\pi}{2}) \cosh vt \mathrm{d}t \tag{3.14}$$

3.2.2.3 *Doppler* PSD

The *Doppler* PSD $(S_{\mu_i\mu_i}(f))$ is the average power of the channel as a function of the *Doppler* frequency, f_D. It is derived as the *Fourier* transform of the ACF $r_{\mu_i\mu_i}(\tau)$ and is obtained as

$$S_{\mu_i\mu_i}(f) = \int_{-\infty}^{\infty} r_{\mu_i\mu_i}(\tau)e^{-j2\pi f\tau}d\tau \tag{3.15}$$

Two important characteristics of the *Doppler* PSD are the *Doppler* shift $B_{\mu_i\mu_i}^{(1)}$ and the *Doppler* spread $B_{\mu_i\mu_i}^{(2)}$ [53]. The *Doppler* shift $B_{\mu_i\mu_i}^{(1)}$ is given by

$$B_{\mu_i\mu_i}^{(1)} = \frac{\int_{-\infty}^{\infty} f S_{\mu_i\mu_i}(f)\,df}{\int_{-\infty}^{\infty} S_{\mu_i\mu_i}(f)\,df} \tag{3.16}$$

The *Doppler* spread $B_{\mu_i\mu_i}^{(2)}$ is given by

$$B_{\mu_i\mu_i}^{(2)} = \sqrt{\frac{\int_{-\infty}^{\infty} \left(f - B_{\mu_i\mu_i}^{(1)}\right) S_{\mu_i\mu_i}(f)\,df}{\int_{-\infty}^{\infty} S_{\mu_i\mu_i}(f)\,df}}. \tag{3.17}$$

Doppler shift is a measure of the degree of frequency shift introduced by multi-path fading, where as *Doppler* spread is the average frequency shift that the signal experiences during transmission over the multi-path channel. These are important because they quantify the degree of frequency dispersion experienced by the channel as a result of the rate and direction of movement of scatterers. $B_{\mu\mu}^{(1)}$ and $B_{\mu\mu}^{(2)}$ can also be calculated using the temporal ACF and its time derivatives [59], defined by

$$B_{\mu_i\mu_i}^{(1)} = \frac{1}{2\pi j} \cdot \frac{\dot{r}_{\mu_i\mu_i}(0)}{r_{\mu_i\mu_i}(0)} \tag{3.18}$$

and

$$B_{\mu_i\mu_i}^{(2)} = \frac{1}{2\pi}\sqrt{\left(\frac{\dot{r}_{\mu_i\mu_i}(0)}{r_{\mu_i\mu_i}(0)}\right)^2 - \frac{\ddot{r}_{\mu_i\mu_i}(0)}{r_{\mu_i\mu_i}(0)}}. \tag{3.19}$$

3.2.2.4 Envelope LCR & AFD

The envelope LCR, denoted $L(r)$, is defined as a measure of the rate at which the received complex envelope crosses a specified level r in the positive or negative

going direction, such that the LCR is the average number of up or down crossings through r per second. The $L(r)$ can be derived by considering two uncorrelated real-valued zero-mean *Gaussian* random processes, $\mu_1(t)$ and $\mu_2(t)$, where $R(t)$ is the absolute value of this process, such that $\mu(t) = \mu_1(t) + \mu_2(t)$ and $R(t) = |\mu(t)|$. Using a procedure similar to that described in [53] we start by finding the joint probability function for the stationary processes $\mu_{P_1}(t)$, $\mu_{P_2}(t)$, $\mu_{\dot{P}_1}(t)$, and $\mu_{\dot{P}_1}(t)$, i.e. $p_{\mu_{P_1}\mu_{P_2}\dot{\mu}_{P_1}\dot{\mu}_{P_2}}(x_1, x_2, \dot{x}_1, \dot{x}_2)$. Based on the following characteristics and assumptions,

$$r_{\mu_1\mu_1}(\tau) \neq r_{\mu_2\mu_2}(\tau), \tau \neq 0 \tag{3.20}$$

$$E\left[\mu_{p_i}(t)\right] = m_i = 0 \tag{3.21}$$

$$var\left[\mu_{p_i}(t)\right] = var\left[\mu_i(t)\right] = r_{\mu_i\mu_i}(0) = \sigma_i^2 \tag{3.22}$$

$$E\left[\dot{\mu}_{p_i}(t)\right] = 0 \tag{3.23}$$

$$var\left[\dot{\mu}_{p_i}(t)\right] = r_{\dot{\mu}_i\dot{\mu}_i}(0) = -\ddot{r}_{\mu_i\mu_i}(0) = \beta_i \tag{3.24}$$

where $\dot{\mu}_{p_i}(t)$ is the first derivative of $\mu_{p_i}(t)$, the joint probability is given by

$$p_{\mu_{P_1}\mu_{P_2}\dot{\mu}_{P_1}\dot{\mu}_{P_2}}(x_1, x_2, \dot{x}_1, \dot{x}_2) = \frac{e^{-\frac{x_1-m_1}{2\sigma_1^2}}}{\sqrt{2\pi}\sigma_1} \cdot \frac{e^{-\frac{x_2-m_2}{2\sigma_2^2}}}{\sqrt{2\pi}\sigma_2} \cdot \frac{e^{-\frac{\dot{x}_1}{2\beta_1^2}}}{\sqrt{2\pi}\beta_1} \cdot \frac{e^{-\frac{\dot{x}_2}{2\beta_2^2}}}{\sqrt{2\pi}\beta_2} \tag{3.25}$$

which can then be simplified to

$$p_{\mu_{P_1}\mu_{P_2}\dot{\mu}_{P_1}\dot{\mu}_{P_2}}(x_1, x_2, \dot{x}_1, \dot{x}_2) = \frac{e^{-\frac{x_1}{2\sigma_1^2}}}{\sqrt{2\pi}\sigma_1} \cdot \frac{e^{-\frac{x_2}{2\sigma_2^2}}}{\sqrt{2\pi}\sigma_2} \cdot \frac{e^{-\frac{\dot{x}_1}{2\beta_1^2}}}{\sqrt{2\pi}\beta_1} \cdot \frac{e^{-\frac{\dot{x}_2}{2\beta_2^2}}}{\sqrt{2\pi}\beta_2} \tag{3.26}$$

using $m_1 = m_2 = 0$ for a *Rayleigh* process.

To make use of (3.26), a transformation from *Cartesian* coordinates (x_1, x_2) to polar coordinates (z, θ) is required in order to get $p_{R\dot{R}\theta\dot{\theta}}(R, \dot{R}, \theta, \dot{\theta})$, from which the joint PDF of $R(t)$, $p_{R\dot{R}}(R, \dot{R})$ can be found. The LCR is defined as

$$L(r) = \int_0^\infty \dot{R} \cdot p_{R,\dot{R}}(r, \dot{R}) d\dot{R}. \tag{3.27}$$

Using a Jacobian determinant, $p_{R\dot{R}}(r, \dot{R})$ can be found as

$$p_{R\dot{R}}(r, \dot{R}) = \frac{r}{(2\pi)^{\frac{3}{2}} \sigma_1 \sigma_2} \int_{-\pi}^{\pi} \frac{1}{\sqrt{(\beta_1 \cos^2 \theta + \beta_2 \sin^2 \theta)}} \cdot$$
$$e^{-r^2 \left[\frac{(\sigma_2^2 \cos^2 \theta + \sigma_1^2 \sin^2 \theta)}{2\sigma_1^2 \sigma_2^2}\right]} \cdot e^{-\dot{R}^2 \left[\frac{1}{2(\beta_1 \cos^2 \theta + \beta_2 \sin^2 \theta)}\right]} d\theta \tag{3.28}$$

By substituting (3.28) into (3.27), the expression for $L(r)$ can be derived as

$$L(r) = \frac{r}{(2\pi)^{\frac{3}{2}} \sigma_1 \sigma_2} \int_{-\pi}^{\pi} \sqrt{(\beta_1 \cos^2 \theta + \beta_2 \sin^2 \theta)} \cdot e^{-r^2 \left[\frac{(\sigma_2^2 \cos^2 \theta + \sigma_1^2 \sin^2 \theta)}{2\sigma_1^2 \sigma_2^2}\right]} d\theta \tag{3.29}$$

The average fade duration (AFD) is the amount of time that the received complex envelope remains below a specified level r and is denoted by $T(r)$. In general, the AFD is defined as

$$T(r) = \frac{p_{R-}(r)}{L(r)} \tag{3.30}$$

where $p_{R-}(r)$ indicates that the process $R(t)$ is found below the level r, i.e. $p_{R-}(r) = p[R(t) \leq r]$, as discussed in [53], such that

$$p_{R-}(r) = \int_0^r p_R(R) dR \tag{3.31}$$

and

$$p_R(r) = \int_{-\infty}^{\infty} p_{R\dot{R}}(r, \dot{R}) d\dot{R}. \tag{3.32}$$

Solving (3.32) and substituting into (3.31) gives

$$p_{R-}(r) = \int_0^r \frac{R}{\sigma_1^2 \sigma_2^2} e^{\frac{-R^2}{4\sigma_1^2}} I_0 \left[\frac{R^2}{4} \left(\frac{1}{\sigma_2^2} - \frac{1}{\sigma_1^2}\right)\right] dR \tag{3.33}$$

where I_0 is a zeroth-order modified Bessel function of the first kind. Since $R(t)$ is a *Rayleigh* process and the variances $(\sigma_1 = \sigma_2) = \sigma_0$ and $(\beta_1 = \beta_2) = \beta_0$, then (3.29) can be reduced to

$$L_\zeta(r) = \frac{r}{(2\pi)^{\frac{3}{2}} \sigma_0^2} \int_{-\pi}^{\pi} \sqrt{\beta_0} \cdot e^{-r^2 \left(\frac{\sigma_0^2}{2\sigma_0^4}\right)} d\theta \tag{3.34}$$

63

and further simplified to

$$L_\zeta(r) = \sqrt{\frac{\beta_0}{2\pi}} \cdot \frac{r}{\sigma_0^2} \cdot e^{-\frac{r^2}{2\sigma_0^2}}, r \geq 0. \tag{3.35}$$

Similarly, the AFD for a *Rayleigh* process can be derived by substituting (3.33) and (3.34) into (3.30), and solving to give

$$T_\zeta(r) = \sqrt{\frac{2\pi}{\beta_0}} \cdot \frac{\sigma_0^2}{r} \cdot \left(e^{\frac{r^2}{2\sigma_0^2}} - 1 \right), r \geq 0. \tag{3.36}$$

3.3   Simulation Model

In this section a SoS simulation model is proposed. The simulation model emulates signals received at the transducer in a TCD ultrasound system using the theoretical half-spheroid model as a reference. The simulated receive signal $\hat{\mu}(t)$ has in-phase and quadrature components such that

$$\hat{\mu}(t) = \hat{\mu}_1(t) + j\hat{\mu}_2(t). \tag{3.37}$$

The real-valued SoS *Gaussian* stochastic process $\hat{\mu}_i(t)$ can be approximated by

$$\hat{\mu}_i(t) = \sum_{n=1}^{N_i} C_{i,n} \cos(2\pi f_{i,n}t + \theta_{i,n}), i = 1, 2 \tag{3.38}$$

where $C_{i,n}$ represents the gains, $(2\pi f_{i,n}t)$ the *Doppler* frequencies and $\theta_{i,n}$ the phases of N_i respective exponential functions.

3.3.1   MEDS for Parameterisation of the Proposed SoS Simulation Model

The simulation model parameters must be determined such that the process given by (3.38) has the desired statistics. For simplicity and to provide a good approximation to *Rayleigh* scattering in accordance with the *Jakes* method for SoS [56], the method of exact *Doppler* spread (MEDS) [64] is used to compute these statistics. The

parameters in (3.38) are generated using the following expressions;

$$C_{i,n} = \sigma\sqrt{\frac{2}{N_i}}, \tag{3.39}$$

$$f_{i,n} = f_{D_{max}}\cos\psi_n = f_{D_{max}}\cos\alpha_n\cos\beta_n, \tag{3.40}$$

$$\text{and } \theta_{i,n} = 2\pi\frac{n}{N_i + 1} \tag{3.41}$$

where $C_{i,n}$ represents the gains, $f_{i,n}$ the *Doppler* frequencies, α_n and β_n the discrete azimuth and elevation angles, and $\theta_{i,n}$ the discrete phases of N_i respective sinusoids. A random generator uniformly distributed over the interval $(0, 2\pi)$ can be used to derive values of $\theta_{i,n}$. The values for $f_{D_{max}}$ and σ are identical to the reference model. These parameters are kept constant during the simulation and the model statistical properties are derived by using time averaging instead of statistical averaging. In the analysis that follows N_i is assumed to equal for both *Gaussian* random processes $\mu_1(t)$ and $\mu_2(t)$, such that $N_i = N$.

3.3.2 Statistical Properties of the Simulation Model

Using the theoretical model and its corresponding statistical properties, it is possible to derive the properties of the simulation model.

3.3.2.1 Amplitude PDF

As defined in (B.50) in Appendix B.2, the amplitude PDF of the SoS simulation model becomes

$$\hat{p}_{\hat{\zeta}}(z) = (2\pi)^2 z \int_0^\infty \left[\prod_{n=1}^N J_0\left(2\pi|C_n|x\right)\right] J_0\left(2\pi zx\right)x\mathrm{d}x. \tag{3.42}$$

3.3.2.2 Temporal ACF

The closed form expression for the simulated ACF is given by [61] as

$$\hat{r}_{\hat{\mu}_i\hat{\mu}_i}(\tau) = \sum_{n=1}^N \frac{C_n^2}{2}\cos(2\pi f_{D_{max}}\tau\cos\alpha_n\cos\beta_n). \tag{3.43}$$

The parameters α_n and β_n in (3.43) must be evaluated for the simulation model such that the theoretical and simulated temporal ACFs are a close match. These parameters can be determined using an error minimising function, such as the Lp-norm method of parameter computation (LPNM) [53]. The parameter β_n can be found using the closed form expressions for the theoretical and simulated spatial cross-correlation function (CCF) [61], given as

$$\rho(D) = \int\limits_{0}^{\frac{\pi}{2}} \exp(j2\pi\frac{D}{\lambda}\sin\beta)p_\beta(\beta)d\beta \tag{3.44}$$

and

$$\hat{\rho}(D) = \frac{1}{N}\sum_{n=1}^{N} e^{-j2\pi\frac{D}{\lambda}\sin\beta_n}. \tag{3.45}$$

In (3.44) and (3.45), the spatial CCF is calculated at a separation distance D. Using an arbitrary spatial separation of an integral number of wavelengths allows parameter β_n to be evaluated using the error function

$$E_1^{(p)} = \left[\int\limits_{0}^{D_{max}} |\rho(D) - \hat{\rho}(D)|^p\,dD\right]^{\frac{1}{p}}. \tag{3.46}$$

Similarly, the parameter α_n can then be calculated using theoretical and simulated ACFs, given by (3.12) and (3.43), and the LPNM error function,

$$E_2^{(p)} = \left[\int\limits_{0}^{\tau_{max}} |r_{\mu\mu}(\tau) - \hat{r}_{\hat{\mu}\hat{\mu}}(\tau)|^p\,d\tau\right]^{\frac{1}{p}}. \tag{3.47}$$

3.3.2.3 *Doppler* PSD

The closed form expression for the simulated PSD is simply the *Fourier* transform of the simulated ACF and is given by

$$\hat{S}_{\hat{\mu}_i\hat{\mu}_i}(f) = \int\limits_{-\infty}^{\infty} \hat{r}_{\hat{\mu}_i\hat{\mu}_i}(\tau)e^{-j2\pi f\tau}\mathrm{d}\tau. \tag{3.48}$$

In a similar process to that described in section 3.2.2.3, the *Doppler* shift $\hat{B}^{(1)}_{\hat{\mu}_i\hat{\mu}_i}$ is given by

$$\hat{B}^{(1)}_{\hat{\mu}_i\hat{\mu}_i} = \frac{1}{2\pi j} \cdot \frac{\dot{\hat{r}}_{\hat{\mu}_i\hat{\mu}_i}(0)}{\hat{r}_{\hat{\mu}_i\hat{\mu}_i}(0)} \tag{3.49}$$

and the *Doppler* spread $\hat{B}^{(2)}_{\hat{\mu}_i\hat{\mu}_i}$ is given by

$$\hat{B}^{(2)}_{\hat{\mu}_i\hat{\mu}_i} = \frac{1}{2\pi}\sqrt{\left(\frac{\dot{\hat{r}}_{\hat{\mu}_i\hat{\mu}_i}(0)}{\hat{r}_{\hat{\mu}_i\hat{\mu}_i}(0)}\right)^2 - \frac{\ddot{\hat{r}}_{\hat{\mu}_i\hat{\mu}_i}(0)}{\hat{r}_{\hat{\mu}_i\hat{\mu}_i}(0)}}. \tag{3.50}$$

By solving (3.49) and (3.50), it can be shown that $\hat{B}^{(1)}_{\hat{\mu}_i\hat{\mu}_i}$ and $\hat{B}^{(2)}_{\hat{\mu}_i\hat{\mu}_i}$ are given by [53, 61]

$$\hat{B}^{(1)}_{\hat{\mu}_i\hat{\mu}_i} = 0 \tag{3.51}$$

and

$$\hat{B}^{(2)}_{\hat{\mu}_i\hat{\mu}_i} = \sqrt{\frac{1}{N}\sum_{n=1}^{N} f^2_{D_{max}} \cos^2\alpha_n \cos^2\beta_n}. \tag{3.52}$$

respectively, for $i = 1, 2$.

3.3.2.4 Envelope LCR & AFD

Using a similar approach to that followed in section 3.2.2.4, $\hat{\mu}_1(t)$ and $\hat{\mu}_2(t)$ are two uncorrelated real-valued zero-mean *Gaussian* random processes. The simulated *Rayleigh* process is given by $\hat{\zeta}(t) = |\hat{\mu}(t)| = |\hat{\mu}_1(t) + \hat{\mu}_2(t)|$, and the variances are $(\sigma_1 = \sigma_2) = \sigma_0$ and $(\beta_1 = \beta_2) = \beta_0$. The simulated LCR, $\hat{L}_{\hat{\zeta}}(r)$, can be derived as

$$\hat{L}_{\hat{\zeta}}(r) = \sqrt{\frac{\beta_0}{2\pi}} \cdot \hat{p}_{\hat{\zeta}}(r), r \geq 0 \tag{3.53}$$

where $\hat{p}_{\hat{\zeta}}(r)$ is given by (3.42). This allows the expressions for the simulated LCR to be given by

$$\hat{L}_{\hat{\zeta}}(r) = \sqrt{\frac{\beta_0}{2\pi}} \cdot \frac{r}{\sigma_0^2} \cdot e^{-\frac{r^2}{2\sigma_0^2}}, r \geq 0 \tag{3.54}$$

from the simplification of the expression for the amplitude PDF of the envelope of a *Rayleigh* process, as given by (B.51) in Appendix B.2. Similarly, the simulated

AFD, $\hat{T}_{\hat{\zeta}}(r)$, can be derived as

$$\hat{T}_{\hat{\zeta}}(r) = \sqrt{\frac{2\pi}{\beta_0} \cdot \frac{\sigma_0^2}{r} \cdot \left(e^{\frac{r^2}{2\sigma_0^2}} - 1 \right)}, r \geq 0. \tag{3.55}$$

Therefore, expressions (3.54) and (3.55) converge with the theoretical equivalents, as given by (3.35) and (3.36)

3.4 Numerical Results & Analysis

In this section we present and analyse the 3-D models, comparing the theoretical, simulation, and numerical results. Fig. 3.6 and Fig. 3.7 show plots for the amplitude and normalised phase PDFs of the theoretical reference model, simulation model and SoS simulation, where $\frac{b}{a} = 1$, $f_{D_{max}} = 1.07$ kHz, $\sigma^2 = 1$, and $N = 30$. It is clear from the close agreement of these plots that the SoS channel simulator provides a very strong agreement with the theoretical reference, and the models clearly follow a *Rayleigh* distribution as designed.
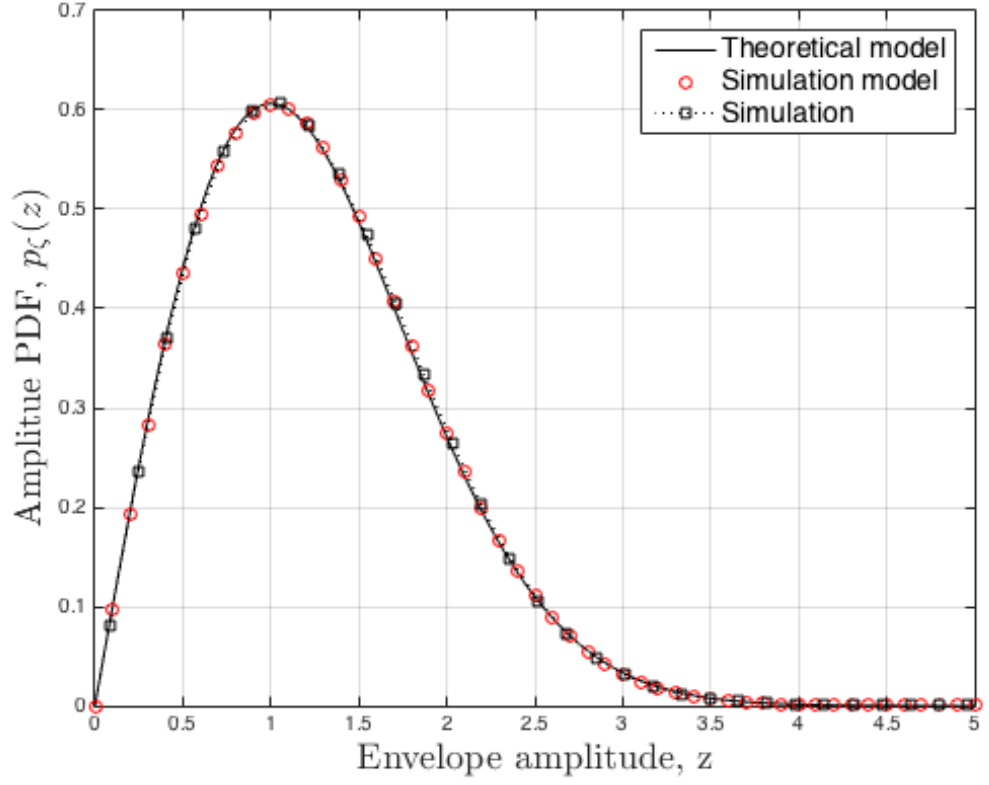
Figure 3.6: The amplitude PDF of the 3-D isotropic half-spheroid theoretical reference, simulation, and SoS simulation results, where $\frac{b}{a} = 1$, $f_{D_{max}} = 1.07$ kHz, $\sigma^2 = 1$, and $N = 30$.
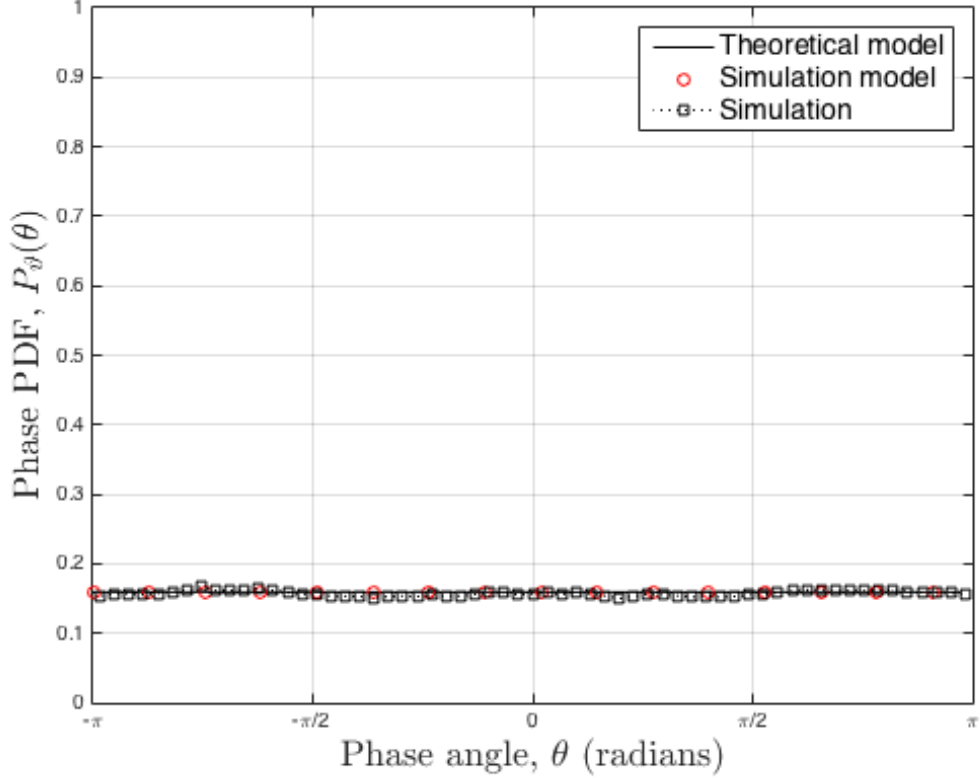
Figure 3.7: The phase PDF of the 3-D isotropic half-spheroid theoretical reference, simulation, and SoS simulation results, where $\frac{b}{a} = 1$, $f_{D_{max}} = 1.07$ kHz, $\sigma^2 = 1$, and $N = 30$.

The level of agreement of the ACFs must be considered in terms of the accuracy of estimation of the α_n and β_n parameters using the LPNM. Fig. 3.8 shows the plots of the theoretical reference and simulation model CCFs for $N = 30$ and $D_{max} = 4\lambda$. This process has been optimised for parameter β_n and the theoretical reference model shows good agreement with the simulation model.
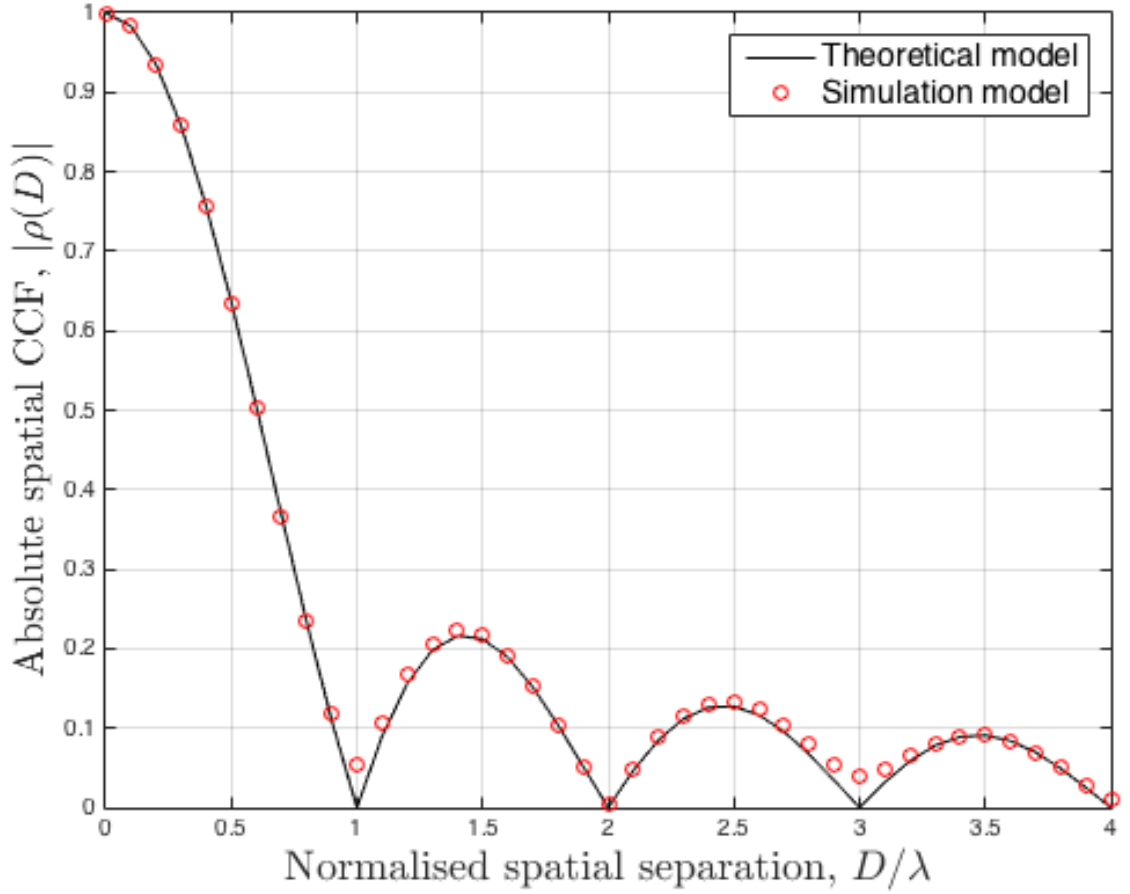
Figure 3.8: A plot of the theoretical and simulated spatial CCFs for the 3-D half-spheroid model for $N = 30$ and $D_{max} = 4\lambda$.

In Fig. 3.9, the ACFs of the theoretical reference model, simulation model and SoS simulation are plotted using the resulting parameter α_n, where $\frac{b}{a} = 1$, $f_{D_{max}} = 1.07$ kHz, $\sigma^2 = 1$, and $N = 30$. This plot shows strong agreement up to a temporal separation period of approximately 0.8 ms, after which the simulation results begin to diverge from the theoretical model. This period of agreement is a function of N, such that as $(N \to \infty)$, so $\hat{r}_{\hat{\mu}_i \hat{\mu}_i}(\tau) \to r_{\mu_i \mu_i}(\tau)$.
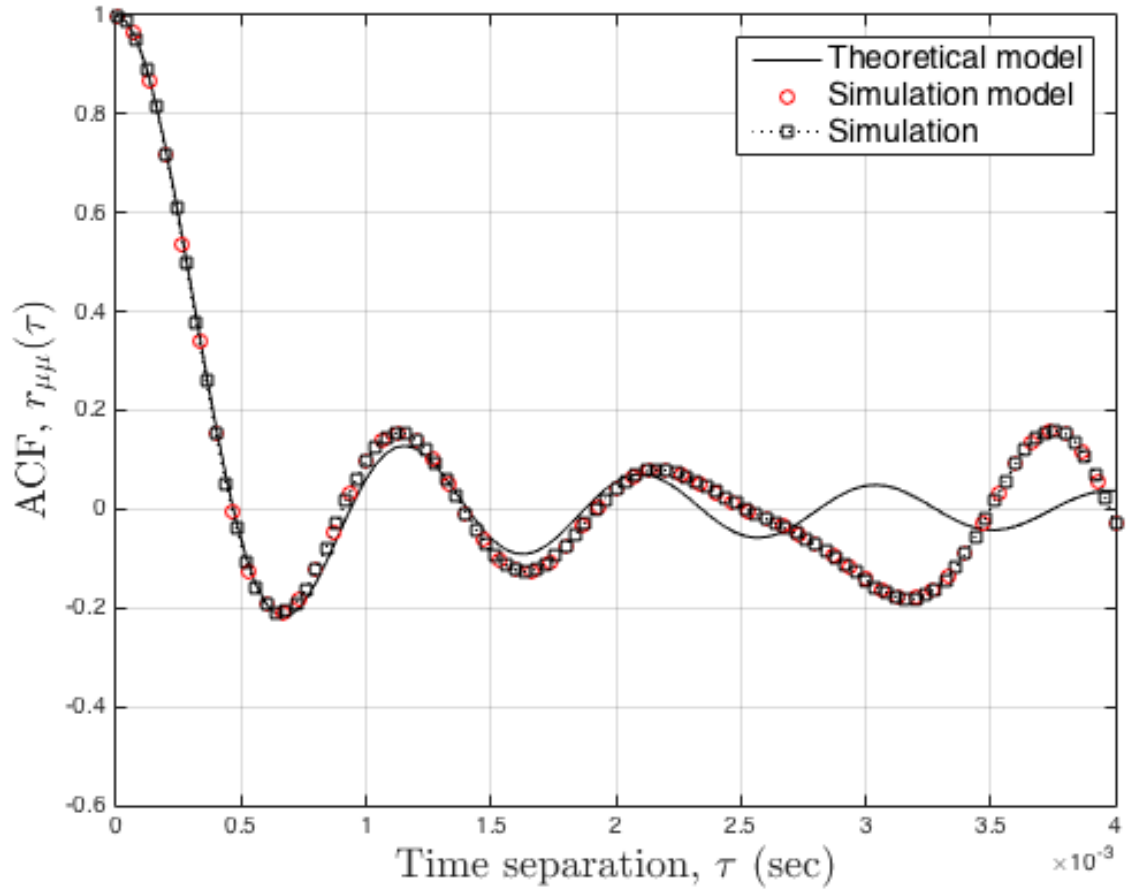
Figure 3.9: The ACF of the 3-D isotropic half-spheroid theoretical reference, simulation, and SoS simulation results, where $\frac{b}{a} = 1$, $f_{D_{max}} = 1.07$ kHz, $\sigma^2 = 1$, and $N = 30$.

The plots of the normalised envelope LCRs and AFDs of the theoretical reference model, simulation model and SoS simulation are shown in Fig. 3.10 and Fig. 3.11 respectively, where $\frac{b}{a} = 1$, $f_{D_{max}} = 1.07$ kHz, $\sigma^2 = 1$, and $N = 30$. These plots demonstrate very close agreement. This is perhaps unsurprising given the convergence of the simplified expressions for the theoretical and simulated models, however this is re-enforced by the agreement of the SoS simulation, which also demonstrates the same close agreement.
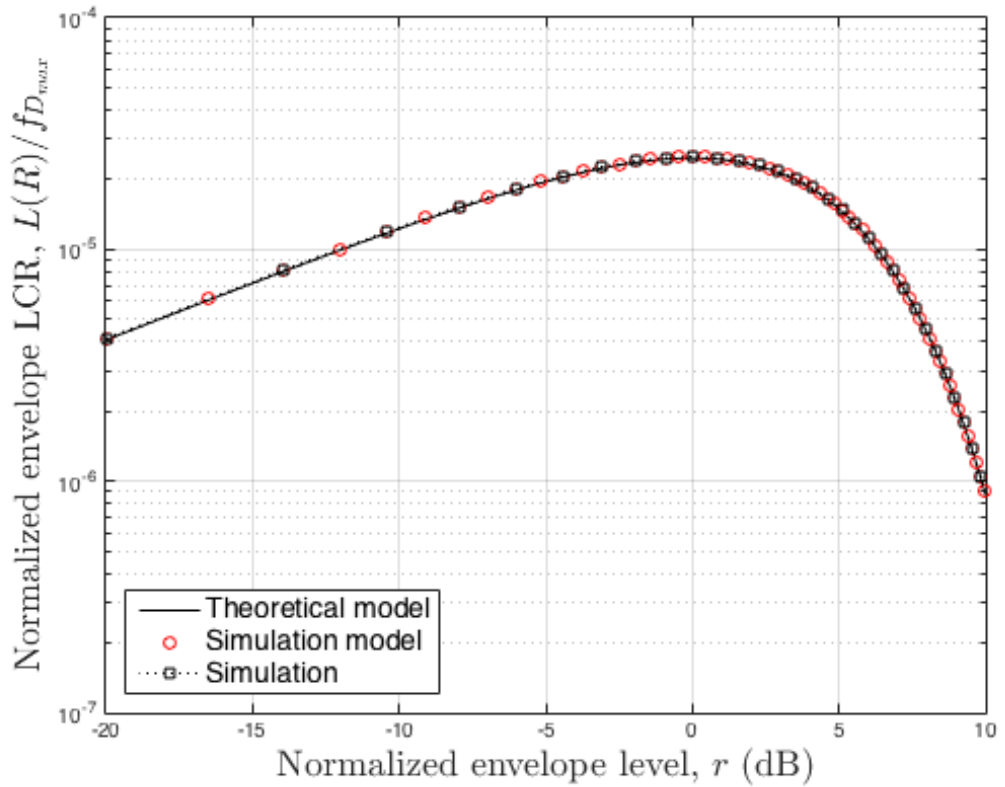
Figure 3.10: The LCR of the 3-D isotropic half-spheroid theoretical reference, simulation, and SoS simulation results, where $\frac{b}{a} = 1$, $f_{D_{max}} = 1.07$ kHz, $\sigma^2 = 1$, and $N = 30$.
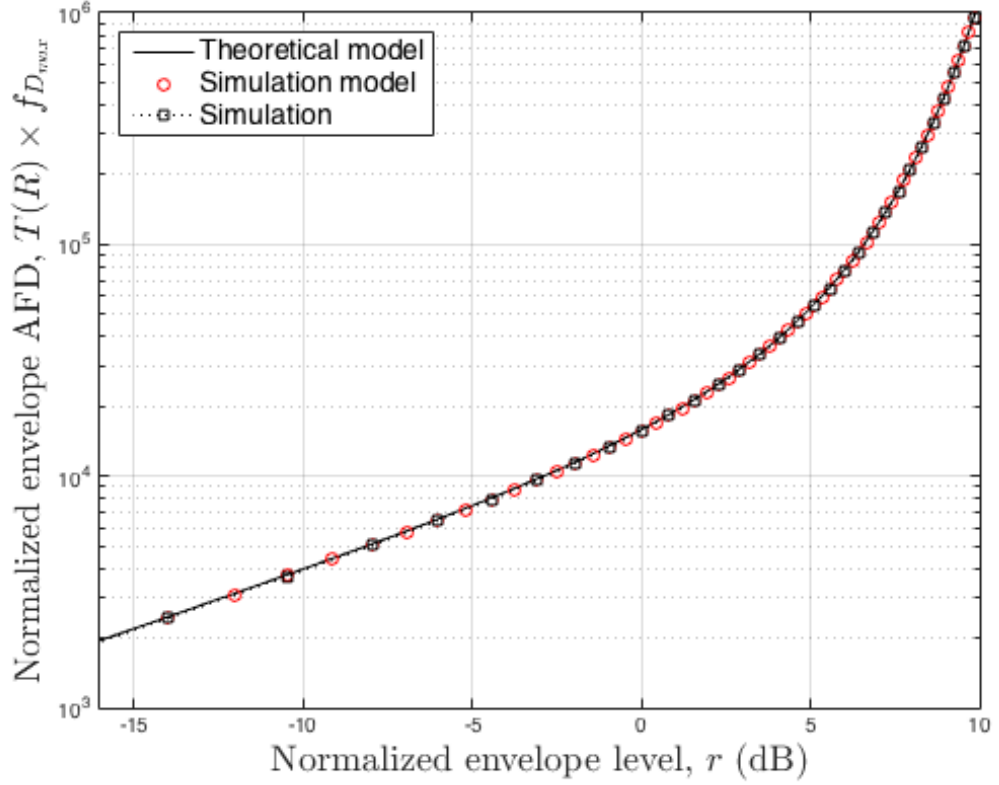
Figure 3.11: The AFD of the 3-D isotropic half-spheroid theoretical reference, simulation, and SoS simulation results, where $\frac{b}{a} = 1$, $f_{D_{max}} = 1.07$ kHz, $\sigma^2 = 1$, and $N = 30$.

Although the results achieved from the theoretical reference model, simulation model and SoS channel simulator are promising, there are a number of fundamental disadvantages of these 3-D isotropic TCD ultrasound propagation channel models. Firstly, although theoretically it can be predicted that the backscattered power from blood demonstrates *Rayleigh* scattering at TCD insonation frequencies (section 2.5.2), these isotropic models are not adaptable to the presence of a significant LoS scattering component. The complexities of human physiology and the practical difficulties of ultrasound measurements require a more flexible approach that can be adapted to measured results. Models that include a LoS component are likely to be more configurable, provide better optimisation capabilities, and higher accuracy. Secondly, the derivation of the ACF requires the estimation of the spatial CCF at a

separation distance of an integral number of wavelengths from the transducer. This is difficult to verify experimentally using standard TCD systems. It requires the received signal to be obtained from individually addressable elements of a multi-element transducer array. This complexity arises from the requirement to jointly analyse the probability distribution in both azimuth and elevation angles. In the case described, this process was much simplified in the geometric model by the unrealistic assumption that the radius a and the base b dimensions were equal. Finally, although the LPNM method of parameter computation is known to offer high levels of accuracy and performance for SoS based isotropic scattering cases [53], in this case a more efficient and more optimal solution should be investigated for the 3-D non-isotropic case that provides better or equal accuracy, with increased simulation performance through lower values of N.

3.5   Summary

In this chapter, 3-D isotropic half-spheroid models have been proposed for investigation of the characteristics of a TCD ultrasound propagation channel based on methods developed for stochastic analysis of mobile communications systems. The stochastic characteristics of the models have been investigated and closed form expressions have been derived for the amplitude and phase PDFs, ACFs, LCRs and AFDs. The MEDS and LPNM functions were used to optimise the ACF simulations, and the simulation models achieve a good fit with the theoretical mathematical reference model. However, these models are relatively inflexible and may be difficult to adapt to the TCD measurement environment. In Chapter 4 non-isotropic 3-D models are investigated.

Chapter 4

3-D Non-isotropic TCD Ultrasound Propagation Channel Models

4.1 Introduction

In this chapter 3-D theoretical and simulation models for statistical analysis of non-isotropic TCD ultrasound propagation channels are described. Taking inspiration from 3-D geometry-based stochastic models (GBSMs) that have been developed for wireless communications systems [65, 66, 67, 68], in this chapter a TCD ultrasound channel model is developed that will lead to improved understanding of the spatial and temporal characteristics of TCD ultrasound.

Taking a similar approach to that described in Chapter 3 for 3-D isotropic models, the first stage of the analysis presented in this chapter is the development of a theoretical model of a non-isotropic channel that is a combination of LoS and NLoS components, and a spherical model. In order to remove the unrealistic assumption imposed by the 3-D isotropic propagation channel model that the probability distributions in the azimuth and elevation angles are independent, the *Von Mises-Fisher* (VMF) probability distribution [69, 70] is used to characterise the scattering distribution. However, this theoretical model will only be used as the starting point

for further analysis, since it assumes an infinite number of effective scatterers, and cannot be implemented in practice due to the corresponding complexities imposed. The second stage of the analysis presents a simulation model and a SoS channel simulator [55, 71]. The simulation model will be used to consider the effect of diffuse scattering based on single bounce signal reflections and a finite number of scatterers in the receive path. The azimuth and elevation angles of the simulation model are computed using the method of equal volume (MEV) [68]. Finally, the statistical properties of the SoS channel simulator are verified through comparison of the reference model, the simulated results.

4.2 Theoretical Reference Model

In the sub-sections that follow, a model geometry is developed based on a 3-D spheroid and the statistical properties of this theoretical model are investigated.

4.2.1 Model Geometry

Taking a similar approach to that described in Chapter 3 section 3.2, in this case the scattering geometry is elaborated by considering the propagation channel as a 3-D non-isotropic sphere, as shown in Fig. 4.1. Let us consider a single element ultrasound transducer which is assumed to be stationary and positioned at the origin of the Cartesian coordinates. Once again, the direction of blood flow in the insonation region is, without any loss of generality, assumed to be in the direction of the x axis with velocity v. The ultrasound system can be simplified to consider only the reflections from a strong scattering region within blood flow of an isonated vessel. Strong incident scatterers such as S_n are assumed to exist within and around the periphery of the spherical model. The signal received at the RF amplifier in this non-isotropic sphere will therefore be a combination of direct LoS and single-bounce NLoS components. The parameters shown in Fig. 4.1 and in the mathematical expressions that follow are defined in Table 4.1.
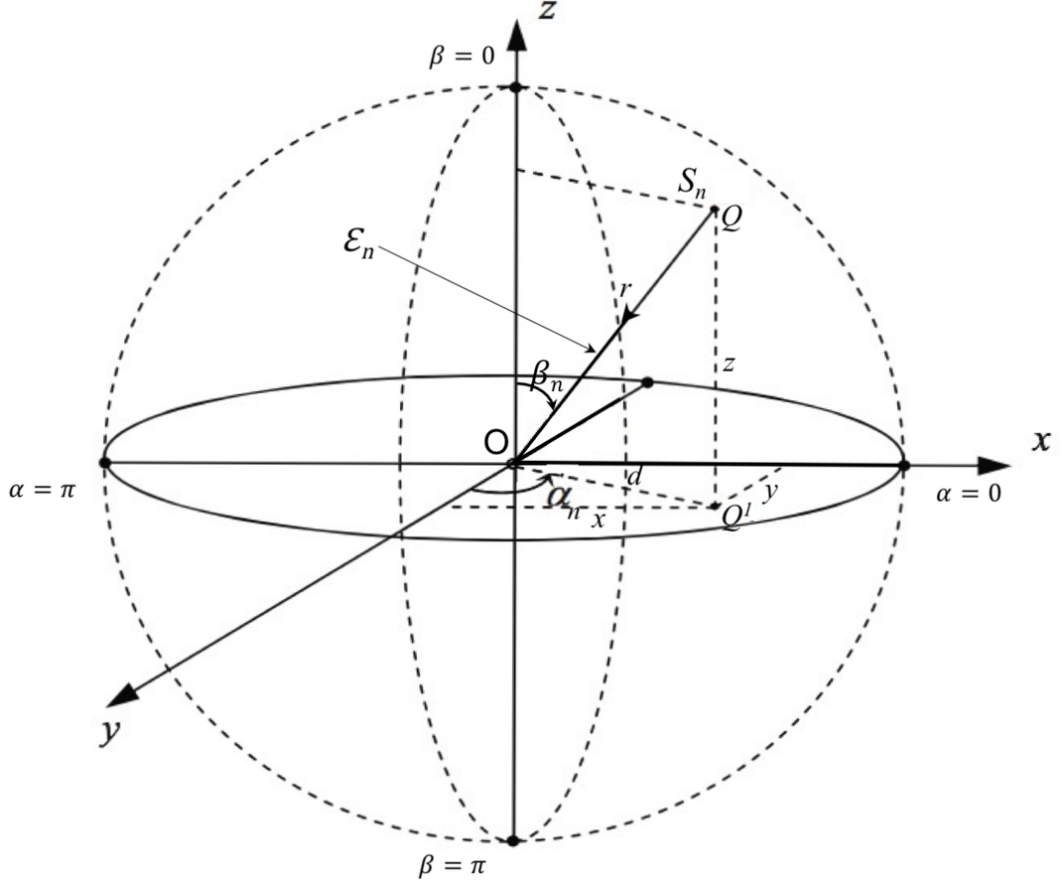
Figure 4.1: 3-D non-isotropic sphere; an incident scatterer S_n is shown in three-dimensional space ($\rho = 3$).

As in the isotropic case described in section 3.2.1, the direction of blood flow in the insonation region is, without any loss of generality, assumed to be in the direction of the x-axis with velocity v. Tissue is assumed to be homogeneous with uniform acoustic impedance. Echoes received from stationary tissue can be considered to exhibit the same frequency and phase as the transmitted signal. Echoes from scatterers (i.e. moving tissue and fluids) will exhibit slight differences in delay and/or phase. From these differences, the *Doppler* frequency is obtained which can then be processed to produce a *Doppler* sonogram. The NLoS complex received signal may be subject to refraction or diffraction by tissue objects in and around the insonation path, or reflection at tissue boundaries.

Table 4.1: Definition of parameters for 3-D non-isotropic sphere.

Parameter	Definition
α_n $[-\pi \leq \alpha_n \leq \pi]$	azimuth angle of arrival (AAoA) of the incident receive signal r
α_0 $[-\pi \leq \alpha_0 \leq \pi]$	mean azimuth angle of arrival (AAoA) of the receive signal r
β_n $[-\pi \leq \beta_n \leq \pi]$	elevation angle of arrival (EAoA) of the incident receive signal r
β_0 $[-\pi \leq \beta_0 \leq \pi]$	mean elevation angle of arrival (EAoA) of the receive signal r
c	speed of sound in the medium
ε_n	path distance of incident receive signal r
k $[k \geq 0]$	VMF concentration parameter
K	*Rician* K-factor
f_c	insonation frequency
$f_{D_{\max}}$	maximum *Doppler* frequency
N $[N \to \infty]$	number of incident scatterers
v	blood flow velocity within isonated vessel
τ_n	time for an incident wave to travel the path distance $\left(\frac{\varepsilon_n}{c}\right)$
θ_n	phase shift corresponding to incident scatterers path

The complex fading envelope is a superposition of a LoS component $m(t)$ and NLoS scattering components $n(t)$ and can be expressed as

$$\mu(t) = m(t) + n(t) \tag{4.1}$$

where

$$m(t) = \sqrt{\frac{K}{(K+1)}} e^{j2\pi f_{D_{\max}} t \cos\alpha_0 \cos\beta_0} \tag{4.2}$$

and

$$n(t) = \sqrt{\frac{1}{(K+1)}} \lim_{N\to\infty} \sum_{n=1}^{N} \frac{1}{\sqrt{N}} e^{j2\pi f_{D_{\max}} t \cos\alpha_n \cos\beta_n + \theta_n}. \tag{4.3}$$

In (4.2) and (4.3), K is the *Rician* K-factor, the ratio between the LoS and NLoS components, and N is the number of scatterers ($N \to \infty$). Furthermore, it is assumed phase θ_n is a random variable distributed in the interval $[-\pi, \pi]$.

In section 3.2.1, the scattering geometry was elaborated as a 3-D half-spheroid in which the probability distributions in azimuth and elevation were analysed separately. In this analysis the VMF distribution was used as a method of reducing complexity by jointly analysing azimuth and elevation angles in the probability distribution. The application of the VMF distribution to the scattering geometry shown in Fig. 4.1 is derived as (E.7) in Appendix E, where the probability density of a random unit vector in sample space S^2 is given by

$$f(\alpha, \beta) = \frac{k}{4\pi \sinh k} e^{kA} \cos \beta \qquad (4.4)$$

where

$$A = \left[\cos \beta \cos \beta_0 + \sin \beta \sin \beta_0 \cos (\alpha - \alpha_0) \right]. \qquad (4.5)$$

In (4.5) α, β, α_0 and β_0 represent the azimuth, elevation, mean azimuth, and mean elevation angles of the effective scatterer distribution respectively, where $\alpha \in [-\pi, \pi]$, $\beta \in [-\pi, \pi]$, $\alpha_0 \in [-\pi, \pi]$ and $\beta_0 \in [-\pi, \pi]$. The concentration parameter, k, is real valued and controls the concentration of the distribution relative to the mean angles, α_0 and β_0. For TCD, the region of interest reduces to a unit hemisphere corresponding to the maximum effective insonation angle of the transducer.

To demonstrate the VMF distribution and to show the effect of variation of the mean angles and k, Fig. 4.2 and Fig. 4.3 are presented. In Fig. 4.2(a) the 3-D VMF probability density function (PDF) is plotted for $\alpha_0 = 0°$, $\beta_0 = 0°$ and $k = 3$. For comparison, in Fig. 4.2(b) the 3-D VMF PDF is plotted for $\alpha_0 = 0°$, $\beta_0 = 60°$ and $k = 3$, showing how the distribution follows the mean angle of the received signal.
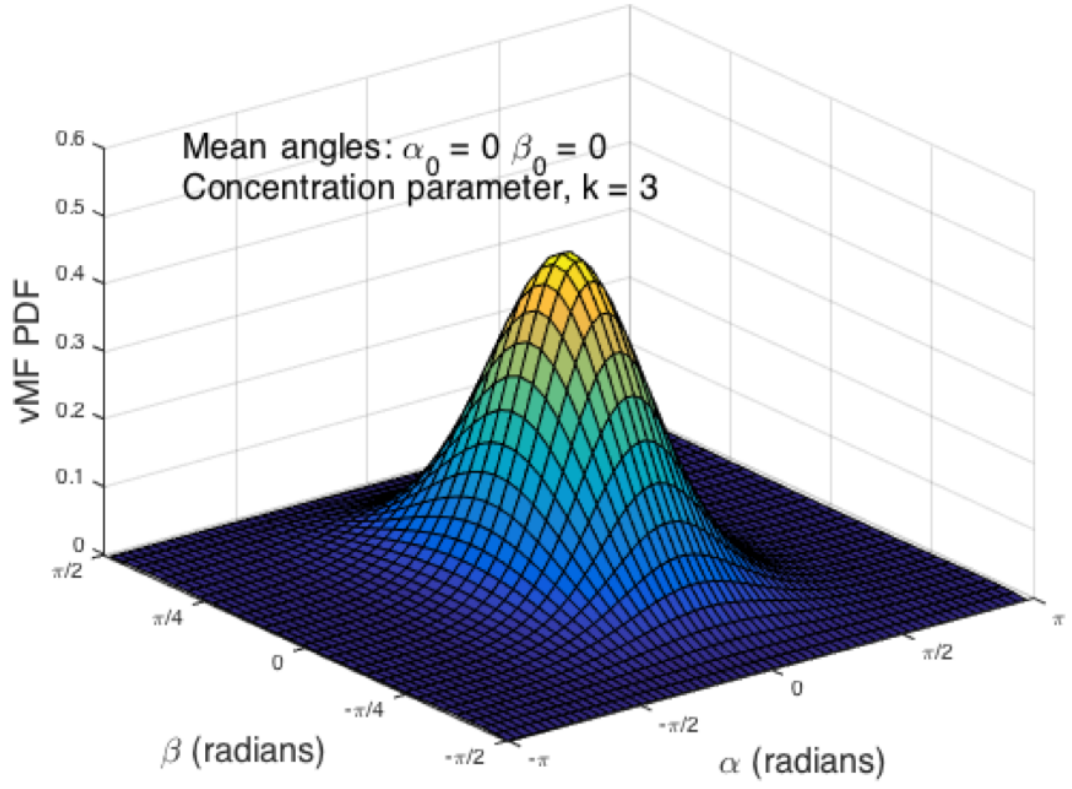
(a)
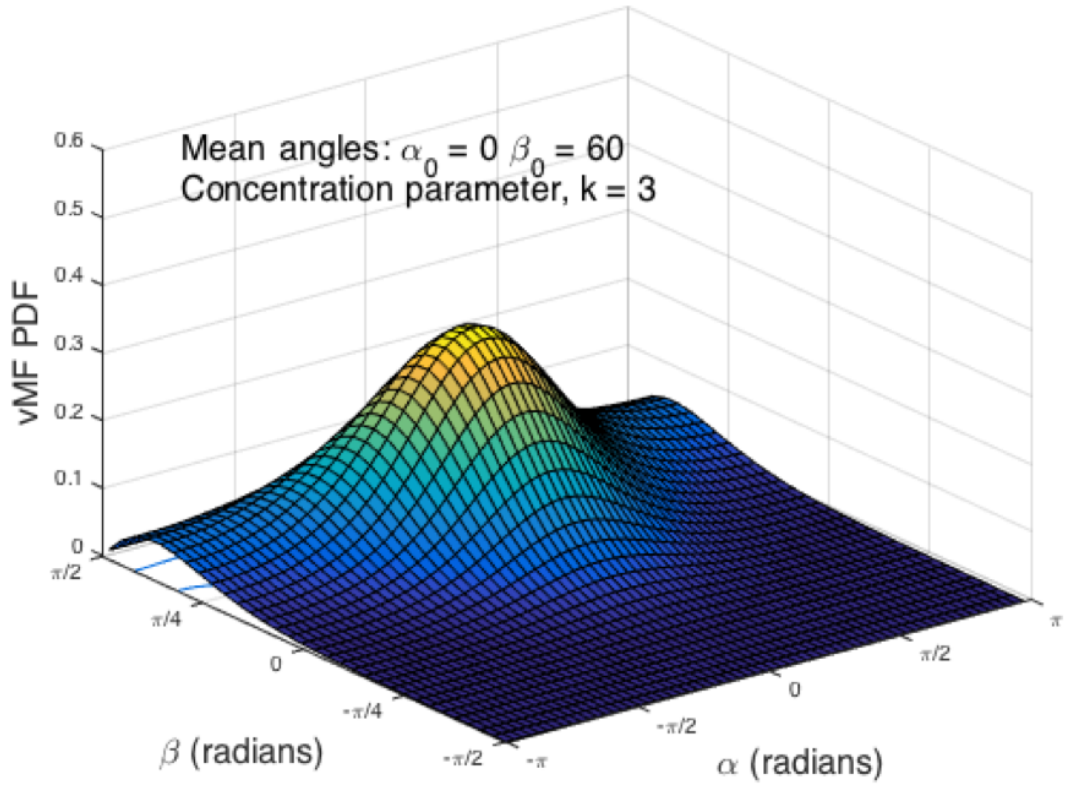
(b)

Figure 4.2: 3-D VMF PDF with (a) ($\alpha_0 = 0°, \beta_0 = 0°$, $k = 3$), and (b) ($\alpha_0 = 0°, \beta_0 = 60°$, $k = 3$).

In Fig. 4.3 we set the mean angles to ($\alpha_0 = 0°, \beta_0 = 30°$), and observe the effect on the scattering distribution when the concentration parameter is varied; (a) $k = 0$, (b) $k = 4$, and (c) $k = 200$. For $k = 0$ the VMF PDF is observed to be even over the surface of the sphere, however as k increases the VMF PDF is seen to be more concentrated towards the mean direction. For scattering analysis in TCD observations α_0, β_0, and k can be adapted to the propagation environment. Additionally, the K-factor can also be adjusted to the level of power observed in the scattered paths. The geometry of the proposed model can therefore be considered well characterised and highly flexible.
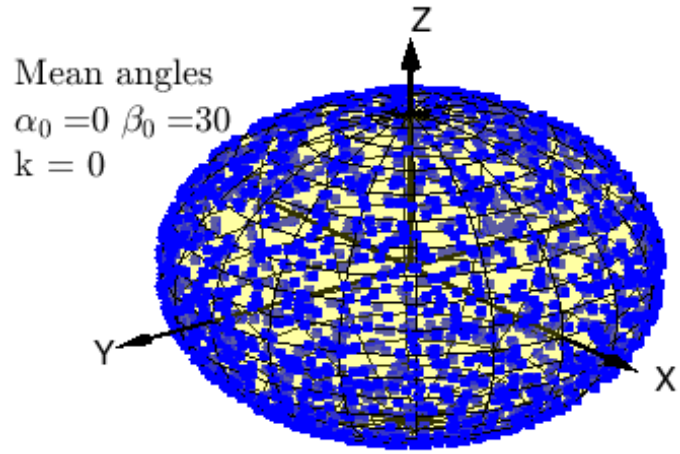
(a)
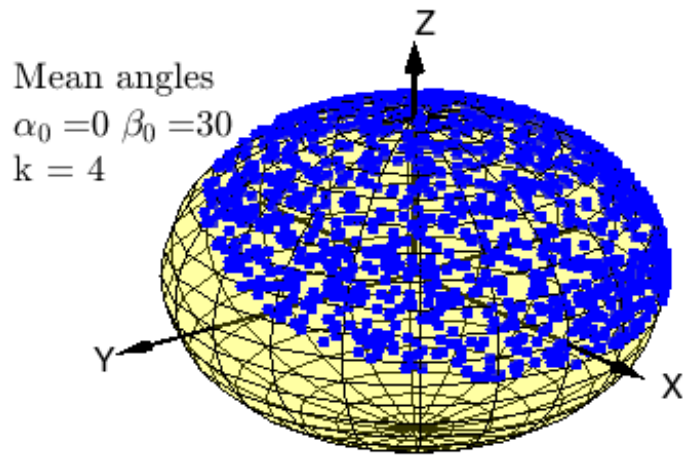
(b)
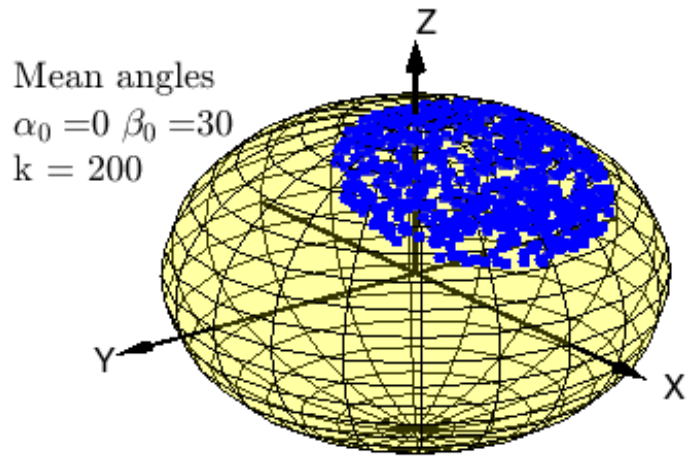
(c)

Figure 4.3: 3-D VMF distribution of scatterers on a unit hemisphere with mean angles ($\alpha_0 = 0°$, $\beta_0 = 30°$), and (a) $k = 0$, (b) $k = 4$, (c) $k = 200$.

4.2.2 Statistical Properties of the Non-isotropic 3-D Theoretical Model

In this section, the statistical properties of the 3-D non-isotropic spherical model are derived in terms of the amplitude and phase PDF, the ACF, the *Doppler* PSD, the envelope LCR, and the AFD.

4.2.2.1 Amplitude & Phase PDFs

The PDFs of the amplitude and phase of a *Rician* process are described for similar procedures in [68] and [71]. For the theoretical model, the amplitude PDF P_ξ of the envelope is described by (B.49) in Appendix B.2 and given as

$$P_\xi(z) = \frac{z}{\sigma_o^2} e^{-\frac{z^2 + K_0^2}{2\sigma_0^2}} I_0\left(\frac{zK_0}{\sigma_0^2}\right), z \geq 0 \tag{4.6}$$

where z is the amplitude variable, I_o is the zeroth order modified Bessel function of the first kind, $K_0 = \sqrt{\frac{K}{K+1}}$, where K is the *Rician* K-factor, and the variance of $\mu(t)$ is given by $\text{Var}\{\mu(t)\} = 2\sigma_0^2$.

The phase PDF P_ϑ of the envelope of a *Rician* process is given by [71]

$$\begin{aligned}
P_\vartheta(\theta) = &\frac{e^{-\frac{K_0^2}{2\sigma_0^2}}}{2\pi}\left\{1 + \frac{K_0}{\sigma_0}\sqrt{\frac{\pi}{2}}\cos\left(\theta - \theta_K\right)\right.\\
&\left. e^{\frac{K_0^2\cos^2(\theta - \theta_K)}{2\sigma_0^2}}\left[1 + erf\left(\frac{K_0\cos\left(\theta - \theta_K\right)}{\sigma_0\sqrt{2}}\right)\right]\right\}
\end{aligned} \tag{4.7}$$

where $erf(.)$ denotes the error function and $\theta_K = arg\{m(t)\}$.

4.2.2.2 Temporal ACF

As in the isotropic case described in section 3.2.2.2, the temporal ACF is the ensemble average $E[.]$ of the received band pass signal $\mu(t)$ with itself at a time separation τ, when $\mu(t)$ is WSS, expressed as [54]

$$r_{\mu\mu}(t, t + \tau) = E\left[\mu^*(t)\mu(t + \tau)\right] = r_{\mu\mu}(|\tau|). \tag{4.8}$$

If we substitute (4.1) into (4.8) we obtain the normalised ACF of the LoS and NLoS components as follows:

(a) In the case of the LoS component,

$$r_{\mu_m \mu_m}(\tau) = \frac{K}{(K+1)} e^{j2\pi f_{D\max}\tau \cos\alpha_0 \cos\beta_0}. \tag{4.9}$$

(b) In the case of the NLoS scattering component,

$$r_{\mu_n \mu_n}(\tau) = \frac{1}{(K+1)} \int_{-\pi}^{\pi} \int_{-\pi}^{\pi} e^{j2\pi f_{D\max}\tau \cos\alpha \cos\beta} f(\alpha,\beta) \, d\alpha \, d\beta \tag{4.10}$$

The normalised theoretical temporal ACF can then be expressed as the summation of (4.9) and (4.10),

$$r_{\mu\mu}(\tau) = r_{\mu_m \mu_m}(\tau) + r_{\mu_n \mu_n}(\tau). \tag{4.11}$$

4.2.2.3 Doppler PSD

The PSD $S_{\mu\mu}(f)$ is obtained by taking the Fourier transform of the ACF,

$$S_{\mu\mu}(f_D) = \int_{-\infty}^{\infty} r_{\mu\mu}(\tau) e^{-2\pi f_D \tau} \, d\tau. \tag{4.12}$$

Two important characteristics of the PSD are the *Doppler* shift $B_{\mu\mu}^{(1)}$ and the *Doppler* spread $B_{\mu\mu}^{(2)}$. The *Doppler* shift $B_{\mu\mu}^{(1)}$ is given by

$$B_{\mu\mu}^{(1)} = \frac{\int_{-\infty}^{\infty} f S_{\mu\mu}(f) \, df}{\int_{-\infty}^{\infty} S_{\mu\mu}(f) \, df} \tag{4.13}$$

The *Doppler* spread $B_{\mu\mu}^{(2)}$ is given by

$$B_{\mu\mu}^{(2)} = \sqrt{\frac{\int_{-\infty}^{\infty} \left(f - B_{\mu\mu}^{(1)}\right) S_{\mu\mu}(f) \, df}{\int_{-\infty}^{\infty} S_{\mu\mu}(f) \, df}}. \tag{4.14}$$

4.2.2.4 Envelope LCR & AFD

Assuming a 3-D non-isotropic scattering environment, the LCR $L(R)$ is defined as the rate at which the received signal envelope $\xi(t)$ crosses the level R in a positive (or negative) going direction and, where a LoS component is present, it can be shown

that [72]

$$L(R) = \frac{2R\sqrt{(K+1)}}{\pi^{\frac{3}{2}}} \sqrt{\frac{b_2}{b_0} - \frac{b_1^2}{b_0^2}}$$
$$\times e^{-K-(K+1)R^2}$$
$$\times \int_0^{\frac{\pi}{2}} \cosh\left(2\sqrt{K(K+1)} \cdot R\cos\theta\right)$$
$$\times \left[e^{-(\chi\sin\theta)^2} + \sqrt{\pi} \cdot \chi \cdot \sin\theta \cdot erf(\chi\sin\theta)\right] d\theta \tag{4.15}$$

where χ, b_0, b_1 and b_2 are

$$\chi = \sqrt{\frac{Kb_1^2}{(b_0 b_2 - b_1^2)}} \tag{4.16}$$

$$b_0 \triangleq E\left[\mu_I(t)^2\right] = E\left[\mu_Q(t)^2\right] \tag{4.17}$$

$$b_1 \triangleq E\left[\mu_I(t)^2 \dot{\mu}_Q(t)^2\right] = E\left[\mu_Q(t)^2 \dot{\mu}_I(t)^2\right] \tag{4.18}$$

$$b_2 \triangleq E\left[\dot{\mu}_I(t)^2\right] = E\left[\dot{\mu}_Q(t)^2\right] \tag{4.19}$$

respectively, and where $\mu_I(t)$ and $\mu_Q(t)$ are the in-phase and quadrature components of the complex fading envelope $\mu(t)$ described by (4.1). Correspondingly, $\dot{\mu}_I(t)$ and $\dot{\mu}_Q(t)$ are the first derivatives of $\mu_I(t)$ and $\mu_Q(t)$ respectively. Therefore, for b_0, b_1 and b_2 it can be shown that

$$b_n = \frac{1}{K+1}(2\pi)\int_{-\pi}^{\pi}\int_{-\pi}^{\pi} f(\alpha,\beta)\left[f_{D_{max}}\cos(\alpha)\cos(\beta)\right]^n d\alpha d\beta \tag{4.20}$$

and that

$$b_0 = \frac{1}{K+1}. \tag{4.21}$$

The AFD $T(R)$ is defined as the average time over which the received signal envelope $\xi(t)$ remains below a certain level R. For conditions when a LoS component is present this can be written as [54]

$$T(R) = \frac{1 - Q\left(\sqrt{2K}, \sqrt{2(K+1)R^2}\right)}{L(R)} \tag{4.22}$$

where $Q(a,b)$ is the Marcum Q function [73].

4.3   Simulation Model

From the theoretical model described in section 4.2.2, a corresponding simulation model can be developed based on a SoS approach. From (4.1), (4.2), and (4.3), the simulation model becomes

$$\hat{\mu}(t) = \hat{m}(t) + \hat{n}(t) \tag{4.23}$$

where

$$\hat{m}(t) = m(t) = \sqrt{\frac{K}{(K+1)}} e^{j(2\pi f_{D\max} t \cos \alpha_0 \cos \beta_0)} \tag{4.24}$$

and

$$\hat{n}(t) = \sqrt{\frac{1}{(K+1)}} \sum_{n=1}^{N} \frac{1}{\sqrt{N}} e^{j(2\pi f_{D\max} t \cos \alpha_n \cos \beta_n + \theta_n)}. \tag{4.25}$$

In (4.24), the LoS component in the simulation model is identical to the LoS component in the theoretical model defined in (4.2). In (4.25), N becomes a finite number of effective scatterers and the only parameters which remain to be determined are the angles (α_0, β_0) and (α_n, β_n); the AAoA and EAoA of the mean and effective scatterers respectively.

4.3.1   MEV for Parametrisation of the Proposed SoS Simulation Model

Using an approach consistent with [68], the MEV is used to jointly calculate the set of azimuth and elevations angles. An extension to the modified method of equal area (MMEA) [53] used in the case of 2D non-isotropic scattering, the MEV considers the volume of the VMF PDF given by the cumulative distribution function (CDF),

$$F(\alpha, \beta) = \int_{-\pi}^{\pi} \int_{-\pi}^{\pi} f(\alpha, \beta) \, d\alpha \, d\beta. \tag{4.26}$$

In this study, the MEV was used to select a set of AAoA and EAoA angles $[\alpha_n, \beta_n]_{n=1}^{N}$ to satisfy the condition

$$\int_{(\beta_n - \frac{\pi}{2})}^{\beta_n} \int_{(\alpha_n - \pi)}^{\alpha_n} f(\alpha_n, \beta_n) \, d\alpha \, d\beta = \frac{n - \frac{1}{4}}{N}, n = 1, 2, ..., N. \tag{4.27}$$

4.3.2 Statistical Properties of the Simulation Model

Using the theoretical model and its corresponding statistical properties, it is possible to derive the properties of the simulation model. This is achieved by applying the discrete model parameters to (4.6), (4.7), (4.11), (4.12), (4.13), (4.14), (4.15) and (4.22) as demonstrated in the sub-sections that follow.

4.3.2.1 Amplitude & Phase PDFs

As defined in (B.47) in Appendix B.2, the amplitude PDF of the SoS simulation model becomes

$$P_{\hat{\xi}}(z) = (2\pi)^2 z \int_0^\infty \left[\prod_{n=1}^N J_0\left(2\pi |g| x\right) \right] J_0\left(2\pi z x\right) J_0\left(2\pi K_0 x\right) x\, dx \qquad (4.28)$$

where g is the single bounce gain of the finite scatterers given by $g = \sigma_0 \sqrt{2/N}$.

Similarly, the phase PDF of the SoS simulation model becomes

$$\begin{aligned} P_{\hat{\vartheta}}(\theta) = & 2\pi \int_0^\infty \int_0^\infty \left[\prod_{n=1}^N J_0\left(2\pi |g| x\right) \right] \\ & J_0\left(2\pi x \sqrt{z^2 + K_0^2 - 2z K_0 \cos\left(\theta - \theta_K\right)}\right) x z\, dx\, dz. \end{aligned} \qquad (4.29)$$

4.3.2.2 Temporal ACF

The ACF of the simulation is given by

$$\hat{r}_{\hat{\mu}\hat{\mu}}(t, t + \tau) = E\left[\hat{\mu}^*(t)\hat{\mu}(t + \tau)\right] = \hat{r}_{\hat{\mu}_m\hat{\mu}_m}(\tau) + \hat{r}_{\hat{\mu}_n\hat{\mu}_n}(\tau) \qquad (4.30)$$

where $\hat{r}_{\hat{\mu}_m\hat{\mu}_m}(\tau)$ and $\hat{r}_{\hat{\mu}_n\hat{\mu}_n}(\tau)$ are the LoS and NLoS components respectively.

(a) In the case of the normalised LoS component,

$$\hat{r}_{\hat{\mu}_m\hat{\mu}_m}(\tau) = \frac{K}{(K+1)} e^{j2\pi f_{D_{\max}} \tau \cos\alpha_0 \cos\beta_0} \qquad (4.31)$$

and will thus be identical to the theoretical model.

(b) In the case of the normalised NLoS scattering component,

$$\hat{r}_{\hat{\mu}_n \hat{\mu}_n}(\tau) = \frac{1}{(K+1)} \sum_{n=1}^{N} \frac{1}{N} e^{j2\pi f_{D_{\max}} \tau \cos \alpha_n \cos \beta_n}. \tag{4.32}$$

4.3.2.3 Doppler PSD

The *Doppler* PSD of the simulation model is simply the Fourier transform of $\hat{r}_{\hat{\mu}\hat{\mu}}(\tau)$ and may be expressed as

$$\hat{S}_{\hat{\mu}\hat{\mu}}(f_D) = F\left\{\hat{r}_{\hat{\mu}\hat{\mu}}(\tau)\right\} = F\left\{\hat{r}_{\hat{\mu}_m \hat{\mu}_m}(\tau)\right\} + F\left\{\hat{r}_{\hat{\mu}_n \hat{\mu}_n}(\tau)\right\}. \tag{4.33}$$

The *Doppler* shift $\hat{B}_{\hat{\mu}\hat{\mu}}^{(1)}$ and the *Doppler* spread $\hat{B}_{\hat{\mu}\hat{\mu}}^{(2)}$ of the simulation model can be derived from the discrete PSD and ACF as shown in Appendix E (E.6) and (E.7), expressed as

$$\hat{B}_{\hat{\mu}\hat{\mu}}^{(1)} = \frac{f_{D_{\max}}}{(K+1)} \times \left[K \cos \alpha_0 \cos \beta_0 + \sum_{n=1}^{N} \cos \alpha_n \cos \beta_n\right] \tag{4.34}$$

and

$$\hat{B}_{\hat{\mu}\hat{\mu}}^{(2)} = \sqrt{-\ddot{\hat{r}}_{\hat{\mu}\hat{\mu}}(0) - \left(\hat{B}_{\hat{\mu}\hat{\mu}}^{(1)}\right)^2}. \tag{4.35}$$

4.3.2.4 Envelope LCR & AFD

The envelope LCR of the simulation model can be derived as [68]

$$
\begin{aligned}
\hat{L}(R) ={} & \frac{2R\sqrt{(K+1)}}{\pi^{\frac{3}{2}}} \sqrt{\frac{\hat{b}_2}{\hat{b}_0} - \frac{\hat{b}_1^2}{\hat{b}_0^2}} \\
& \times e^{-K-(K+1)R^2} \\
& \times \int_0^{\frac{\pi}{2}} \cosh\left(2\sqrt{K(K+1)} \cdot R\cos\theta\right) \\
& \times \left[e^{-(\hat{\chi}\sin\theta)^2} + \sqrt{\pi} \cdot \hat{\chi} \cdot \sin\theta \cdot erf\left(\hat{\chi}\sin\theta\right)\right] d\theta
\end{aligned} \tag{4.36}
$$

where $\hat{\chi}$, $\hat{b}_0$ and $\hat{b}_m$ are

$$\hat{\chi} = \sqrt{\frac{K\hat{b}_1^2}{\left(\hat{b}_0\hat{b}_2 - \hat{b}_1^2\right)}} \tag{4.37}$$

$$\hat{b}_0 = \frac{1}{K+1} \tag{4.38}$$

$$\text{and } \hat{b}_m = \frac{1}{K+1}(2\pi)\frac{1}{N}\sum_{n=1}^{N}\left[f_{D_{max}}\cos\alpha_n\cos\beta_n\right]^m \tag{4.39}$$

respectively, where $m \in \{1, 2\}$. Similarly, the envelope AFD for the simulation model can be expressed as

$$\hat{T}(R) = \frac{1 - Q\left(\sqrt{2K}, \sqrt{2(K+1)R^2}\right)}{\hat{L}(R)}. \tag{4.40}$$

4.4 Numerical Results & Analysis

In this section we analyse and compare the theoretical, simulation and numerical results. The model parameters used in this analysis are informed by optimised values derived during the verification process presented in Chapter 6 and summarised in Table 4.2.

Table 4.2: Parameters used in 3-D spherical non-isotropic model analysis.

Parameter	Value	Definition
f_c	2 MHz	insonation frequency of TCD ultrasound
c	1500 ms^{-1}	estimated speed of sound in tissue
$f_{D_{max}}$	1.09 kHz	maximum *Doppler* frequency
K	0.0078	*Rician* K-factor
k	4.2	VMF concentration parameter
σ	0.48	standard deviation of the PDF
N	15	number of incident scatterers
v	0.42 ms^{-1}	blood flow velocity within the isonated vessel
α_0	0°	mean azimuth angle of arrival
β_0	0°	mean elevation angle of arrival
θ_K	0 rad	$arg\{m(t)\}$

Fig. 4.4 and Fig. 4.5 show plots for the amplitude and phase PDFs of the theoretical reference model, simulation model and SoS simulation, where $K = 0.0078$, $\sigma = 0.48$, $\theta_K = 0$, and $N = 15$. For the phase PDFs, Fig. 4.5(a) demonstrates the phase distribution of a *Rician* process. Compare this with the uniform distribution of a *Rayleigh* process shown in Fig. 3.7. The contiguity of these plots demonstrates that the SoS channel simulator provides a very strong agreement with the theoretical reference and simulation models. Furthermore, the plots confirm the process corresponding to the parameters in Table 4.2 is weakly *Rician*.
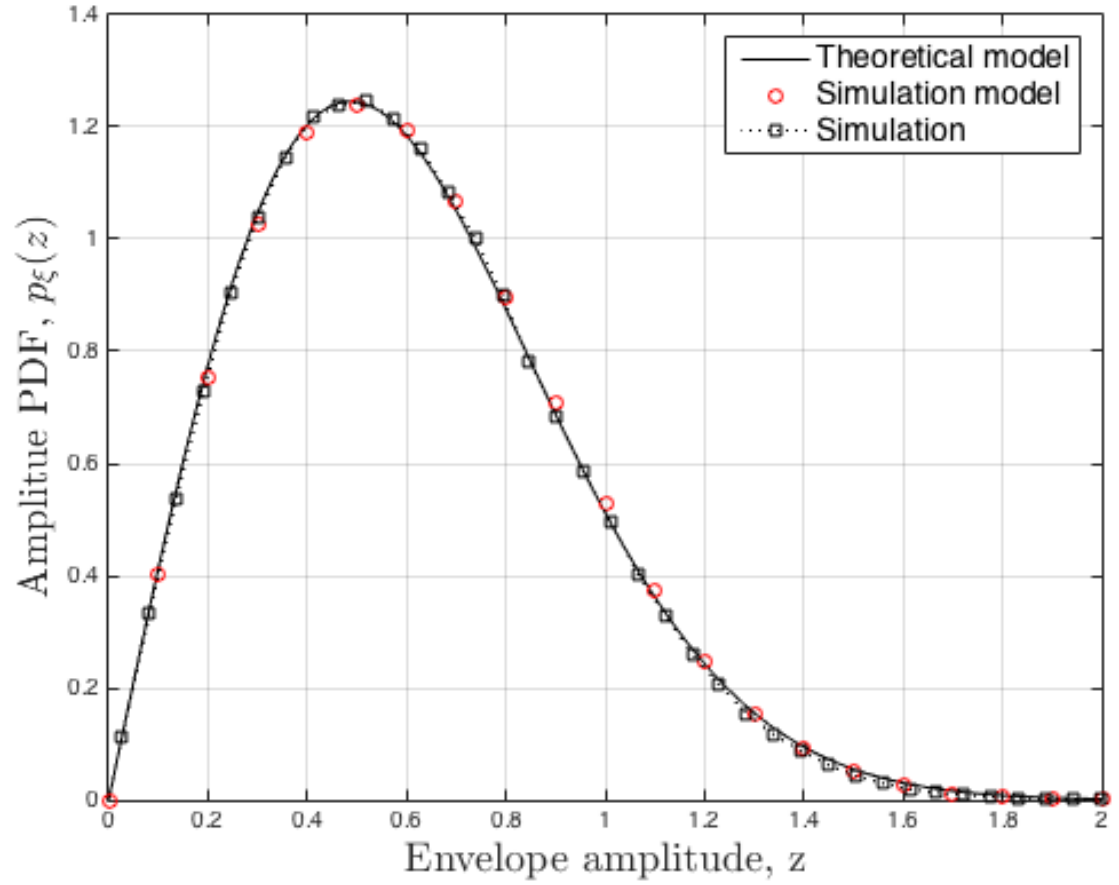
Figure 4.4: The amplitude PDF of the 3-D non-isotropic spheroid theoretical reference, simulation, and SoS simulation results, where $K = 0.0078$, $\sigma = 0.48$, and $N = 15$.
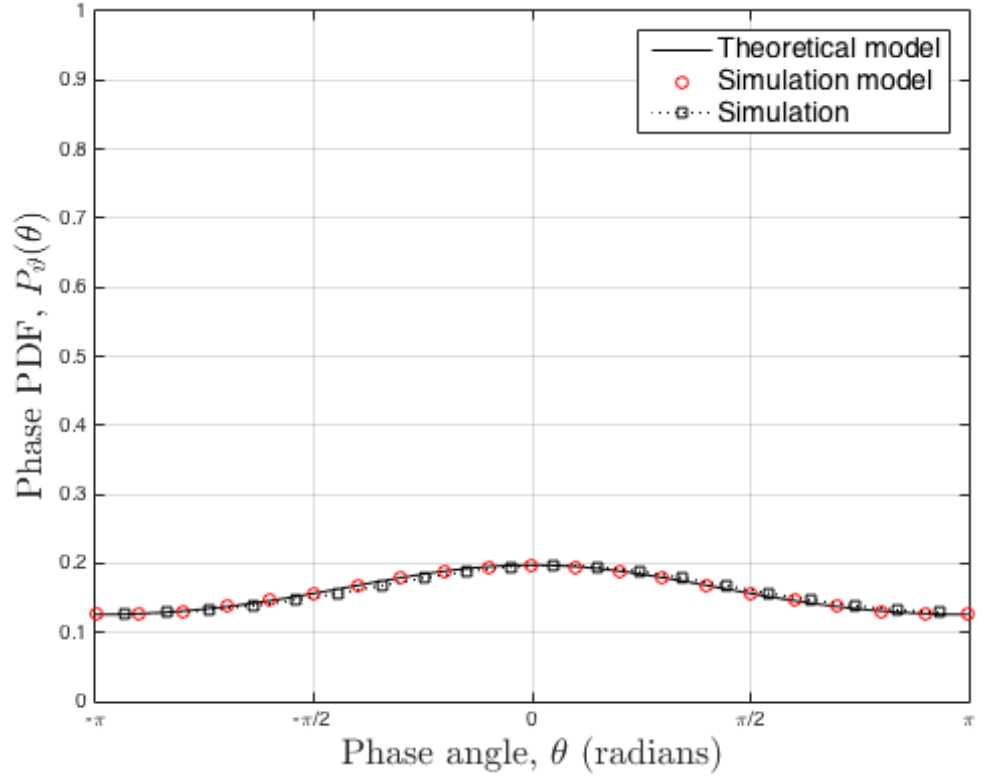
(a)
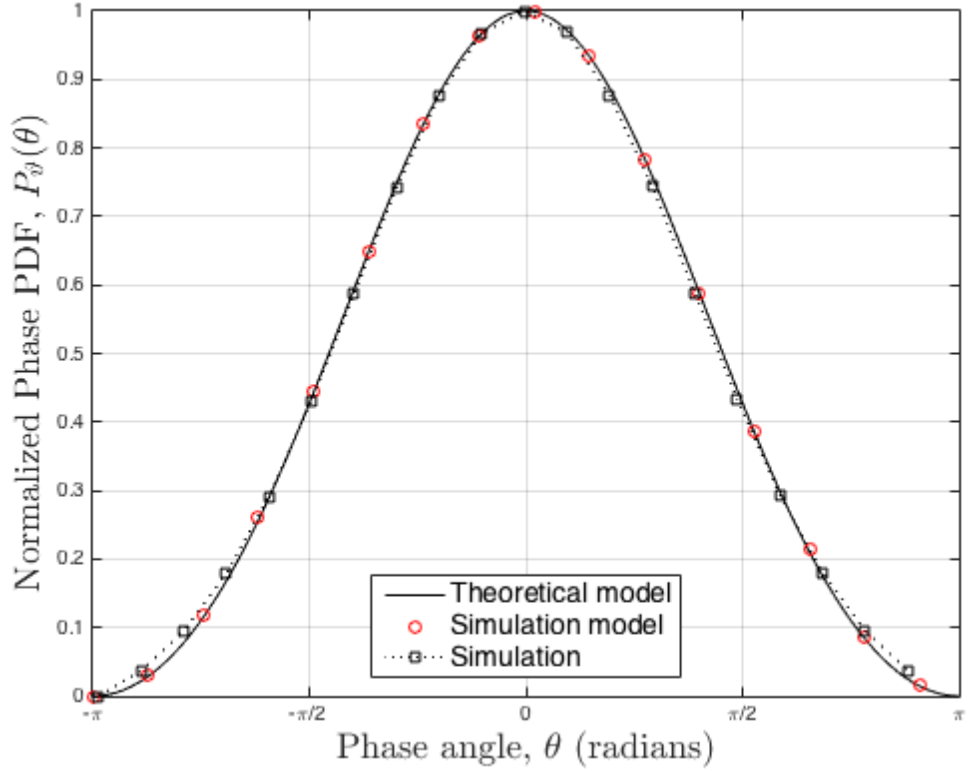
(b)

Figure 4.5: (a) The phase PDF (b) The normalised phase PDF; of the 3-D non-isotropic spheroid theoretical reference, simulation, and SoS simulation results, where $K = 0.0078$, $\sigma_0 = 0.48$, $\theta_K = 0$, and $N = 15$.

The level of agreement of the ACFs must be considered in terms of the accuracy of estimation of the α_n and β_n parameters in the NLoS components, as calculated using the MEV. Fig. 4.6 shows the ACFs of the theoretical reference model, simulation model and SoS simulation, where $f_{D_{max}} = 1.09$ kHz, $K = 0.0078$, $k = 4.2$, $N = 15$, $\alpha_0 = 0°$ and $\beta_0 = 0°$. This plot shows strong agreement up to a temporal separation period of approximately 4.2 ms, after which the simulation results begin to diverge from the theoretical model. This period of agreement is a significant improvement on that achieved for the 3-D isotropic case presented in section 3.4 Fig. 3.9, and has been achieved with half the number of simulated incident scatterers, N. As in the case of Fig. 3.9, as $(N \rightarrow \infty)$, so the simulation model and SoS simulation converge with the theoretical model such that $\hat{r}_{\hat{\mu}_i \hat{\mu}_i}(\tau) \rightarrow r_{\mu_i \mu_i}(\tau)$.
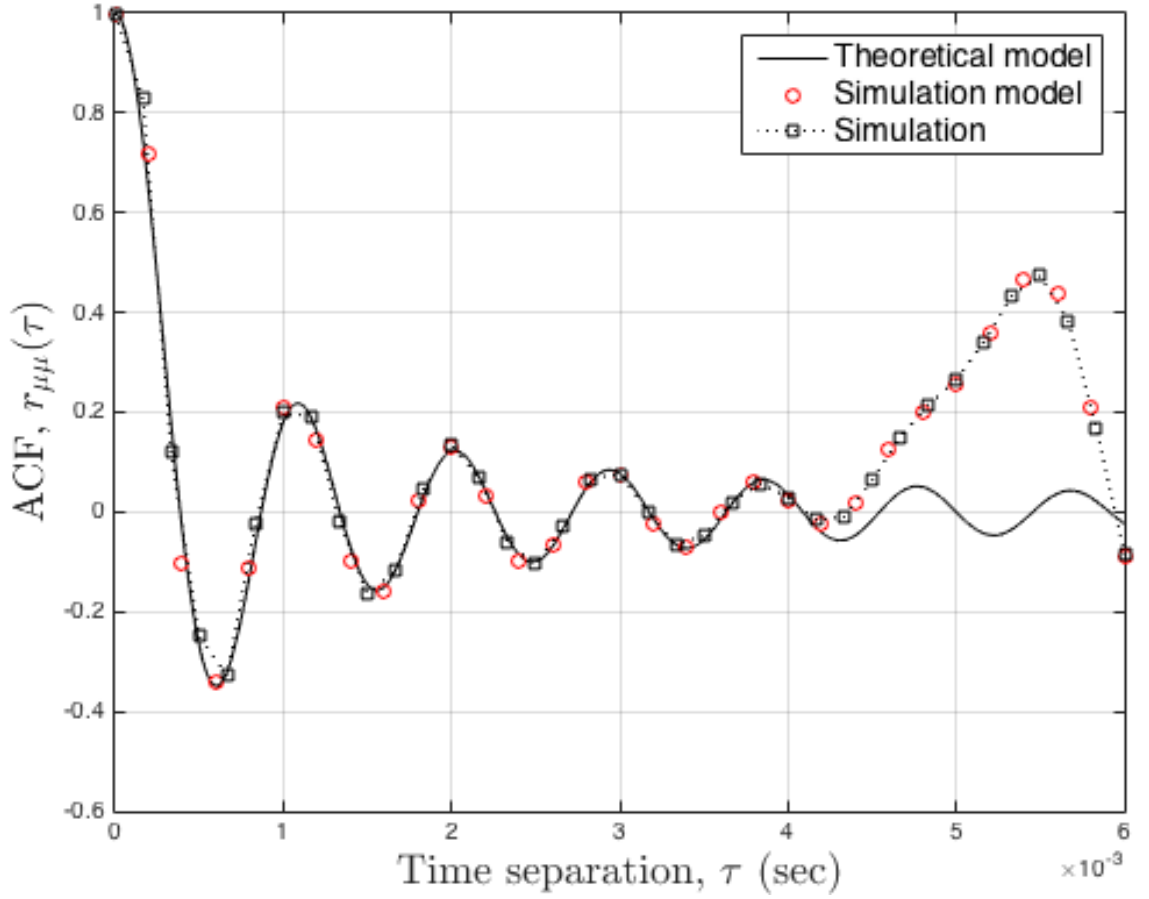
Figure 4.6: The normalised ACF of the 3-D non-isotropic spheroid theoretical reference, simulation, and SoS simulation results, where $f_{D_{max}} = 1.09$ kHz, $K = 0.0078$, $k = 4.2$, $N = 15$, $\alpha_0 = 0°$ and $\beta_0 = 0°$.

The plots of the normalised envelope LCRs and AFDs of the theoretical reference model, simulation model and SoS simulation are shown in Fig. 4.7 and Fig. 4.8 respectively, where $f_c = 2$ MHz, $f_{D_{max}} = 1.09$ kHz, $K = 0.0078$, $k = 4.2$, $N = 15$, $\alpha_0 = 0°$ and $\beta_0 = 0°$. These plots show close agreement, demonstrating the accuracy of the simulation model and SoS simulation.
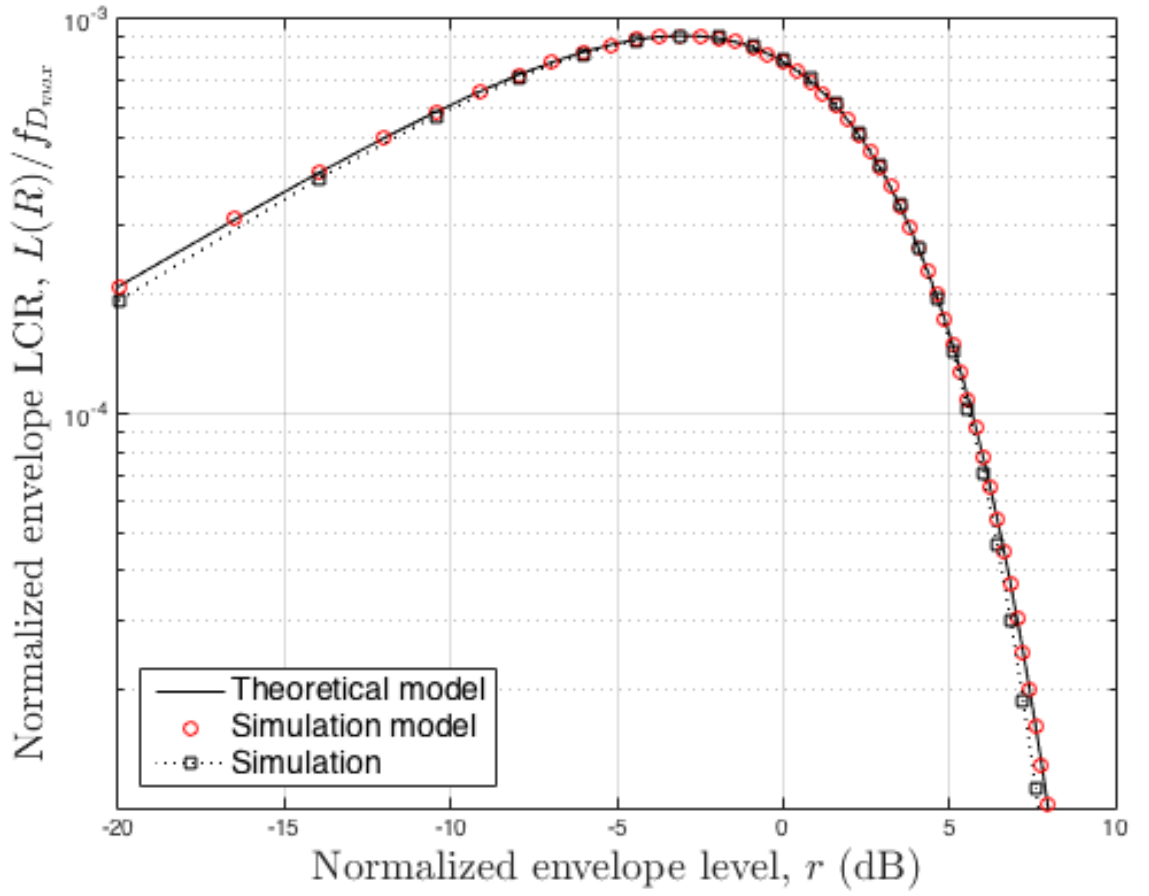
Figure 4.7: The normalised LCR (dB) of the 3-D non-isotropic spheroid theoretical reference, simulation, and SoS simulation results, where $f_c = 2$ MHz, $f_{D_{max}} = 1.09$ kHz, $K = 0.0078$, $k = 4.2$, $N = 15$, $\alpha_0 = 0°$ and $\beta_0 = 0°$.
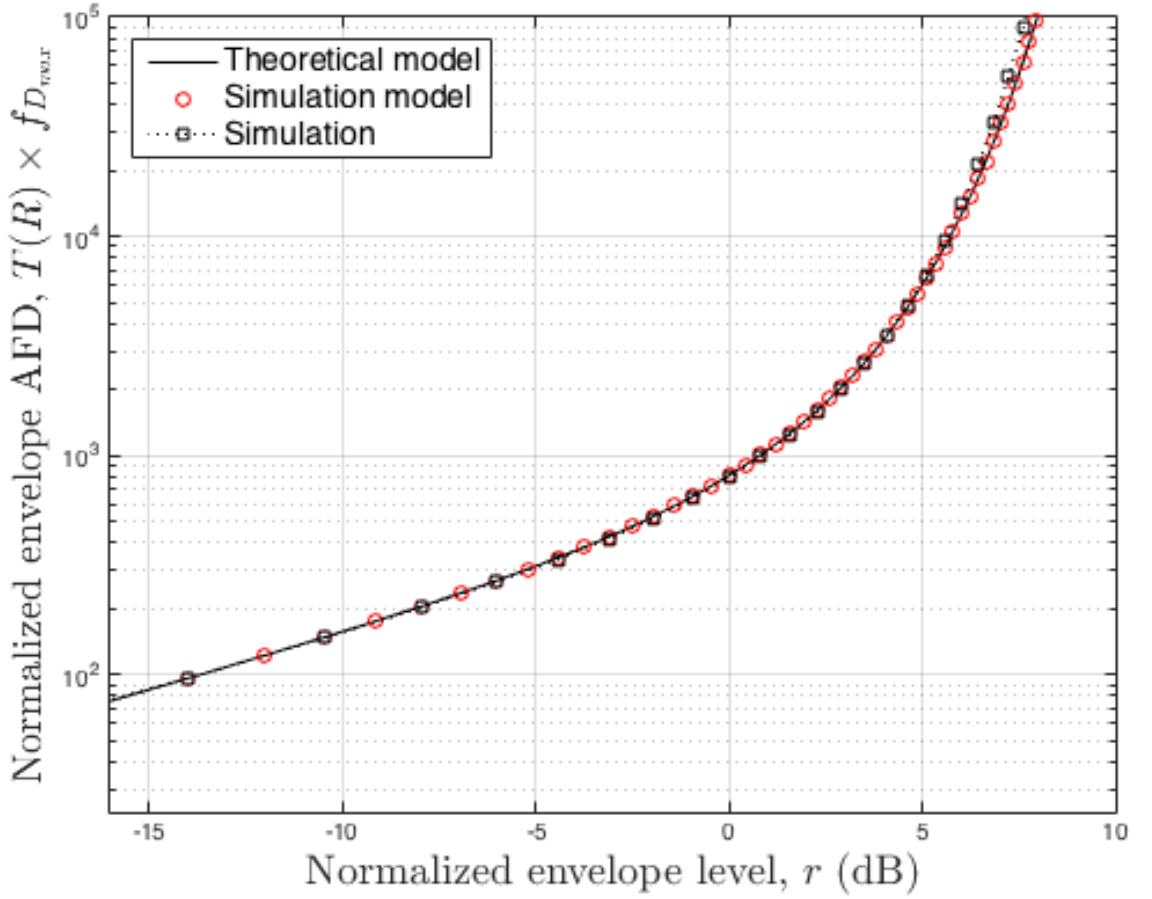
Figure 4.8: The normalised AFD (dB) of the 3-D non-isotropic spheroid theoretical reference, simulation, and SoS simulation results, where $f_c = 2$ MHz, $f_{D_{max}} = 1.09$ kHz, $K = 0.0078$, $k = 4.2$, $N = 15$, $\alpha_0 = 0°$ and $\beta_0 = 0°$.

The results presented using the non-isotropic theoretical reference model, simulation model and SoS channel simulator continue to demonstrate a high degree of accuracy, whilst overcoming the fundamental disadvantages of the 3-D isotropic TCD ultrasound propagation channel models discussed in Chapter 3. The performance of the 3-D non-isotropic models is somewhat better than the isotropic models, demonstrated by the lower number of incident scatterers used in the SoS channel simulator, where $N = 15$, and the reduced complexity achieved by overcoming the requirement to estimate the spatial CCF and by combining the PDF analysis in azimuth and elevation using the VMF distribution. Furthermore, these 3-D non-isotropic models can be adapted to include a LoS scattering component, thus providing better opti-

misation capabilities and a more flexible approach that can be adapted to measured results.

4.5   Summary

In this chapter, 3-D non-isotropic spherical models have been proposed for investigation of the characteristics of a TCD ultrasound propagation channel. The stochastic characteristics of the models have been investigated and closed form expressions have been derived for the amplitude and phase PDFs, ACFs, LCRs and AFDs. The MEV was used to optimise the α_n and β_n parameters, and the simulation models achieve a good fit with the theoretical mathematical reference model. These models demonstrate greater accuracy and performance than the isotropic models discussed previously in Chapter 3, and support the analysis of a *Rician* process through the presence of a NLoS component. In Chapter 6 the performance of these models will be verified against measured results from a TCD *Doppler* phantom, described in Chapter 5, and a patient measurements database.

Chapter 5

A Flow Phantom for TCD Ultrasound Studies

5.1 Introduction

Medical phantoms are objects with particular dimensions and characteristics that are specially designed to replicate human physiology for specific imaging modalities, e.g. magnetic resonance imaging (MRI), positron emission tomography–computed tomography (PET-CT), and ultrasound. They support activities such as quality control assessment, performance evaluation, and research analysis. In clinical research, data security and patient ethics governance rules place restrictions on experimental work with patients and patient data. Medical phantoms provide a method for pre-clinical research which avoids these restrictions.

In this chapter, a blood flow phantom is described which will support pre-clinical research of TCD propagation channels. Blood flow phantoms, a particular class of medical phantom that can produce constant and pulsatile blood flow with physiological tissue and blood equivalence, are important tools for designing, developing, and evaluating *Doppler* ultrasound systems. This chapter describes the process of developing and characterising a blood flow phantom test bench for experimental study of TCD ultrasound channel characteristics and fulfils an important step in the process of analysing the TCD propagation channel.

5.2 Tissue Mimicking Materials

There are a number of commercial ultrasound flow phantoms available for purchase on the market. These are commonly based on tissue mimicking material (TMM) such as low density reticulated foam, gelatin and agar; the acoustic and mechanical properties of which are mostly well known between 2-10 MHz [74]. However, poly (vinyl alcohol) cryogel (PVA-C) offers a number of advantages over traditional TMMs; it's non-toxic, maintains long-term structural and acoustic stability and can form vascular models without the use of additional vessel wall tubing, such as silicon, rubber, latex etc. This last point is important, since unwanted artefacts in the received signal can be introduced by the poor acoustic properties of vessel mimicking materials. For these reasons, PVA-C TMMs have emerged from initial use in magnetic resonance imaging (MRI) and are now widely employed in brain, vessel and breast ultrasound phantoms [75].

In this chapter, a PVA-C TMM is described which has been specially designed for analysis and verification of a TCD US propagation channel model. In order to improve the attenuation and backscattering properties of PVA-C, a number of common scattering agents were tested; namely silicon carbide[i], graphite[ii], and aluminium oxide[iii] particles. The acoustic velocity, attenuation, characteristic impedance, and backscatter coefficient of the TMMs were assessed. The results of this evaluation are reported and a wall-less PVA-C flow phantom design is described.

5.3 Evaluation of PVA-C TMM Compounds

In order to establish the most suitable compound material for the phantom, an experiment was designed to test the acoustic properties of each candidate TMM sample at a centre frequency of 2.08 MHz against the standards recommended by

---

[i]Silicon carbide powder (Grit 400, 20μ particle size), supplied by Logitech Ltd, Erskine Ferry Road, Old Kilpatrick, Glasgow G60 5EU.

[ii]Graphite powder (Mesh size 340<, 44μ particle size), supplied by Easy Composites Ltd, Unit 39, Park Hall Business Village, Longton, Stoke on Trent, Staffordshire ST3 5XA.

[iii]Aluminium oxide powder (3μ particle size), supplied by Logitech Ltd, Erskine Ferry Road, Old Kilpatrick, Glasgow G60 5EU.

IEC 61685 [76]: TMMs should have an acoustic velocity of $1540(\pm(15))ms^{-1}$, an attenuation coefficient of $(0.5 \pm 0.05) \times 10^{-4} f dBm^{-1}Hz^{-1}$, a characteristic acoustic impedance of $(1.6 \pm 0.16) \times 10^6 kgm^{-2}s^{-1}$, and a backscatter coefficient of $(1 - 4) \times 10^{-28} f^4 m^{-1} Hz^{-4} sr^{-1}$.

5.3.1 Preparation of PVA-C TMMs

PVA is a water-soluble synthetic polymer. An aqueous solution of PVA was prepared by mixing 10% by weight of PVA powder[iv] with sterile distilled water at room temperature. To this solution, 0.01% benzalkonium chloride[v] was added to prevent microbial invasion. The solution was gently heated and mixed until it became a thick, clear liquid, as shown in Fig. 5.1. When heating the solution, care must be taken to prevent the temperature rising above 98 °C in order to prevent aeration and evaporation due to boiling. The solution is then allowed to cool to room temperature. Once cooled, it is mixed with the desired scattering agent (1% by weight of the aluminium, graphite and silicon carbide powders) and then degassed in a vacuum chamber.

The final stage of PVA-C TMM preparation is freeze-thawing the solution to create a solid cryogel phantom. This was performed in a programmable thermo-cycler[vi] that was configured to automatically perform 4, 6 and 8 cycles of 12 hours freezing to −20 °C and 12 hours thawing to +20 °C. In total, 12 candidate TMMs were prepared; for each of the (4, 6 and 8) cycles, test samples were produced for control (no scattering agent), aluminium, graphite and silicon carbide. Examples of the TMM test samples are shown in Fig. 5.2.

[iv]Poly (vinyl alcohol) 99+% hydrolysed, product 341584, Sigma-Aldrich UK company Ltd. Dorset, England.

[v]Benzalkonium chloride solution, product 63249, Sigma-Aldrich UK company Ltd. Dorset, England.

[vi]Automated thermo-cycler, developed by the Department of Clinical Physics & Bioengineering, NHS Greater Glasgow and Clyde.

Figure 5.1: An aqueous solution of 10% by weight PVA in water.

Figure 5.2: PVA-C TMM after 4 freeze-thaw cycles samples for control, silicon carbide (SiC), graphite and aluminium oxide (AlO).

5.3.2 Measurement of Acoustic Parameters

The measurement methods followed were based on the techniques described by *Browne et al* [77]. The acoustic velocity, attenuation coefficient, and backscatter coefficient were measured using the ultrasonic test system shown in Fig. 5.3. The

test system consisted of an Olympus NDT immersion transducer (A306S-SU) with a centre frequency of 2.08 MHz, mounted upon a XYZ motion stage, an immersion water tank filled with de-gassed water, a programmable pulser-receiver (Utex UT340), a digital storage oscilloscope (Tektronix TPS2024B), and a personal computer (PC). The PC was used with supporting software scripts developed in Matlab$^{\text{TM}}$for control of the motion stage and analysis of the pulse-echo observations.
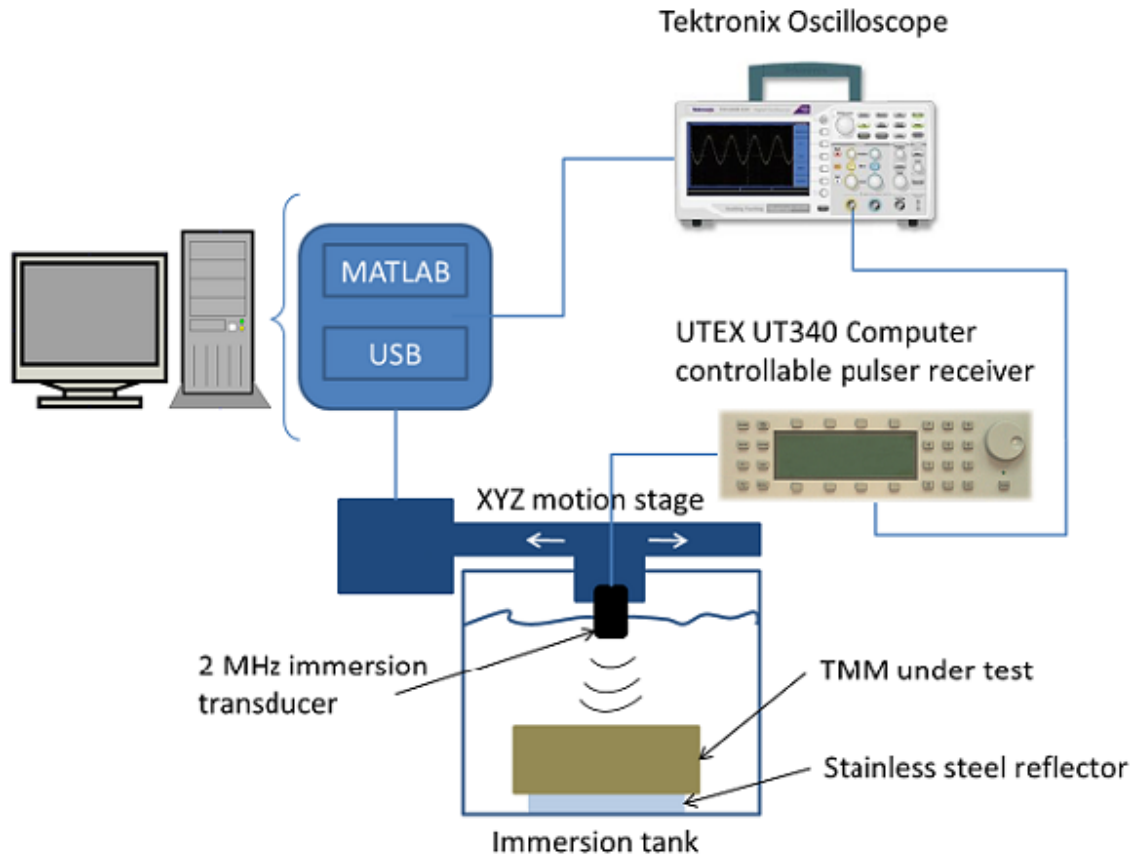
Figure 5.3: Ultrasonic pulse-echo test system.

The Olympus NDT immersion transducer (A306S-SU) characteristics are summarised for reference in Table 5.1.

Table 5.1: Olympus NDT immersion transducer (A306S-SU) characteristics.

Olympus unfocused immersion transducer	A306S
Frequency	2.25 MHz
Centre frequency	2.08 MHz
Minimum focal length	20.3 mm
Maximum focal length	48.3 mm
Crystal diameter	13 mm
6 dB bandwidth	51.82 %

The pulse-echo technique uses a single transducer operating sequentially in transmit and receive modes. The pulser-receiver was configured to drive the transducer at 100 V with a pulse repetition frequency of 200 Hz. The induced pulse was reflected from a highly polished stainless steel reflector in the base of the immersion tank. The motion stage was programmed to position the transducer over an area of 8 mm by 8 mm at intervals of 1 mm, allowing measurements to be spatially averaged. At each position of the transducer, the reflected RF signal was sampled at 25 MHz using the digital storage oscilloscope and post-processed on a PC using Matlab^TM scripts developed for this purpose. All measurements were conducted with a water temperature of $20\,°\mathrm{C} \pm 1\,°\mathrm{C}$.

5.3.2.1 Calculating the acoustic velocity

The acoustic velocity in the TMM sample was determined by measuring the time difference between the RF pulse and its echo from the stainless steel reflector with and without the TMM sample in place. This was calculated using the expression

$$c_s = \frac{c_w}{1 + \Delta t \frac{c_w}{d}} \tag{5.1}$$

where c_s was the acoustic velocity in the sample, c_w was the reference speed of sound in degassed water with no sample in place, d was the depth of the TMM sample (measured using digital callipers) and Δt was the time shift of the RF pulse and echo with the sample in place. The reference speed of sound, c_w, is given by

$$c_w = \frac{2d}{\Delta t}. \tag{5.2}$$

The calculated value of c_w was found to be within 0.25% of the expected value at $T\,°C$ using the formula for the speed of sound in pure water as a function of temperature derived by *Bilaniuk et al* [78], verifying the experimental setup.

5.3.2.2 Calculating the acoustic attenuation coefficient

The acoustic attenuation coefficient (α_c) of the sample was calculated as the log difference of the magnitudes of the gated RF echo using

$$\alpha_c = \frac{-20}{d} log_{10} \frac{|V_s|}{|V_w|} \tag{5.3}$$

where $|V_s|$ was the magnitude of the gated RF echo with the sample in place and $|V_w|$ was the magnitude of the gated RF echo through degassed water. The magnitudes were calculated using a 256-point discrete *Fourier* transform.

5.3.2.3 Calculating the acoustic backscatter coefficient

The acoustic backscatter coefficient (η) of the sample was calculated as the difference of the power spectra of the gated RF echo using the formulation derived by *Chen et al*[79] for flat transducers, given as

$$\eta \cong \begin{cases} \frac{\langle |V_s|^2 \rangle}{|V_w|^2} \cdot \frac{ka^2}{l.4\pi \exp\left[\left(\frac{2}{\pi}\right)\left(\frac{\bar{r}}{r_0}\right)^{\frac{1}{2}}\right]}, & \frac{\bar{r}}{r_0} < 1, \\ \frac{\langle |V_s|^2 \rangle}{|V_w|^2} \cdot \frac{ka^2}{l.4\pi.4E_\infty}, & \frac{\bar{r}}{r_0} > 1 \end{cases} \tag{5.4}$$

where $\langle |V_s|^2 \rangle$ was the mean power of the gated RF echo with the sample in place, $|V_w|^2$ was the power of the gated RF echo through degassed water, k is the wave number, a is the radius of the transducers active element, $\bar{r}$ is the mean distance

from the transducer surface to the sample volume, l is the length of the windowed backscatter signal, and r_0 is the *Rayleigh* distance of the transducer given by

$$r_0 = \frac{ka^2}{2\pi}.$$

(5.5)

5.3.2.4   Calculating the acoustic impedance

The acoustic impedance (z_a) was calculated using the formula

$$z_a = \rho \times c_s$$

(5.6)

where ρ was the measured density of the sample in kg/m^3, and c_s was the acoustic velocity calculated for each sample using the method described in section 5.3.2.1.

5.3.3   TMM Sample Test Results

A summary of the observed acoustic properties of the TMM samples are shown in Table 5.2 and the effects of varying the number of freeze-thaw cycles on the acoustic velocity, attenuation coefficient and the backscatter coefficient are shown in Fig. 5.4, Fig. 5.5, and Fig. 5.6, respectively.

Table 5.2: Measured tissue mimicking material parameters; control, silicon carbide, graphite and aluminium oxide

Scattering Agent	No. freeze-thaw cycles	Acoustic Velocity (v) ms^{-1}	Attenuation coeff. (α) $(\times 10^{-4})fdBm^{-1}$	Acoustic Impedance (Z) $(\times 10^{6})kgm^{-2}s^{-1}$	Backscatter coeff. (η) $(\times 10^{-28})f^{4}m^{-1}Hz^{-4}sr^{-1}$
IEC 61685 TMM parameters [76]	—	1540 ± 15	(0.5 ± 0.05)	(1.6 ± 0.16)	1
Control (none)	4 cycles	1527	0.25	1.72	1.79
	6 cycles	1534	0.33	1.75	1.53
	8 cycles	1536	0.48	1.79	1.14
Silicon Carbide	4 cycles	1528	0.72	1.71	0.69
	6 cycles	1529	1.29	1.73	0.26
	8 cycles	1534	0.56	1.75	0.98
Graphite	4 cycles	1528	0.31	1.70	1.66
	6 cycles	1529	0.40	1.74	1.35
	8 cycles	1524	1.01	1.77	0.44
Aluminium Oxide	4 cycles	1525	0.49	1.72	1.12
	6 cycles	1524	0.35	1.73	1.55
	8 cycles	1530	1.30	1.76	0.20

The error bars shown in Fig. 5.4, Fig. 5.5, and Fig. 5.6, are calculated using the standard error (SE), such that

$$SE = \frac{\sigma}{\sqrt{n}}. \tag{5.7}$$

The acoustic velocity results for 4, 6, and 8 cycle test samples are shown in Fig. 5.4. The acoustic velocity measured in the 4 cycle control sample is generally slightly lower than previously reported [75], while the 8-cycle graphite sample seems to lie outside the general trend. However the remaining results are reasonably consistent, showing that increasing the number of freeze-thaw cycles results in an increase in acoustic velocity through the sample and the mean acoustic velocities measured are mostly around or within IEC limits; $1540(\pm(15))ms^{-1}$. In particular, the 4 and 6-cycle aluminium oxide samples are observed to fall just outside the lower IEC limit. However, with a mean measure of $1525ms^{-1}$, the 4-cycle sample is thought to be within acceptable measurement tolerances given that all observed velocities were lower than anticipated.
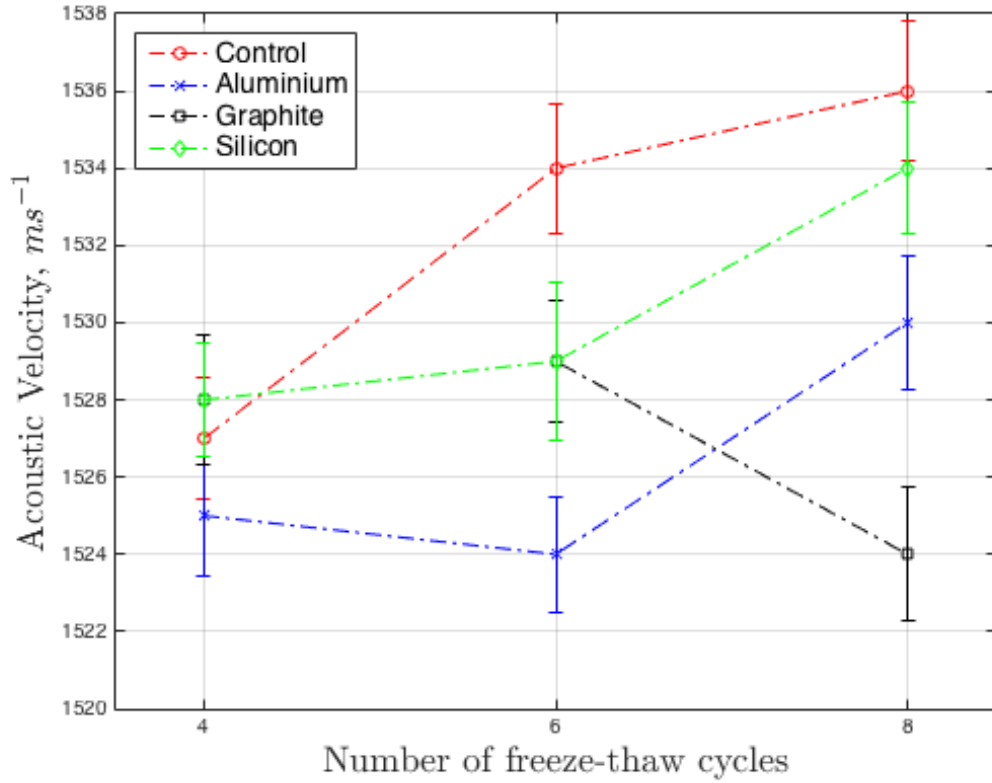
Figure 5.4: Acoustic velocity for 4, 6, and 8 cycle test samples.

The attenuation coefficient results shown in Fig. 5.5 fall broadly within the anticipated range for the number of freeze-thaw cycles at an insonation frequency of 2 MHz [74, 75]. The introduction of scattering agents can be seen to increase the attenuation coefficient of PVA-C, and this effect can similarly be observed by increasing the number of freeze-thaw cycles in the control samples. The results for silicon carbide fall outside of the general trend suggesting there may be a problem with this sample, and the attenuation coefficients measured for all samples, except that of 4-cycle aluminium oxide, fall outside the recommended IEC standard of $(0.5 \pm 0.05) \times 10^{-4} f dBm^{-1}$. This highlights the main problem with PVA-C based phantoms; it is difficult to accurately obtain the recommended attenuation coefficient [74]. However, the results show it may be possible to balance the acoustic velocity and attenuation coefficient requirements using aluminium oxide.
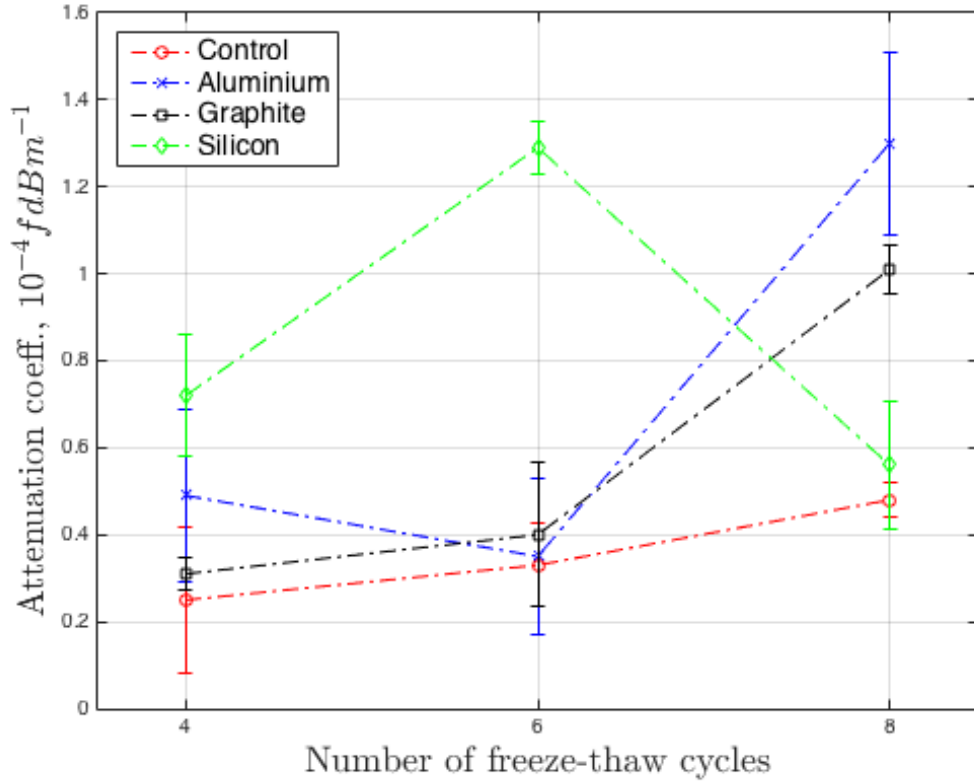
Figure 5.5: Attenuation coefficient for 4, 6, and 8 cycle test samples.

Finally, the backscatter coefficient results in Fig. 5.6 show that the introduction of the scattering agents has been observed to reduce the backscatter coefficient of PVA-C, and this effect increases with the number of freeze-thaw cycles in the control samples. Once again, the results for silicon carbide fall outside of the general trend, while the aluminium oxide sample continues to show promise. The overall trend shows that increasing the number of freeze-thaw cycles beyond 6 will result in a backscatter coefficient below the requirement of $(1-4) \times 10^{-28} f^4 m^{-1} Hz^{-4} sr^{-1}$. Notably, the IEC standard places less emphasis on the backscatter coefficient requirement, particularly at frequencies below 4 MHz.
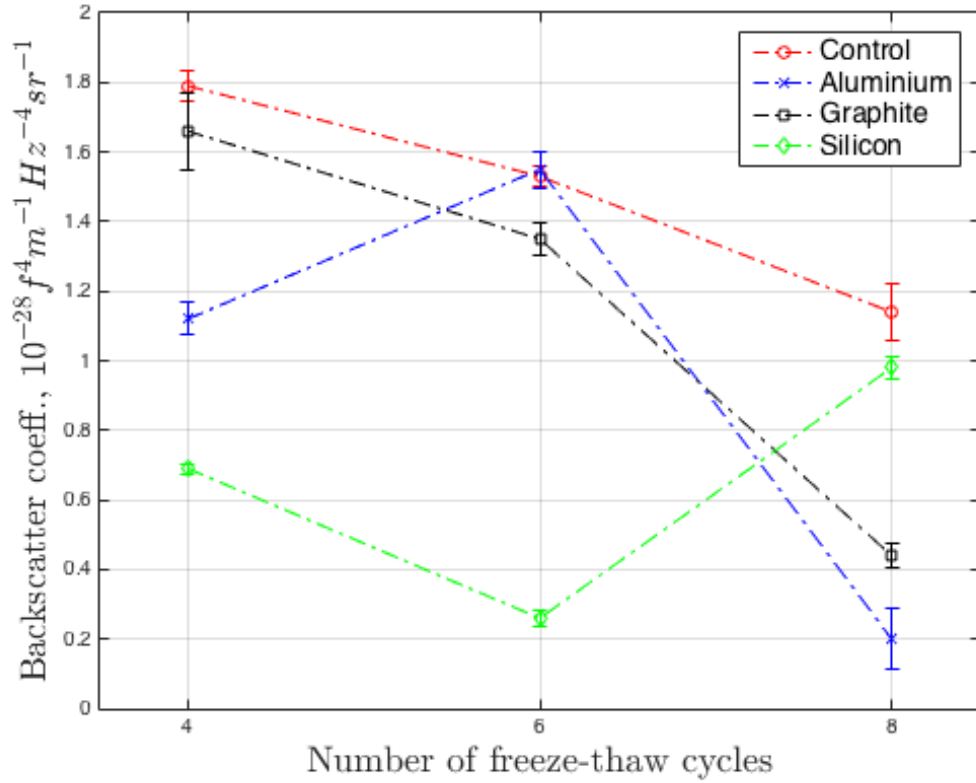
Figure 5.6: Backscatter coefficient for 4, 6, and 8 cycle test samples.

5.3.4   TMM Test Sample Analysis

Although the material benefits of PVA-C are clear, it requires additional scattering agents to achieve acoustic properties consistent with recommended standards. Tests

using common scattering agents showed that, although it was difficult to get truly consistent results, a 4-cycle TMM with 1% aluminium oxide can achieve acoustic properties that are agreeable with IEC standards, and can be used in wall-less flow phantoms. Subsequent preparations have shown this process to be repeatable in small volumes, however the overall velocity, attenuation, and backscatter results suggest it may be difficult to achieve truly consistent results with PVA-C with different laboratory production equipment. Furthermore, the inconsistent results observed with both graphite and silicon carbide are thought to be caused by difficulty in achieving an even dispersal of powder in aqueous solution, resulting in an inhomogeneous TMM. In the case of silicon carbide, the particles were observed to settle at the base of the solution, whilst graphite particles tended to cloud or cluster within the solution. To guarantee consistent results, a mechanical mixing system is preferred to hand mixing as this is likely to improve powder dispersal, whilst it is recommended that careful adherence is given to each step in TMM preparation process to guarantee repeatability. In the flow phantom design in the descriptions that follow, a TMM based on 4-cycle PVA-C with 1% aluminium oxide was used.

Fig. 5.7 shows an image of the specially designed perspex container used for the TCD flow phantom, with graduated markings for accurate placement of the transducer element at the required insonation depth. The steel rod used to create the vessel channel can also be seen. This rod was positioned during the manufacturing process and the freeze-thaw cycles. It was carefully removed once the PVA-C process was complete. The final design was lined with low profile, coarse synthetic grass[vii] to provide acoustic damping to minimise ultrasound reflections from the base and side walls, and improve the SNR.

[vii]Synthetic grass (6 mm/flat blade), Express Grass, Trinity Trading Estate, Sittingbourne, Kent ME10 2PG.
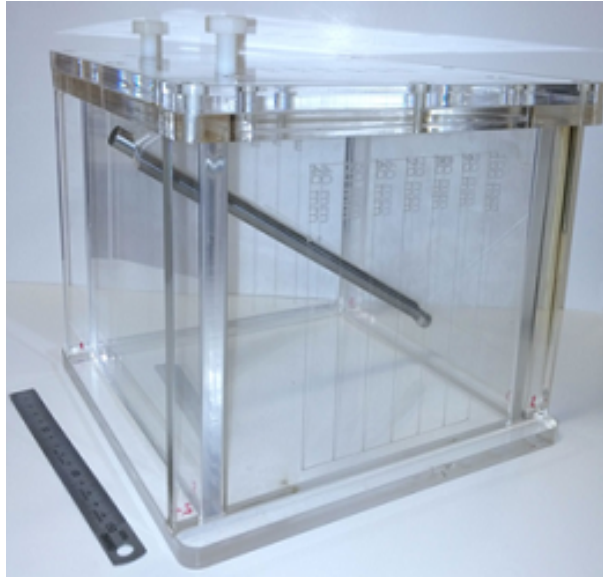
Figure 5.7: Custom designed perspex box for the TCD ultrasound flow phantom.

5.4   Flow Phantom Test Bench

A flow phantom test bench was created to analyse and compare the theoretical and measured acoustic characteristics of a TCD ultrasound propagation channel, as shown in Fig. 5.8.
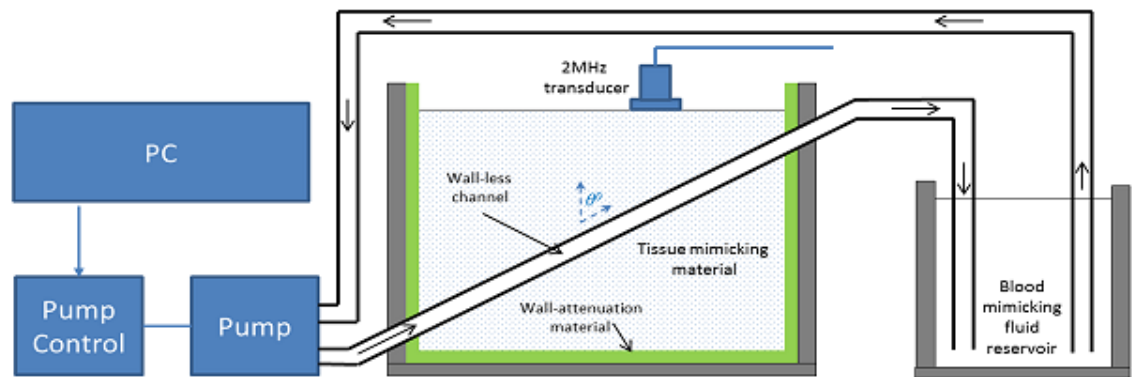
Figure 5.8: A TCD ultrasound flow phantom system.

The test bench consists of a portable, 2 MHz, power-motion or single-channel TCD (*PMD 100, Spencer Technologies*) ultrasound system [80], a windows computer running LabVIEW™(*National Instruments*), a pump and pump-controller (*Department of Clinical Physics & Bioengineering, NHS Greater Glasgow and Clyde*) ca-

pable of operating with constant and pulsatile flow, connected to a 68-pin data acquisition (DAQ) PC card via a shielded connector block (*National Instruments SCB-68*), a PVA-C flow phantom and reservoir of blood mimicking fluid (BMF) [76]. An image of the test bench is shown in Fig. 5.9.
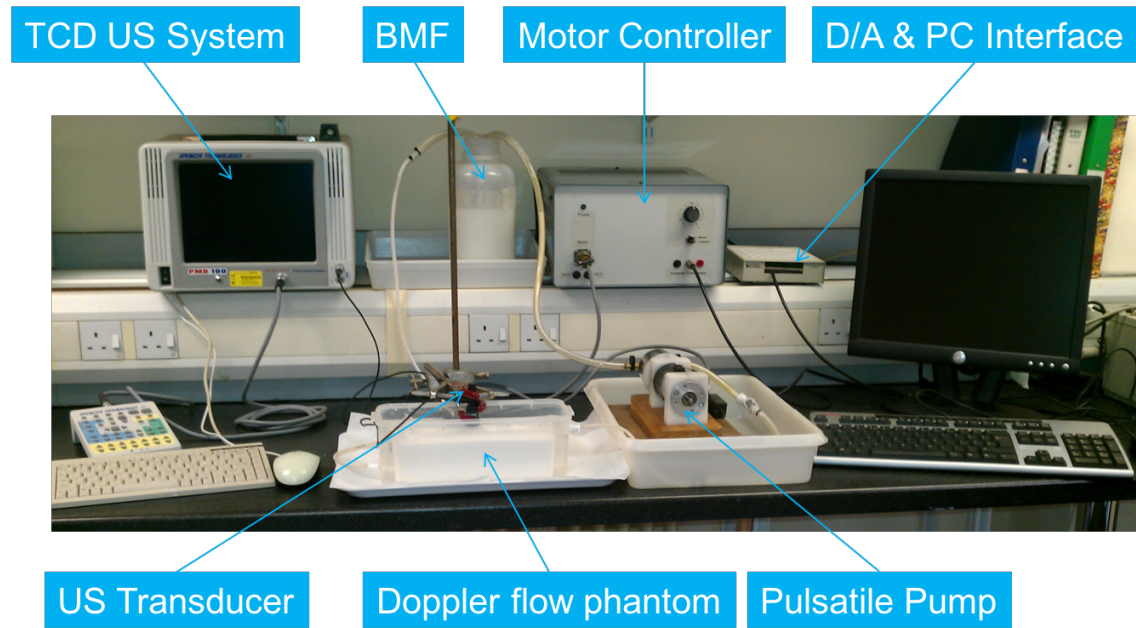
Figure 5.9: An image of the TCD ultrasound flow phantom test bench used in the experiment.

A LabVIEW™application was used to synthesise a blood flow waveform and drive the pump using pulsatile flow via the DAQ and pump controller. This process circulated BMF through the flow phantom whilst a single-element 2 MHz transducer was placed on the flow phantom to capture Doppler ultrasound.

5.4.1   Flow System Data Acquisition

The flow system is designed to replicate a patient measurement system. The 2 MHz transducer is placed on the phantom, above the vessel channel and at the desired insonation depth. The received signal can be used, in combination with the spectrogram and M-mode displays on the TCD system, to manoeuvre the transducer to a

point where the received spectrogram displays the blood flow waveform and the M-mode display indicates the desired insonation depth (as shown in section 2.4.2, Fig. 2.3). Using the TCD ultrasound system in single channel mode whilst insonating at a depth of approximately 40 mm and using 10% of maximum power, raw *Doppler* signals were acquired and recorded from the flow phantom, and exported as audio files consisting of 32-bit floating point data sampled at a frequency of 44.1 kHz. The data acquired from the TCD phantom is a real signal and contains no complex plane. In order to get a analytical representation of the signal, the real signal undergoes a *Hilbert* transform to restore the complex plane using a Matlab^{TM}function.

5.5   Summary

In this chapter, PVA-C TMM was evaluated with a number of potential scattering agents for use in a TCD ultrasound flow phantom. Although the material benefits of PVA-C are clear, it requires additional scattering agents to achieve acoustic properties consistent with recommended flow phantom standards. Tests using common scattering agents showed that a 4-cycle TMM with 1% aluminium oxide was able to achieve acoustic properties that are agreeable with IEC standards. As such, this TMM is considered suitable for use in wall-less flow phantoms for investigation of multi-path propagation effects in TCD ultrasound systems. However, the overall velocity, attenuation and backscatter results suggest it may be difficult to achieve truly consistent results with PVA-C. It is possible that some minor differences in production technique and variations in the dispersal of the scattering agents can account for some inconsistencies in the results observed. Indeed, the variability in results of the TMM sample tests suggest that further analysis is required at 2, 3, 5, and 7 cycles to establish a clearer pattern of results for acoustic velocity, attenuation coefficient, and backscatter coefficient. In particularly, it was observed that when using silicon carbide and graphite scattering agents, it is difficult to achieve an even dispersal of powder in aqueous solution, resulting in an inhomogeneous TMM.

Notwithstanding these results, a TCD flow phantom was created using a TMM based

on the 4-cycle freeze-thaw process and 1% aluminium oxide powder (3μ particle size), as described. This phantom, and the accompanying flow system as specified, provides a suitable test bench for the verification of non-isotropic TCD ultrasound propagation channel models, as discussed in Chapter 6.

Chapter 6

Verification of 3-D Non-isotropic TCD Ultrasound Propagation Channel Models

6.1 Introduction

In this chapter the 3-D non-isotropic TCD ultrasound propagation channel models, described in Chapter 4, are verified against measured results from the TCD flow phantom, described in Chapter 5, and a patient recordings database. The verification analysis will compare plots of the first and second order statistics; amplitude PDF, phase PDF, ACF, LCR, and AFD. The discussion will expand on areas of agreement and disagreement before assessing the usefulness of the non-isotropic TCD ultrasound propagation channel models for further study of TCD.

6.2 Patient Recordings Database

A database of anonymised and de-personalised TCD patient examinations was developed by data-mining archived routine clinical tests of blood flow through the MCA. This database was created in accordance with UK health information governance principles [81] and with guidance from Glasgow health board's *Caldicott* patient confidentiality guardian.

Raw *Doppler* signals were acquired from 83 examinations of 34 adult patients, recorded using a Spencer Technologies TCD ultrasound system. All patients were being treated for ischemic stroke or were identified as at risk of a stroke event. Audio files consisting of 32-bit floating point data sampled at 48 kHz were recorded, in addition to peak systolic and diastolic blood flow in ms^{-1}, insonation power (% full power), SNR, mean, and variance. The captured data sets also include notes on perceived signal quality, patient sex (M/F), and recording date. The data set was exported to a Matlab™MAT-file for convenience of data processing and statistical analysis.

All patient recordings were pre-processed and categorised to determine suitability for analysis. Pre-processing was performed in two steps: Firstly a SNR measure was performed and only recordings with an SNR greater than 3 dBs were deemed acceptable for analysis. Secondly, all recordings with evidence of detected embolus were excluded from analysis, since these exhibit abnormal high-frequency HITS which are non-standard signal features that may offset statistical averaging. After pre-processing, 33% of the recordings in the patient database from 11 patients were determined acceptable for detailed analysis. As in the case of the TCD phantom data set, described in section 5.4.1, the patient recording data sets are real signals containing no complex plane. In order to obtain an analytical representation of the signal, in the final stage of pre-processing the real signal undergoes a *Hilbert* transform using a Matlab™function.

6.3   Model Optimisation

The parameters $f_{D_{max}}$, K, k, σ, N, v, θ_K, α_0, and β_0 were optimised in the theoretical and simulation models were optimised to achieve as close a fit as possible with the patient measurements. Using Matlab™, fitting algorithms were used to process the PDFs and ACF of the theoretical model and patient measurements over three stages. Firstly, the optimal values of σ and K were obtained by fitting the amplitude PDF

to the PDF of the patient measurements. Secondly, the optimal value of θ_K was obtained by fitting the phase PDF to the PDF of the patient measurements. Finally, the optimal values of $f_{D_{max}}$, k, v, α_0, and β_0 were obtained using a multivariable sum of least squares regression algorithm to fit the ACFs to the statistical average of the patient measurements. The optimised parameter values used to achieve the results presented are described in Table 6.1.

Table 6.1: Definition of parameter values following 3-D spherical non-isotropic model optimisation.

Parameter	Value	Definition
f_c	2 MHz	insonation frequency of TCD ultrasound
c	1500 ms^{-1}	estimated speed of sound in tissue
$f_{D_{max}}$	1.099 kHz	maximum *Doppler* frequency
K	0.0078	*Rician* K-factor
k	4.201	VMF concentration parameter
σ	0.48	standard deviation of the PDF
N	15	number of incident scatterers
v	0.412 ms^{-1}	blood flow velocity within the isonated vessel
α_0	0°	mean azimuth angle of arrival
β_0	0°	mean elevation angle of arrival
θ_K	0.165 rad	$arg\{m(t)\}$

The insonation frequency (f_c) is a predefined feature of the TCD ultrasound system and was fixed at 2 MHz. The speed of sound in tissue c was estimated as 1500 ms^{-1}; a compromise based on the average acoustic properties of tissue in the cranium. Importantly for the comparison of the models and the phantom study, tissue is assumed to be homogeneous and does not account for complex tissue structures, or acoustic interfaces encountered between skin and bone etc. The number of sinusoids in the SoS simulation model N, was chosen to be as small as possible whilst providing a close match between the simulation model and the optimised theoretical reference model. A small value of N leads to a computationally efficient simulation model.

6.4 Analysis of Theoretical, Simulated and Measured Results

In this section we analyse and compare the plots of the PDFs, ACFs, LCRs and AFDs of the 3-D non-isotropic TCD ultrasound theoretical reference model, simulation model, SoS simulation results, with the measurements from phantom and patient recordings.

6.4.1 Amplitude & Phase PDFs

Fig. 6.1 and Fig. 6.2 show the amplitude and normalised phase PDFs of the theoretical reference model, simulation model, SoS simulation results, phantom measurement, and patient measurements respectively. The key parameters in this analysis are K, σ, θ_K and N.

Firstly, considering the amplitude PDF in Fig. 6.1, the patient measurements provide close agreement with the theoretical and simulation models. As $K = 0.0078$, this confirms that the patient measurements exhibit a small but detectable LoS component, but this LoS component is not dominant and, as a result, the the amplitude PDFs exhibit a *Rayleigh* scattering profile. It also shows the standard deviation of the patient measurements match the models, where the standard deviation is observed as $\sigma = 0.48$. Both K and σ have been optimised effectively, as demonstrated by the close fit of the models and patient measurements.

Figure 6.1: The amplitude PDF of the 3-D non-isotropic spheroid theoretical reference, simulation, and SoS simulation results, phantom measurement and patient measurement, where $K = 0.0078$, $\sigma = 0.48$, and $N = 15$.

The phantom measurements plot in Fig. 6.1 exhibits a notable difference to the others, indicating that both σ and K are marginally greater in this case. This suggests the LoS component in the phantom measurements is marginally more significant and there is slightly greater dispersion of the signal amplitude probability distribution. These differences are thought to arise from compromises in the flow phantom design. For example, the flow phantom is homogeneous, where as real tissue structures are complex, including skin, bone, and tissue interfaces. In addition to the material compromises that are made when constructing a flow phantom, background noise from the mechanical pump system and turbulent flow in the vessel channel can also be a source of noise in the recorded signal. These differences are proposed

to explain the variation in signal amplitude observed in the phantom measurements.

For the normalised phase PDF in Fig. 6.2, the plots show phase θ is a random variable with normal distribution. The patient measurements provide very close agreement with the theoretical and simulation models, whilst once again there is a small disagreement with the phantom measurements. The phantom phase PDF plot shows there is slightly greater phase dispersion in the phantom measurements. Once again, it is reasonable to assume this difference can be accounted by the reasons stated previously for the amplitude PDF.
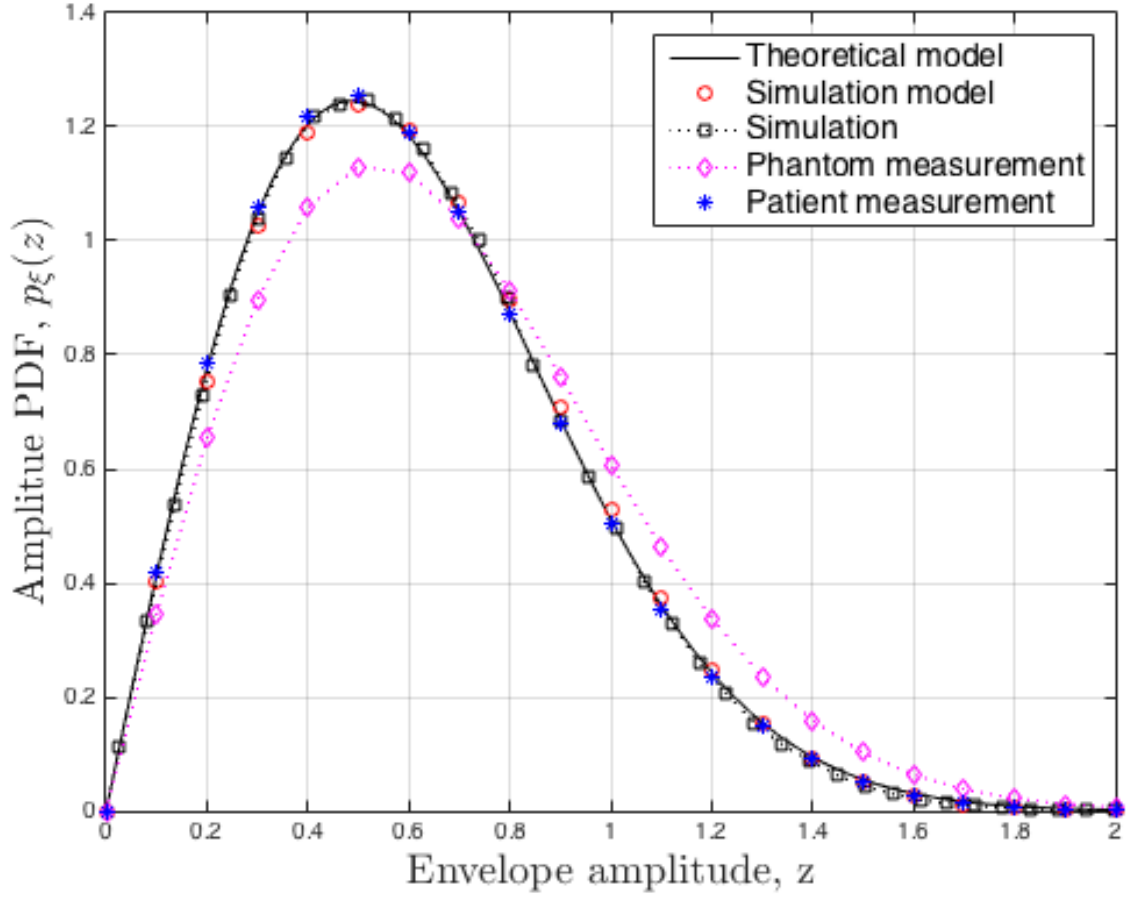

Figure 6.2: The phase PDF of the 3-D non-isotropic spheroid theoretical reference, simulation, SoS simulation results, phantom measurement and patient measurement, where $K = 0.0078$, $\sigma_0 = 0.48$, $\theta_K = 0.165$ radians, and $N = 15$.

A further feature observed in the plots presented in Fig. 6.2 is the small but noticeable central phase offset, such that the optimised value of $\theta_K = 0.165$ radians. The source of this phase offset and the degree to which it might be anticipated are unclear from the analysis. It is thought this may be an artefact in the TCD system, data acquisition process, or may have been introduced as a result of the *Hilbert* transform during signal pre-processing. However, the effect is small and doesn't appear to be significant. Although further investigations are required to understand this observation more fully, it is also possible an imperfection in the ultrasound system could be the cause. For example, in communications systems using phase-shift keying (PSK) modulation, there is always a frequency and phase shift. Such imperfections are common in communications systems and acceptable from and engineering view point. Indeed, such features can be used to radio 'fingerprint' unique transmitters for security applications [82].

In summary, it is clear from the plots of both amplitude and phase PDF that the non-isotropic propagation channel models demonstrate very good agreement with the patient measurements, whilst the phantom measurements are encouragingly similar. The utility of the models is provided by the ability to optimise the parameters K, σ and θ_K to fit the patient measurements. The differences observed in the phantom measurements highlight the limits in accuracy achieved by this flow system in terms of acoustic and physiological equivalence, but also sign post an area of further refinement through investigation of flow settings and material design.

6.4.2   Temporal ACFs

Fig. 6.3 shows the ACF of the theoretical reference model, simulation model, SoS simulation results, phantom measurement, and patient measurement. The key parameters in this analysis are; K, $f_{D_{max}}$, k, α_0, β_0 and N. The plots show the normalised ACF is zero mean, periodic, and has a decaying envelope. There is some variability evident in the amplitude of the decaying envelope for the patient and phantom measurements. This may be due to the variation in blood flow velocity

caused by the cardiac cycle. Normal resting peak diastolic and systolic blood flow velocities in the MCA can typically vary between 0.1 ms^{-1} and 1 ms^{-1}, whilst velocities in diseased arteries can vary more widely. Although the interval $(t+\tau)$ is small compared to the relative change in motion, in order to better support clinical analysis, models may be required which support both time-varying and motion-varying cases in order to describe the channel correlation properties more accurately.
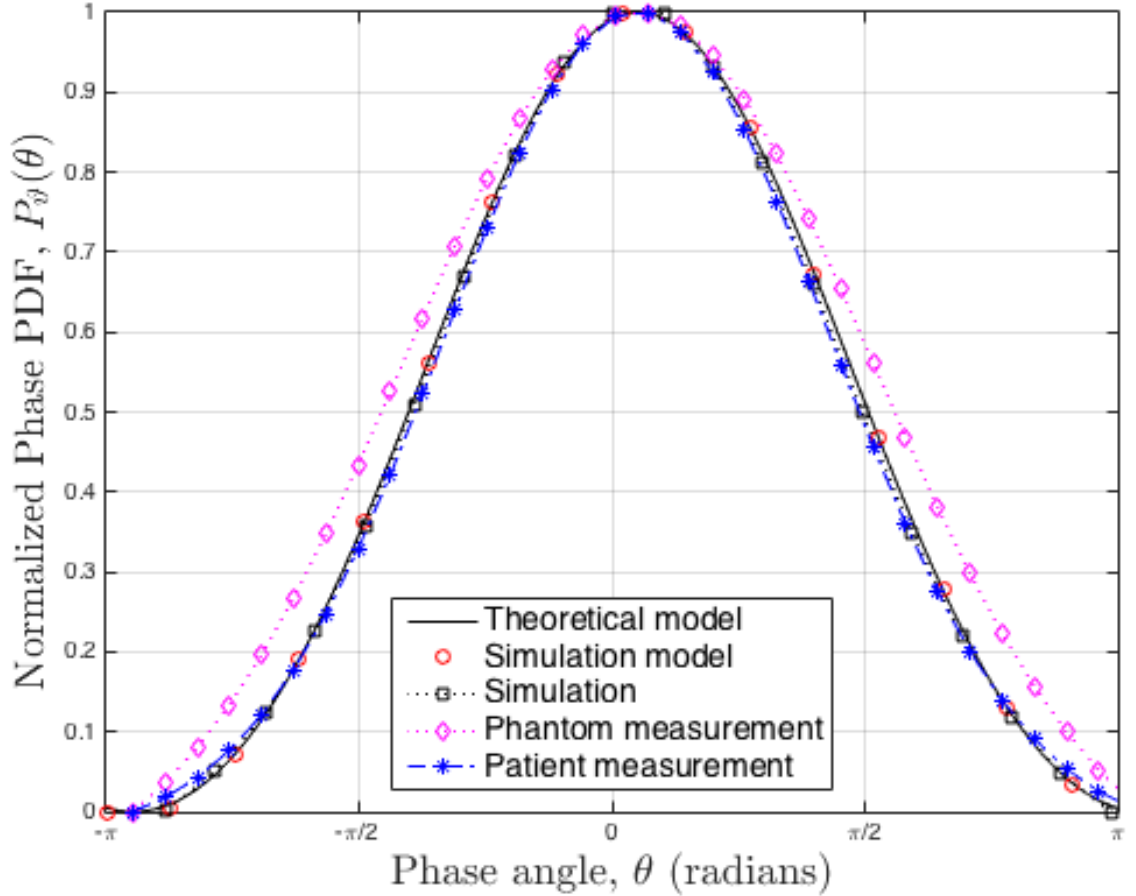

Figure 6.3: The normalised ACF of the 3-D non-isotropic spheroid theoretical reference, simulation, SoS simulation results, phantom measurement and patient measurement, where $f_{D_{max}} = 1.099$ kHz, $K = 0.0078$, $k = 4.201$, $N = 15$, $\alpha_0 = 0°$ and $\beta_0 = 0°$.

Nonetheless, the theoretical reference model, simulation model, SoS simulation, and

patient measurement plots show very good correlation up to approximately 0.5 ms. After 0.5 ms, the patient measurement remains loosely correlated before the simulation model and SoS simulation results diverge at approximately 4.2 ms. The close agreement of the theoretical reference model, simulation model, and SoS simulation results confirms that the number of sinusoids in the SoS simulation, $N = 15$, is an excellent choice. Furthermore and importantly, the level of agreement of the models and the patient measurements up to approximately 4.2 ms confirms the error minimisation function has optimised the parameters $f_{D_{max}}$, k, α_0, and β_0 to the patient measurements.

Unfortunately, as a result of the statistical differences identified between the patient and phantom measurements in the PDF analysis, and further compounded by the parameter optimisations, the phantom ACF measurement shows poor agreement with the models.

6.4.3 Envelope LCRs & AFDs

At this stage in the analysis, the parameters used in both the LCR and AFD have been fully optimised. Fig. 6.4 shows the normalised LCR in decibels of the theoretical reference model, simulation model and SoS simulation, phantom measurement, and patient measurement. This plot show remarkably close agreement between the models and experimental data below a normalised envelope level of approximately 8 dBs, above which we reach the limit of the recording levels of the measured results. The close fit with the SoS simulator reaffirms the narrow band flat fading nature of the TCD *Doppler* system.
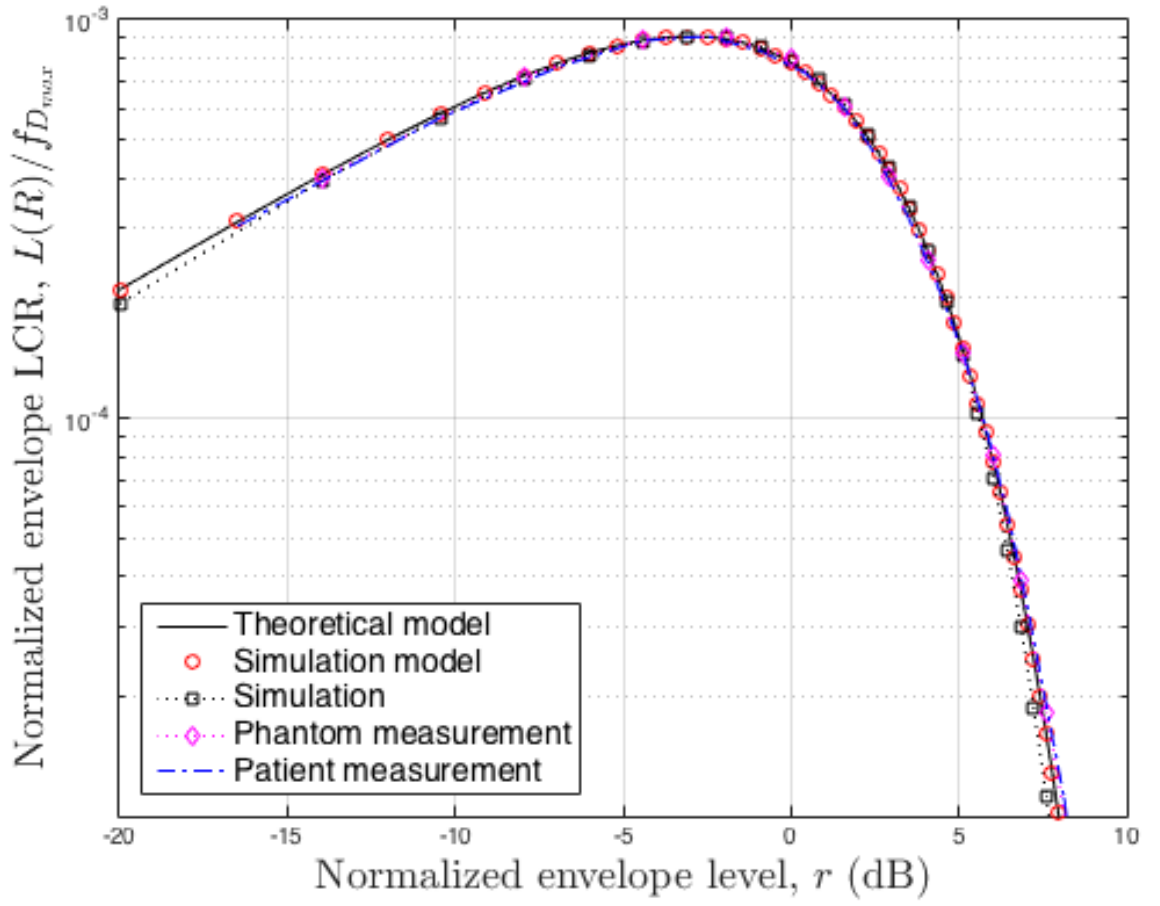
Figure 6.4: The normalised LCR (dB) of the 3-D non-isotropic spheroid theoretical reference, simulation, SoS simulation results, phantom measurement and patient measurement, where $f_c = 2$ MHz, $f_{D_{max}} = 1.099$ kHz, $K = 0.0078$, $k = 4.201$, $N = 15$, $\alpha_0 = 0°$ and $\beta_0 = 0°$.
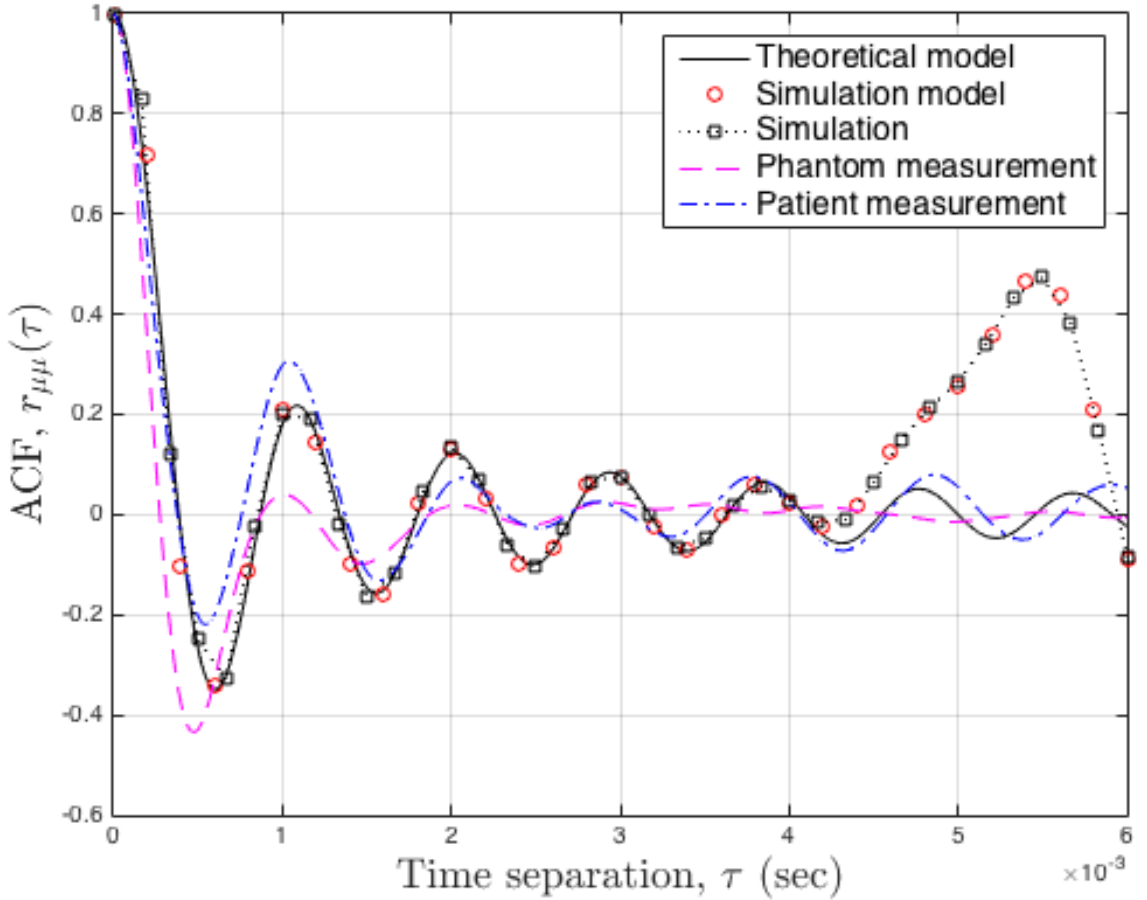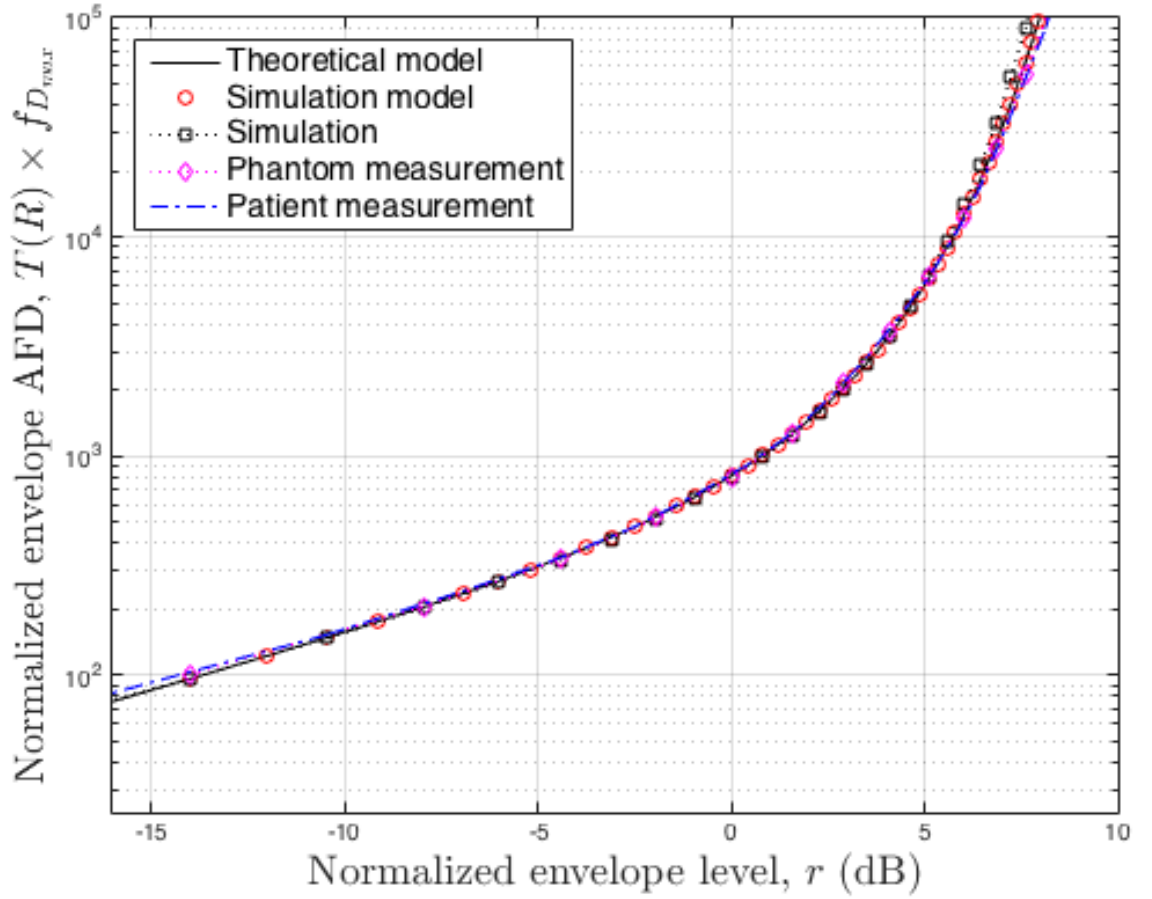
Figure 6.5: The normalised AFD (dB) of the 3-D non-isotropic spheroid theoretical reference, simulation, SoS simulation results, phantom measurement and patient measurement, where $f_c = 2$ MHz, $f_{D_{max}} = 1.099$ kHz, $K = 0.0078$, $k = 4.201$, $N = 15$, $\alpha_0 = 0°$ and $\beta_0 = 0°$.

Fig. 6.5 shows the normalised AFD in decibels of the theoretical reference, simulation, SoS simulation results by experiment, phantom measurement and patient measurement. Consistent with the LCR, this plot shows close agreement between the theoretical, simulation, and experimental data up to a normalised envelope level of approximately 8 dBs.

The close agreement of the LCR and AFD envelopes respectively confirms the non-isotropic SoS channel simulator is a very good match to the patient measurements and provides an extremely useful reference for TCD ultrasound.

6.5   Summary

In this chapter, the 3-D non-isotropic TCD ultrasound propagation channel models were verified against *Doppler* ultrasound measurements obtained from a TCD flow phantom and a patient measurements database. Whilst slight differences were observed between the TCD flow phantom and the patient measurements, a comparison of the optimised stochastic models with the patient database demonstrated a strong level of agreement. Further, these results suggest that the TCD ultrasound propagation channel has a weak LoS component.

The degree of difference observed between the flow phantom and patient measurements of PDFs and ACF are disappointing but not surprising. These differences highlight the limitations of equivalence between medical phantoms and patient measurements. Ultrasound medical flow phantoms provide a simple reference system, with acoustic properties which are close, but not identical, to those measured in real patient data. The cumulative effect of compromising on material selection and flow system specification make true parity very difficult to achieve.

The proposed models establish a clear benchmark from which the thorough investigation and analysis of the channel statistics of TCD ultrasound may be understood. Although a relatively small patient cohort have been tested, with only 11 patient samples of adequate criteria available for analysis, the models described have been demonstrated to be tuneable and adaptable to the observed statistical patient average.

As a result of the flexibility and utility of the non-isotropic models verified in this chapter, it is anticipated that these will have extremely useful application value in the design and assessment of new and improved techniques for qualitatively analysing embolisation events in future TCD ultrasound systems. These results can also inform and guide further stochastic analysis in this field, and may provide a basis for improving our understanding of scattering effects and fading intervals

in new and emerging signal processing methods for other applications of *Doppler* ultrasound.

In the final chapter, conclusions on the value of this research are offered and areas of future work are proposed which may help to mitigate some of the issues associated with multi-path fading in TCD signal ultrasound propagation channels.

Chapter 7

Conclusions & Future Work

Improvements in our ability to detect and characterise emboli in the MCA will directly benefit the lives of those who have, or are at risk of having, a stroke. In an effort to deal with the financial burden of an ageing population, health services around the world are seeking imaginative ways to move from a reactive model of healthcare, to a proactive and preventive model. At this same juncture, those considerable advances we have witnessed in disease treatments and life expectancy made possible by pharmacological discoveries in the past century are beginning to slow. A transition is underway, where we can expect healthcare advances in the next century to emerge from technological innovations in, for example, genomics, big data, machine learning, artificial intelligence, and wearable technologies. It is within this climate of change that engineers, scientists, and clinicians must collaborate, evaluate and consider how to take advantage of recent technological advances, and meet the requirements of the next generation.

Within the context of these much greater ambitions, the inspiration emerged to re-evaluate TCD ultrasound against the latest clinical requirements. The next technological breakthrough in TCD ultrasound requires a transition from systems that quantify embolisation events to those which qualitatively analyse embolisation events. The emergence of such a system would increase the capabilities of our stroke clinicians, allowing them to detect embolus much earlier in asymptotic patients, assess the composition of embolus, and prescribe the most effective interventions. A

strategy to, above all, save lives and prevent disabilities as a result of stroke.

Although detection of MES is a mature application of TCD ultrasound, new algorithms are being developed to help characterise and classify MES. In chapter 2 a review of the latest MES detection algorithms and enhanced DSP techniques was described. A reasonable conclusion from this work was the prediction that the combination of a hybrid MES detection algorithm and a suitable modulation scheme should allow the next generation of TCD ultrasound systems to achieve reliable and robust MES detection at $EBR_{min} \geq 5$ dBs or less. Furthermore, such systems may also be capable of precise emboli motion tracking. However, since existing acoustic wave modelling methods do not support analysis of the channels information transfer characteristics, a stochastic propagation channel model is required to support the design and development of an optimal TCD ultrasound system based on this approach. Since many of these MES detection algorithms use advanced signal processing techniques previously applied to improve the robustness and reliability of wireless communications, it is fitting that we may also look to wireless communications systems for methods which help us to optimise and improve these techniques. Taking inspiration from stochastic models developed for wireless communications systems, the objective of this thesis was to derive, define, and verify 3-D stochastic propagation channel models that can be used to develop and enhance techniques for detecting and tracking emboli in the intra-cranial arteries.

The channel models described in chapters 3 and 4 offer a first step in the process of using stochastic analysis in TCD ultrasound to inform the development of these algorithms. The simulation models provided by this research offer a method of reproducing the statistical properties of TCD ultrasound, and, as demonstrated, these models can be optimised to efficiently and accurately match measured results, as demonstrated by the verification of the 3-D non-isotropic TCD ultrasound propagation channel models described in chapter 6. This chapter provides a brief summary of the research findings resulting from this work and proposes several suggestions for future work.

7.1 Summary of Results

The key results from this thesis are summarised below.

i. **3-D spherical TCD ultrasound propagation channel models:** In Chapter 3, 3-D isotropic spherical scattering models were developed for analysis of *Rayleigh* fading environments. The proposed reference was based on a half-spheroid geometry that was adapted from similar approaches for wireless communications. Mathematical derivations were developed for these models, in terms of the amplitude PDF, phase PDF, temporal ACF, *Doppler* PSD, envelope LCR, and AFD. Additionally, a SoS based channel simulator was described. Parameter optimisations were performed using the LPNM method and numerical results were reported for the case $\frac{b}{a} = 1$, where a is the radius of the base and b is the height of the half-spheroid, such that the maximum *Doppler* frequency $f_{D_{max}} = 1.07$ kHz, the standard deviation $\sigma = 1$, and the number of sinusoids in the SoS simulation model $N = 30$. The numerical results and analysis showed good agreement between the models, but issues of complexity were raised, due to the requirement to jointly analyse the amplitude PDF in both azimuth and elevation. Furthermore, these models are not sufficiently flexible to consider the presence or importance of a LoS scattering component.

   To address these deficiencies, in Chapter 4, 3-D non-isotropic spherical scattering models were developed for analysis of *Rician* fading environments, which can be used to consider the presence of a LoS component. Again, the proposed reference model was adapted from similar approaches for wireless communications, however the model geometry was spherical in this case. Additionally, the VMF probability distribution was used to characterise the scattering distribution as a method of reducing complexity by jointly analysing azimuth and elevation angles in the probability distribution. Mathematical derivations were developed for the theoretical reference and simulation models, and a SoS based channel simulator was described. Parameter optimisations were

performed using the MEV and numerical results were reported for the case where the maximum *Doppler* frequency $f_{D_{max}} = 1.09$ kHz, the *Rician* K-factor $K = 0.0078$, the VMF concentration parameter $k = 4.2$, the standard deviation $\sigma = 0.48$, and the number of sinusoids in the SoS simulation model $N = 15$. The numerical results and analysis showed strong agreement between the models. These models demonstrated improved performance and accuracy in comparison to the previous case, requiring lower numbers of incident scatters 'N' in the SoS simulator, whilst offering the flexibility to consider the significance of a LoS scattering component.

ii. **A new flow phantom for TCD ultrasound studies:** In Chapter 5, a novel wall-less *Doppler* flow phantom was described. This medical blood flow phantom was designed for analysis of 3-D TCD ultrasound channel models. The process of material selection and construction is described in detail. Analysis of the available scattering agents demonstrated that 1% aluminium oxide powder (3μ particle size, measurement by weight) per PVA-C preparation, with 4 freeze-thaw cycles, offered the optimal results for acoustic velocity, attenuation, backscatter coefficient, and impedance. A flow system test bench was specified for the resulting phantom, and the details of data acquisition were described.

iii. **Verification of the 3-D non-isotropic TCD ultrasound propagation channel models:** In Chapter 6, the non-isotropic spherical scattering models were verified against flow phantom and patient measurements. These models were fitted to the patient measurements using a multivariable sum of least squares regression fitting algorithm. Numerical results were reported for the case where the maximum *Doppler* frequency $f_{D_{max}} = 1.099$ kHz, the *Rician* K-factor $K = 0.0078$, the VMF concentration parameter $k = 4.201$, the standard deviation $\sigma = 0.48$, the mean AAoA $\alpha_0 = 0°$, the mean EAoA $\beta_0 = 0°$, the phase offset $\theta_K = 0.165$ radians, and the number of sinusoids in the SoS simulation model $N = 15$. The numerical results and analysis showed strong agreement between the models and the patient measurements. Differences

observed in the flow phantom PDFs and ACF were accounted for by design compromises and flow system performance issues. Furthermore, although there is limited patient test data from which to draw a definitive result, it has been established by this analysis that the TCD ultrasound propagation channel has narrow band flat fading characteristics and no dominant LoS component. In conclusion, the strong agreement between the 3-D non-isotropic TCD ultrasound propagation channel models and the patient measurements have establish a clear benchmark from which the thorough investigation and analysis of the channel statistics of TCD ultrasound may be understood.

7.2   Future Work

There are several areas of future work that can be developed from this thesis.

i. **Validation of the 3-D non-isotropic spherical TCD ultrasound propagation channel models:** The verification process described in Chapter 6 was performed on a small number of patient measurements, and this reduces the statistical significance of the results. In order to achieve more scientifically robust results, a process of validation is required. Such a process would include a measurements data set from a much larger patient sample group, and should include sub-sample groups of both normal and diseased patients. This research would take the methods and models verified in Chapter 6 and, having established an adequate patient sub-sample size, optimise and analyse the channel models against each of the sub-sample groups. This process would establish accurately the model parameters and statistical properties of TCD ultrasound systems and could attempt to identify any significant differences across the sub-groups. Such research would require approval using a supporting application to the Integrated Research Application System (IRAS), an ethics application and, most likely, clinical support.

ii. **Adaptation of 3-D non-isotropic spherical TCD ultrasound propagation channel models for variable blood flow velocity:** The models

developed in Chapters 3 & 4 assume a constant velocity of blood flow in the insonation region. This assumption is reasonable over the interval $(t + \tau)$, since this interval is small compared to the relative change in motion at blood flow rates, and given that normal resting peak diastolic and systolic blood flow velocities in the MCA typically vary between 0.1 ms^{-1} and 1 ms^{-1}. However, in diseased arteries, blood flow velocities can vary more widely and may peak at more than double the mean resting rate. In order to confirm the original assumption, further investigations into models which support both time-varying and motion-varying cases would be required. This work could be framed to fit within the validation study described above.

iii. **Fading mitigation:** Wireless communications systems have developed several mitigation strategies to counter act the presence of multi-path fading, such as diversity, coding, equalisation etc. Some such techniques may not be appropriate for *Doppler* ultrasound, however a research question could be formed to consider appropriate methods of fading mitigation. For example, a rake receiver. It is feasible in *Doppler* ultrasound to consider a multi-element transducer array and complementing sub-receivers. Using techniques complementary to existing methods in wireless communications, each sub-receiver would decode a multi-path component and use a weighted algorithm to recombine the result. In the presence of reflections from intra-vascular bodies such as embolus, such a technique could be used to significantly improve the detection and characterisation process.

iv. **MES Signal Pattern Classifier:** In combination with the front-end fading mitigation improvements that have been suggested above, analysis of existing MES detection algorithms in Chapter 2 showed there is an opportunity to investigate signal pattern classifiers and adopt a machine learning approach to improve the robustness and reliability of MES detection. There are many possible methods of signal classification; statistical, decision-tree, neural networks etc. Although there is existing literature on binary classification using parametric signal processing, it is not clear at this stage what the most opti-

mal method would be. However, the performance and accuracy of all signal classifiers rely on a sufficient set of training data. This problem therefore requires the creation of a database of patient TCD recordings which can act as a repository of embolus detection signals from which to harvest a training data set. From experience of establishing the relatively small patient measurements database used in this research, this would require a formal approach to one of the NHS health boards research and development groups. At the current time, I'am unaware of a process by which TCD patient measurement recordings are routinely digitally archived within patient records. Such a requirement would therefore need to establish a clear case for social health economic benefit, an assessment on current clinical practice, and formation of a concise research question. Such research would most likely require approval using a supporting application to the Integrated Research Application System (IRAS), and would require an ethics application and, most likely, clinical support.

v. **Flow phantom design:** The flow phantom design described in Chapter 5 could be improved in several ways. Firstly, the TMM sample results described in section 5.3.3 should be extended to consider additional freeze-thaw cycle tests at 3, 5 and 7 cycles. The manufacturing process involved in TMM preparation is extremely slow. Not enough time was given to performing adequate testing in the original research, and three data sample points per test variant is insufficient to draw conclusive results. Furthermore, although the wall-less phantom was a successful design in the experimental work described, the walls of the vessel channel begin to degrade in time and this limits the useful working-life of the phantom. Results should be compared with walled phantoms using standard phantom vessel materials, such as silicon, latex etc.

Appendix A

Derivation of the *Doppler* Equation for TCD ultrasound

A.1 Analysis of Doppler frequency

In this appendix, we derive an expression for the *Doppler* frequency (f_D) in a TCD ultrasound system. The framework for this derivations is provided by figure A.1. This figure helps us to relate the insonation frequency (f_c), the velocity of the wave in the medium (c), the velocity of the observer relative to the medium (v_o) and the velocity of the source relative to the medium (v_s), to the frequency shift between the original insonation frequency (f_c) and the frequency of the reflected pulse $(f_{\alpha)})$ observed at the source, known as the Doppler frequency (f_D).
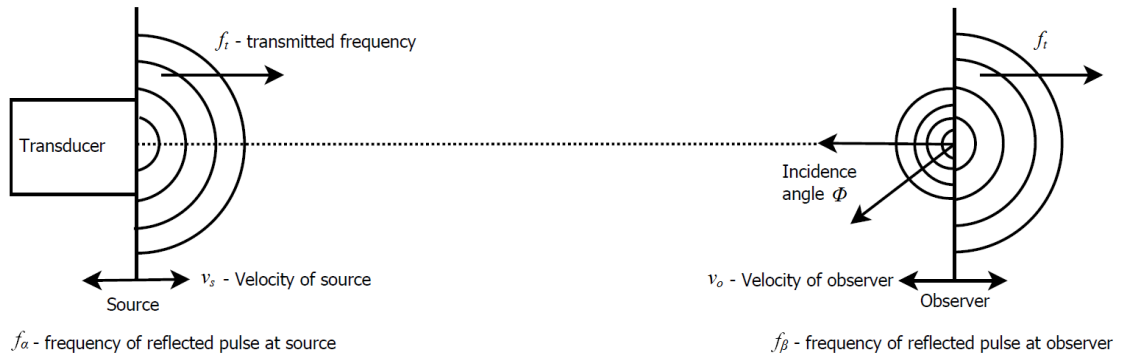
Figure A.1: The Doppler effect, as applied to ultrasound pulse reflection.

Equation (A.1) is the classic definition of f_D as developed by Christian Andreas Doppler, published in 1843,

$$f_D = \frac{(c \pm v_o)}{(c \pm v_s)} \times f_c. \tag{A.1}$$

However, in ultrasound systems we must consider traversing the medium in two directions since our transducer shall transmit an ultrasound pulse and will subsequently receive an echo or reflection;

1. Outgoing pulse; observed Doppler shift frequency f_α.

2. Reflected pulse; observed Doppler shift frequency f_β.

A.1.1 Consider the Outgoing Pulse

From equation (A.1) we derive equation (A.2) for the outgoing pulse, i.e. the Doppler shifted frequency of the pulse at the observer.

$$f_\alpha = \left(\frac{c \pm v_o}{c \pm v_s} \right) \times f_c \tag{A.2}$$

A.1.2 Consider the Reflected Pulse

Now consider the reflected pulse. The reflected pulse must travel back to the source through the medium and can be described by

$$f_\beta = \left(\frac{c \pm v_o}{c \pm v_r} \right) \times f_\alpha \tag{A.3}$$

where v_r is the velocity of the source of the reflected pulse. Through substitution with equation (A.2), equation (A.3) can be re-written as

$$f_\beta = \left(\frac{c \pm v_o}{c \pm v_r} \right) \times \left(\frac{c \pm v_o}{c \pm v_s} \right) \times f_c. \tag{A.4}$$

Since the transducer is stationary, we can consider the transducer velocity (v_s) to be zero. Further, we can consider the velocity of the source of the reflected pulse (v_r) to be equal to the negative velocity of the observer ($-v_o$). Substituting these

values into equation (A.4) gives us

$$f_\beta = \frac{c}{(c - v_o)} \times \frac{(c + v_o)}{c} \times f_c \tag{A.5}$$

which can be further simplified to

$$f_\beta = \left(\frac{c + v_o}{c - v_o} \right) \times f_c. \tag{A.6}$$

A.1.3 Derivation of the Doppler Frequency

The Doppler frequency shift (f_D) observable at the source can be derived by the following steps;

$$f_D = \Delta f = f_\beta - f_c = \left[\left(\frac{c + v_o}{c - v_o} \right) \times f_c \right] - f_c \tag{A.7}$$

$$f_D = \left(\frac{c + v_o}{c - v_o} - 1 \right) \times f_c \tag{A.8}$$

$$f_D = \left(\frac{(c + v_o) - (c - v_o)}{c - v_o} \right) \times f_c \tag{A.9}$$

$$f_D = \left(\frac{2v_o}{c - v_o} \right) \times f_c \tag{A.10}$$

$$f_D = \left(\frac{2v_o}{c} \right) \times f_c \tag{A.11}$$

Since the velocity of the observer is very small in comparison to the velocity of sound in the medium, the v_o term in the denominator of equation (A.10) can be ignored and this equation can be re-written as equation (A.11). Equation (A.11) gives us the Doppler frequency shift detectable at the transducer when the angle of incidence (θ) is zero. However, in all practical situations this is unlikely to be the case and (A.11) becomes

$$f_D = \left(\frac{2v_o \times \cos(\theta)}{c} \right) \times f_c \tag{A.12}$$

to accommodate a non-zero value of θ. Thus equation (A.12) from classical physics theory provides the foundation for analysis of blood flow in ultrasound systems.

Appendix B

Derivation of PDFs

B.1   Derivation of AAOA and EAOA PDFs

In this appendix, we derive the closed-form solutions for the PDF in azimuth ($P(\alpha)$) and elevation ($P(\beta)$) planes given by equation (3.5) and (3.6).

B.1.1   Defining the Jacobian Transform

A Jacobian transform is an algebraic method for determining the probability density of a variable y that is a function of just one other variable x (i.e. y is a transformation of x) when we know the probability density of x. In this case, the starting point for defining the Jacobian transform is the equation of a spheroid.

$$\frac{(x^2 + y^2)}{a^2} + \frac{z^2}{b^2} = 1. \tag{B.1}$$

With consideration of figure 3.1, using simple trigonometry it is possible to derive the following expressions,

$$\cos(\psi) = \frac{x_r}{r}, x_r = \cos(\psi)r \tag{B.2}$$

$$\sin(\beta) = \frac{z_r}{r}, z_r = \sin(\beta)r \tag{B.3}$$

$$\sin(\alpha) = \frac{y_r}{r'}, y_r = \sin(\alpha)r' \tag{B.4}$$

and

$$\cos(\beta) = \frac{r'}{r}, r' = \cos(\beta)r. \tag{B.5}$$

By substituting equation (B.5) into (B.4), we get

$$y_r = \sin(\alpha)\cos(\beta)r. \tag{B.6}$$

Additionally, we know from simple trigonometry that

$$\cos(\psi) = \cos(\alpha)\cos(\beta)r. \tag{B.7}$$

Thus,

$$x_r = \cos(\alpha)\cos(\beta)r \tag{B.8}$$

$$y_r = \sin(\alpha)\cos(\beta)r \tag{B.9}$$

and

$$z_r = \sin(\beta)r. \tag{B.10}$$

By substituting equations (B.8), (B.9) and (B.10) into (B.1) we get

$$\frac{(\cos(\alpha)\cos(\beta)r)^2 + (\sin(\alpha)\cos(\beta)r)^2}{a^2} + \frac{(\sin(\beta)r)^2}{b^2} = 1. \tag{B.11}$$

If we simplify this expression this expression we get

$$\frac{r^2\cos^2(\alpha)\cos^2(\beta) + r^2\sin^2(\alpha)\cos^2(\beta)}{a^2} + \frac{r^2\sin^2(\beta)}{b^2} = 1 \tag{B.12}$$

therefore

$$\frac{r^2\cos^2(\beta)(\cos^2(\alpha) + \sin^2(\alpha))}{a^2} + \frac{r^2\sin^2(\beta)}{b^2} = 1 \tag{B.13}$$

and then substituting $(\cos^2(\alpha) + \sin^2(\alpha)) = 1$, we get

$$r^2\left[\frac{\cos^2(\beta)}{a^2} + \frac{\sin^2(\beta)}{b^2}\right] = 1. \tag{B.14}$$

If we solve (B.14) in terms of r, we get

$$r = \left[\frac{a^2 b^2}{b^2 \cos^2(\beta) + a^2 \sin^2(\beta)} \right]^{\frac{1}{2}}. \tag{B.15}$$

To derive the PDFs we make use of the Jacobian transformation. In this case, the Jacobian transform is the determinant of a 3-D matrix,

$$\frac{\partial(x_r, y_r, z_r)}{\partial(r, \beta, \alpha)} = \begin{vmatrix} x_r & x_\beta & x_\alpha \\ y_r & y_\beta & y_\alpha \\ z_r & z_\beta & z_\alpha \end{vmatrix} = \tag{B.16}$$

$$x_r \begin{bmatrix} y_\beta & y_\alpha \\ z_\beta & z_\alpha \end{bmatrix} - x_\beta \begin{bmatrix} y_r & y_\alpha \\ z_r & z_\alpha \end{bmatrix} + x_\alpha \begin{bmatrix} y_r & y_\beta \\ z_r & z_\beta \end{bmatrix}$$

where

$$x_r = \frac{\partial(x)}{\partial(r)} = \cos(\beta)cos(\alpha) \tag{B.17}$$

$$y_r = \frac{\partial(y)}{\partial(r)} = \cos(\beta)sin(\alpha) \tag{B.18}$$

$$z_r = \frac{\partial(z)}{\partial(r)} = \sin(\beta) \tag{B.19}$$

$$x_\beta = \frac{\partial(x)}{\partial(\beta)} = -r\sin(\beta)cos(\alpha) \tag{B.20}$$

$$y_\beta = \frac{\partial(y)}{\partial(\beta)} = -r\sin(\beta)sin(\alpha) \tag{B.21}$$

$$z_\beta = \frac{\partial(z)}{\partial(\beta)} = r\cos(\beta) \tag{B.22}$$

$$x_\alpha = \frac{\partial(x)}{\partial(\alpha)} = -r\cos(\beta)sin(\alpha) \tag{B.23}$$

$$y_\alpha = \frac{\partial(y)}{\partial(\alpha)} = r\cos(\beta)cos(\alpha) \tag{B.24}$$

$$z_\alpha = \frac{\partial(z)}{\partial(\alpha)} = 0 \tag{B.25}$$

Using equations (B.18) to (B.25), equation (B.16) can be re-written as

$$\frac{\partial(x_r, y_r, z_r)}{\partial(r, \beta, \alpha)} =$$

$$-r^2 \cos(\beta)(\sin^2(\alpha)\sin^2(\beta)+$$

$$\sin^2(\beta)\cos^2(alpha) + \cos^2(\alpha)\cos^2(\beta)+ \tag{B.26}$$

$$\sin^2(\alpha)\cos^2(\beta))$$

which can be simplified to

$$\frac{\partial(x_r, y_r, z_r)}{\partial(r, \beta, \alpha)} = -r^2\cos(\beta)(\sin^2(\beta) + cos^2(\beta)). \tag{B.27}$$

The Jacobian transform can therefore be taken as

$$\left|\frac{\partial(x_r, y_r, z_r)}{\partial(r, \beta, \alpha)}\right| = r^2\cos(\beta). \tag{B.28}$$

B.1.2 Defining the Joint Density Function

Now that we have the Jacobian, we need to find an expression for the joint probability density function $p(r, \beta)$. Taking the volume of a half-spheroid to be

$$V = \frac{2\pi a^2 b}{3} \tag{B.29}$$

then the joint probability density function is

$$p(r, \beta) = \frac{r^2\cos(\beta)}{V} = \frac{3r^2\cos(\beta)}{2\pi a^2 b}. \tag{B.30}$$

Integrating the joint density function with respect to r gives us the joint density in terms of α and β as shown by

$$p(\beta) = \int \frac{3r^2\cos(\beta)}{2\pi a^2 b}dr, \tag{B.31}$$

$$= \frac{3\cos(\beta)}{2\pi a^2 b}\left[\frac{1}{3}r^2\right] \tag{B.32}$$

$$p(\beta) = \frac{\cos(\beta)}{2\pi a^2 b}r^3. \tag{B.33}$$

By substituting with equation (B.15), we remove the r term and form the expression for $p(\beta)$ in of a, b and β as shown by

$$p(\beta) = \frac{\cos(\beta)}{2\pi a^2 b} \left[\frac{a^2 b^2}{b^2 \cos^2(\beta) + a^2 \sin^2(\beta)} \right]^{\frac{3}{2}} \tag{B.34}$$

which can be simplified to

$$p(\beta) = \frac{ab^2 \cos(\beta)}{2\pi (a^2 \sin^2(\beta) + b^2 \cos^2(\beta))^{\frac{3}{2}}} \tag{B.35}$$

$$0 \le \alpha \le 2\pi, 0 \le \beta \le \frac{\pi}{2}.$$

Finally, equation (B.35) can be re-worked into a more convenient form by multiplying the numerator and denominator by $\frac{1}{a^3}$, to obtain

$$p(\beta) = \frac{(\frac{b}{a})^2 \cos(\beta)}{2\pi (\sin^2(\beta) + (\frac{b}{a})^2 \cos^2(\beta))^{\frac{3}{2}}}. \tag{B.36}$$

B.1.3   Calculating the Marginal PDFs

The next step is to calculate the marginal PDFs $P_\alpha(\alpha)$ and $P_\beta(\beta)$, such that

$$p(\beta) = \int_0^{2\pi} P(\beta, \alpha) d\alpha \tag{B.37}$$

and

$$p(\alpha) = \int_0^{\frac{\pi}{2}} P(\beta, \alpha) d\beta. \tag{B.38}$$

Taking equation (B.37) and solving for $P(\beta)$ obtains

$$p(\beta) = \int_0^{2\pi} \frac{(\frac{b}{a})^2 \cos(\beta)}{2\pi (\sin^2(\beta) + (\frac{b}{a})^2 \cos^2(\beta))^{\frac{3}{2}}} d\alpha \tag{B.39}$$

$$= \frac{(\frac{b}{a})^2 \cos(\beta)}{2\pi (\sin^2(\beta) + (\frac{b}{a})^2 \cos^2(\beta))^{\frac{3}{2}}} [2\pi - 0] \tag{B.40}$$

$$= \frac{(\frac{b}{a})^2 \cos(\beta)}{(\sin^2(\beta) + (\frac{b}{a})^2 \cos^2(\beta))^{\frac{3}{2}}}. \tag{B.41}$$

Taking equation (B.38) and solving for $P(\alpha)$ obtains

$$p(\alpha) = \int_0^{\frac{\pi}{2}} \frac{(\frac{b}{a})^2 \cos(\beta)}{2\pi (\sin^2(\beta) + (\frac{b}{a})^2 \cos^2(\beta))^{\frac{3}{2}}} d\beta \tag{B.42}$$

$$= \frac{(\frac{b}{a})^2}{2\pi} \int_0^{\frac{\pi}{2}} \frac{\cos(\beta)}{(\sin^2(\beta)+(\frac{b}{a})^2 \cos^2(\beta))^{\frac{3}{2}}} d\beta \tag{B.43}$$

$$= \left[\frac{(\frac{b}{a})^2}{2\pi} \cdot \frac{\sqrt{2}a^2 \sin(\beta)}{b^2 \sqrt{\frac{(b^2-a^2)\cos(2\beta)+a^2+b^2}{a^2}}} \right]_0^{\frac{\pi}{2}} = \frac{1}{2\pi}. \tag{B.44}$$

Thus, in the azimuth plane, the PDF $P_\alpha(\alpha)$ is

$$p(\alpha) = \frac{1}{2\pi}, 0 \le \alpha \le 2\pi \tag{B.45}$$

and in the elevation plane, the PDF $P_\beta(\beta)$ is

$$p(\beta) = \frac{(\frac{b}{a})^2 \cos(\beta)}{(\sin^2(\beta) + (\frac{b}{a})^2 \cos^2(\beta))^{\frac{3}{2}}}, 0 \le \beta \le \frac{\pi}{2}. \tag{B.46}$$

B.2   Derivation of Amplitude PDFs

In this section, we describe the closed-form solutions for the amplitude PDFs of the envelopes $\hat{\xi}(t)$ and $\hat{\zeta}(t)$ used in the isotropic and non-isotropic simulation models respectively, and referenced by equations (3.35) and (4.28).

The amplitude PDF $\hat{p}_{\hat{\xi}}(z)$ of the envelope of a *Rician* process under LoS conditions is defined in [53], [68] and [71], and can be expressed as

$$\hat{p}_{\hat{\xi}}(z) = (2\pi)^2 z \int_0^\infty \left[\prod_{n=1}^N J_0 \left(2\pi|C_n|x\right) \right] J_0 \left(2\pi zx\right) J_0 \left(2\pi K_0 x\right) x dx \tag{B.47}$$

where $J_0(.)$ denotes the zeroth-order Bessel function of the first kind and $z \ge 0$. In (B.47) N is the number of incident scatterers and C_n is the gain associated with each scatterer. By choosing $C_n = \sigma_0 \sqrt{2/N}$ where $(\sigma_0^2 = 1)$ $\hat{p}_{\hat{\xi}}(z)$ becomes

$$\hat{p}_{\hat{\xi}}(z) = (2\pi)^2 z \int_0^\infty e^{-2(\pi\sigma_0 x)^2} J_0 \left(2\pi zx\right) J_0 \left(2\pi K_0 x\right) x dx. \tag{B.48}$$

Simplifying (B.48) using the definition at 6.626.1 p.704 of [63] results in

$$\hat{p}_\xi(z) = \frac{z}{\sigma_o^2} e^{-\frac{z^2+K_0^2}{2\sigma_0^2}} I_0 \left(\frac{zK_0}{\sigma_0^2} \right), z \ge 0 \tag{B.49}$$

where z is the amplitude variable, I_o is the zeroth order modified Bessel function of the first kind, $K_0 = \sqrt{\frac{K}{K+1}}$, where K is the *Rician* K-factor, and the variance of $\mu(t)$ is given by $\mathrm{Var}\{\mu(t)\} = 2\sigma_0^2$.

Furthermore, from (B.48) it is straight forward to derive the amplitude PDF $\hat{p}_{\hat{\zeta}}(t)$ of the envelope of a *Rayleigh* process. This is obtained by allowing the LoS component $K_0 \to 0$ and is given by

$$\hat{p}_{\hat{\zeta}}(z) = (2\pi)^2 \, z \int_0^\infty \left[\prod_{n=1}^N J_0\left(2\pi|C_n|x\right) \right] J_0\left(2\pi z x\right) x \mathrm{d}x. \tag{B.50}$$

As $K_0 \to 0$ and choosing $C_n = \sigma_0\sqrt{2/N}$ where $(\sigma_0^2 = 1)$, (B.50) can be simplified to obtain

$$\hat{p}_{\hat{\zeta}}(z) = \frac{z}{\sigma_o^2} e^{-\frac{z^2}{2\sigma_0^2}}, z \geq 0. \tag{B.51}$$

Appendix C

Derivation of the 3-D Isotropic TCD Ultrasound Propagation Channel Model ACF

If received signal of a flat fading channel is given by the delayed version of that signal multiplied by a complex-valued stochastic process $\mu(t)$ [53], then

$$\mu(t) = \sum_{n=1}^{N} C_n e^{j\theta_n(t)}. \tag{C.1}$$

In (C.1), as $N \to \infty$ the central limit theorem may be invoked such that

$$\mu(t) = \lim_{N \to \infty} \sum_{n=1}^{N} C_n e^{j\theta_n(t)}. \tag{C.2}$$

This zero-mean complex valued random *Gaussian* process can be expressed in terms of it's in-phase and quadrature components as

$$\mu(t) = \mu_1(t) + j\mu_2(t). \tag{C.3}$$

In (C.3), it can be assumed that $\mu_1(t)$ and $\mu_2(t)$ are statistically uncorrelated and have equal variances, such that $Var\{\mu_i(t)\} = \sigma_0^2$ for $i = 1, 2$, and the *Rayleigh*

process $\zeta(t)$ can therefore be denoted as

$$\zeta(t) = |\mu(t)| = |\mu_1(t) + j\mu_2(t)| \tag{C.4}$$

The autocorrelation function $r_{\mu\mu}(t)$ is, therefore, a measure of the variation of the complex received signal $\mu(t)$ with time and is defined as the ensemble average of the product of $\mu(t)$ with itself at time separation τ. Thus we have

$$r_{\mu\mu}(\tau) = E[\mu^*(t)\mu(t+\tau)] \tag{C.5}$$

where E[$\cdot$] is the ensemble average operator.

In (C.2), it can be assumed that the phases $\theta_n(t)$ are statistically independent random variables at any time t, since the path delays τ_n associated with each scatterer are all independent due to their random placement. Further, the phases $\theta_n(t)$ at any time t can be treated as being uniformly distributed over the interval $[-\pi, \pi]$. The azimuth and elevation angles of arrival, α and β are independent due to the random placement of scatterers. In the limit as $N \to \infty$, the discrete azimuth angles of arrival α_n and β_n can be replaced by the continuous random variables α and β having the probability density functions $p(\alpha)$ and $p(\beta)$ respectively, as defined in Appendix B.1. The ACF $r_{\mu\mu}$ can therefore be obtained as

$$
\begin{aligned}
r_{\mu\mu}(\tau) &= \lim_{N \to \infty} E_{\tau,\theta}\left[\mu^*(t)\mu(t-\tau)\right] \\
&= \frac{\Omega_p}{2} E_{\theta_n}\left[cos(2\pi f_{D_{max}}\tau \cos(\alpha_n)\cos(\beta_n))\right]
\end{aligned}
\tag{C.6}
$$

where

$$\tau = (\tau_1, \tau_2, ..., \tau_n) \tag{C.7}$$

$$\theta = (\theta_1, \theta_2, ..., \theta_n) \tag{C.8}$$

$$\Omega_p = \sum_{n=1}^{N} C_n^2. \tag{C.9}$$

In equation (C.9), Ω_p can be interpreted as the total received envelope power.

As shown in [54] for the 2-D case based on *Clarke's* model and similarly in the 3-D isotropic scattering case, the evaluation of the expectations shown in (C.6) requires the distribution of the arriving plane waves in azimuth $(p(\alpha))$ and elevation $(p(\beta))$ to be defined. An assumption is made that plane waves will arrive from all directions in azimuth and elevation with equal probability, a transducer gain of $G_{\alpha,\beta}(\theta) = 1$ for $\theta \in (0, 2\pi)$, and normalised such that $\Omega_p = 2$.

Taking the marginal PDFs derived in equations (B.45) and (B.46), the temporal ACF of the uncorrelated in-phase and quadrature components of the complex received signal $\mu(t)$ is obtained as

$$r_{\mu\mu}(\tau) = \int_0^{\frac{\pi}{2}} \int_0^{2\pi} e^{j2\pi f_{Dmax}\tau\cos(\alpha)\cos(\beta)} p(\alpha)p(\beta)\mathrm{d}\alpha\mathrm{d}\beta. \tag{C.10}$$

This can be simplified further by substituting equation (B.45) and (B.46) into (C.7), such that

$$r_{\mu\mu}(\tau) = \frac{1}{2\pi} \int_0^{\frac{\pi}{2}} e^{j2\pi f_{Dmax}\tau\cos(\alpha)\cos(\beta)} \cdot \frac{\left(\frac{b}{a}\right)^2\cos(\beta)}{\left[\sin^2(\beta) + \left(\frac{b}{a}\right)^2\cos^2(\beta)\right]^{\frac{3}{2}}}\mathrm{d}\beta. \tag{C.11}$$

Equation (C.11) can be simplified further to obtain

$$r_{\mu\mu}(\tau) = \int_0^{\frac{\pi}{2}} J_0\left(2\pi f_{Dmax}\tau\cos(\beta)\right) \cdot \left[\frac{\left(\frac{b}{a}\right)^2\cos(\beta)}{\left[\sin^2(\beta) + \left(\frac{b}{a}\right)^2\cos^2(\beta)\right]^{\frac{3}{2}}}\right]\mathrm{d}\beta \tag{C.12}$$

where

$$J_0(z) = \frac{1}{2\pi}\int_0^{2\pi} e^{jz\cos(\theta)}d\theta \tag{C.13}$$

is the zero-order Bessel function of the first kind.

Appendix D

Derivation of the Coordinates System and VMF Distribution

In Fig. 4.1 the rectangular and spherical coordinates of an incident scatterer S_n are plotted in three-dimensional spherical space ($\rho = 3$) in a reference model. Since the number of local scatterers in the reference model is infinite, the discrete azimuth angle of arrival (AAoA) α_n and elevation angle of arrival (EAoA) β_n can be replaced with continuous random variables α and β with a joint probability density given by

$$P(\tau) = \int_{-\frac{\pi}{2}}^{\frac{\pi}{2}} \int_{-\pi}^{\pi} e^{j2\pi\tau f_{max} \cos\alpha \cos\beta} \mathrm{d}\alpha \mathrm{d}\beta \qquad (D.1)$$

In order to remove the unrealistic assumption that the azimuth and elevation angles are independent, the VMF distribution can be used to characterise the scattering distribution.

Taking the rectangular coordinate plots we can state that

$$d^2 = x^2 + y^2 \qquad (D.2)$$

$$r^2 = d^2 + z^2 \qquad (D.3)$$

therefore

$$r^2 = x^2 + y^2 + z^2. \qquad (D.4)$$

and hence

$$x = d \cos \alpha \tag{D.5}$$

$$y = d \sin \alpha \tag{D.6}$$

$$z = r \cos \beta \tag{D.7}$$

$$d = r \sin \beta. \tag{D.8}$$

Using these expressions and assuming a unit sphere $(r = 1)$, we can describe the rectangular coordinates $[x, y, z]$ in terms of the longitude and colatitude; where longitude is the angular measure in a counter-clockwise sense from the x-axis denoted by α and colatitude is the angular measure from the z-axis denoted by β.

$$x = r \cos \alpha \cos \beta = \cos \alpha \cos \beta \tag{D.9}$$

$$y = r \sin \alpha \sin \beta = \sin \alpha \sin \beta \tag{D.10}$$

$$z = r \cos \beta = \cos \beta. \tag{D.11}$$

Further, if we consider a unit random vector $\mathbf{x}$ and a mean direction vector $\boldsymbol{\mu}$ using a spherical coordinate system

$$\mathbf{x} = (\cos \alpha \sin \beta, \sin \alpha \sin \beta, \cos \beta)^T \tag{D.12}$$

$$\boldsymbol{\mu} = (\cos \alpha_0 \sin \beta_0, \sin \alpha_0 \sin \beta_0, \cos \beta_0)^T \tag{D.13}$$

then

$$\boldsymbol{\mu}^T \mathbf{x} = \mathbf{x}^T \boldsymbol{\mu}$$

$$= \begin{bmatrix} \cos \alpha \sin \beta \\ \sin \alpha \sin \beta \\ \cos \beta \end{bmatrix} \cdot [\cos \alpha_0 \sin \beta_0, \sin \alpha_0 \sin \beta_0, \cos \beta_0]$$

$$\boldsymbol{\mu}^T \mathbf{x} = \cos \beta \cos \beta_0 + \sin \beta \sin \beta_0 \cos (\alpha - \alpha_0). \tag{D.14}$$

It is known that if $\mathbf{x}$ is a random unit vector distributed in sample space $S^{\rho-1}$ when $(\rho = 3)$, then (α, β) has a PDF given by

$$P(\alpha, \beta) = \frac{1}{4\pi}\cos\beta, \{0 \leq \alpha \leq \pi\}, \{0 \leq \beta \leq 2\pi\}. \tag{D.15}$$

If we now consider the VMF distribution given by $F(\mu, k)$ such that

$$F(\mu, k) = \frac{k}{\sinh k}e^{k[\boldsymbol{\mu}^T\mathbf{x}]} \tag{D.16}$$

then the probability density of a random unit vector using the VMF distribution in sample space S^2 is given by

$$\begin{aligned}
f(\alpha, \beta) &= \frac{k}{4\pi\sinh k}e^{k[\boldsymbol{\mu}^T\mathbf{x}]}\cos\beta \\
&= \frac{k}{4\pi\sinh k}e^{k[\cos\beta\cos\beta_0 + \sin\beta\sin\beta_0\cos(\alpha-\alpha_0)]}\cos\beta.
\end{aligned} \tag{D.17}$$

In (D.17), α_0 and β_0 define the mean direction and k is the concentration parameter that controls the distribution relative to the mean direction.

Appendix E

Derivation of the Non-isotropic Simulation Model *Doppler* Shift and Spread

In this appendix, we derive the closed-form solutions for the *Doppler* shift $\hat{B}_{\hat{\mu}\hat{\mu}}^{(1)}$ and *Doppler* spread $\hat{B}_{\hat{\mu}\hat{\mu}}^{(2)}$ for the non-isotropic simulation model described in section 4.3.2.3.

The *Doppler* shift $B_{\hat{\mu}\hat{\mu}}^{(1)}$ is given by

$$
\begin{aligned}
B_{\hat{\mu}\hat{\mu}}^{(1)} &= \frac{\int_{-\infty}^{\infty} f S_{\hat{\mu}\hat{\mu}}(f)\, df}{\int_{-\infty}^{\infty} S_{\hat{\mu}\hat{\mu}}(f)\, df} \\
&= \frac{1}{2\pi j} \cdot \frac{\dot{\hat{r}}_{\hat{\mu}\hat{\mu}}(0)}{\hat{r}_{\hat{\mu}\hat{\mu}}(0)}.
\end{aligned}
\tag{E.1}
$$

Appendix E. Derivation of the Non-isotropic Simulation Model Doppler Shift and Spread

The *Doppler* spread $B_{\hat{\mu}\hat{\mu}}^{(2)}$ is given by

$$
\begin{aligned}
B_{\hat{\mu}\hat{\mu}}^{(2)} &= \sqrt{\frac{\int_{-\infty}^{\infty} \left(f - B_{\hat{\mu}\hat{\mu}}^{(1)}\right) S_{\hat{\mu}\hat{\mu}}(f)\, df}{\int_{-\infty}^{\infty} S_{\hat{\mu}\hat{\mu}}(f)\, df}} \\
&= \frac{1}{2\pi} \sqrt{\left(\frac{\dot{\hat{r}}_{\hat{\mu}\hat{\mu}}(0)}{\hat{r}_{\hat{\mu}\hat{\mu}}(0)}\right)^2 - \frac{\ddot{\hat{r}}_{\hat{\mu}\hat{\mu}}(0)}{\hat{r}_{\hat{\mu}\hat{\mu}}(0)}} \\
&= \frac{1}{2\pi} \sqrt{\left(2\pi j \cdot B_{\hat{\mu}\hat{\mu}}^{(1)}\right)^2 - \frac{\ddot{\hat{r}}_{\hat{\mu}\hat{\mu}}(0)}{\hat{r}_{\hat{\mu}\hat{\mu}}(0)}} \\
&= \sqrt{-\left(B_{\hat{\mu}\hat{\mu}}^{(1)}\right)^2 - \frac{\ddot{\hat{r}}_{\hat{\mu}\hat{\mu}}(0)}{\hat{r}_{\hat{\mu}\hat{\mu}}(0)}}
\end{aligned}
\tag{E.2}
$$

where (E.1) and (E.2) can be further simplified by investigating the first and second derivatives of the normalised ACF, $\hat{r}_{\hat{\mu}\hat{\mu}}(\tau)$.

$$
\begin{aligned}
\hat{r}_{\hat{\mu}\hat{\mu}}(\tau) &= \frac{K}{(K+1)} e^{j2\pi f_{D_{\max}}\tau \cos\alpha_0 \cos\beta_0} + \\
&\quad \frac{1}{(K+1)} \sum_{n=1}^{N} \frac{1}{N} e^{j2\pi f_{D_{\max}}\tau \cos\alpha_n \cos\beta_n} \\
\hat{r}_{\hat{\mu}\hat{\mu}}(0) &= \frac{K}{(K+1)} + \frac{1}{(K+1)} = 1.
\end{aligned}
\tag{E.3}
$$

therefore

$$
\dot{\hat{r}}_{\hat{\mu}\hat{\mu}}(0) = \frac{2\pi j f_{D_{\max}}}{(K+1)} \times \left[K \cos\alpha_0 \cos\beta_0 + \sum_{n=1}^{N} \frac{1}{N} \cos\alpha_n \cos\beta_n\right]
\tag{E.4}
$$

and

$$
\ddot{\hat{r}}_{\hat{\mu}\hat{\mu}}(0) = \frac{-(2\pi f_{D_{\max}})^2}{(K+1)} \times \left[K (\cos\alpha_0 \cos\beta_0)^2 + \sum_{n=1}^{N} \frac{1}{N} (\cos\alpha_n \cos\beta_n)^2\right]
\tag{E.5}
$$

Through substitution of (E.3), (E.4) and (E.5) back into (E.1)

$$
\hat{B}_{\hat{\mu}\hat{\mu}}^{(1)} = \frac{f_{D_{\max}}}{(K+1)} \times \left[K \cos\alpha_0 \cos\beta_0 + \sum_{n=1}^{N} \frac{1}{N} \cos\alpha_n \cos\beta_n\right]
\tag{E.6}
$$

and

$$
\hat{B}_{\hat{\mu}\hat{\mu}}^{(2)} = \sqrt{-\ddot{\hat{r}}_{\hat{\mu}\hat{\mu}}(0) - \left(\hat{B}_{\hat{\mu}\hat{\mu}}^{(1)}\right)^2}.
\tag{E.7}
$$

Bibliography

[1] J. Mackay, G. A. Mensah, S. Mendis, and K. Greenlund, *The Atlas of Heart Disease and Stroke.* Geneva, Switzerland: World Health Organisation, 2004.

[2] D. MacNiven, *Scotland's Population 2009.* Edinburgh, UK: Official Print Publication SG/2010/95, 2010.

[3] J. Olesen, A. Gustavsson, M. Svensson, H.-U. Wittchen, and B. Jönsson, "The economic cost of brain disorders in europe," *European J. of Neurology*, vol. 19, no. 1, pp. 155–162, 2012.

[4] A. Morse and A. General, *Progress in Improving Stroke Care.* London, UK: TSO, 2010.

[5] P. A. Committee *et al.*, "Reducing brain damage: Faster access to better stroke care," *London, UK: Government 52nd Report of Session*, vol. 6, 2005.

[6] R. Aaslid, T.-M. Markwalder, and H. Nornes, "Noninvasive transcranial doppler ultrasound recording of flow velocity in basal cerebral arteries," *J. of Neurosurgery*, vol. 57, no. 6, pp. 769–774, 1982.

[7] D. H. Evans and W. N. McDicken, *Doppler ultrasound: Physics, instrumentation, and clinical applications, second edition.* Chichester, UK: John Wiley & Sons, 1989.

[8] S. Satomura and Z. Kaneko, "Ultrasonic blood rheograph," in *Proc. of IEEE 3rd Int. Conf. on Medical Electron.* London, UK, Jul. 1960, pp. 254–258.

[9] J. Webster, *Medical Instrumentation: Application & Design.* New York: John Wiley & Sons, 2009.

[10] P. Wells, "Ultrasonic colour flow imaging," *Physics in medicine and biology*, vol. 39, no. 12, p. 2113, 1994.

[11] J. A. Davis, D. W. Inglis, K. J. Morton, D. A. Lawrence, L. R. Huang, S. Y. Chou, J. C. Sturm, and R. H. Austin, "Deterministic hydrodynamics: taking blood apart," *Proc. of the Nat. Academy of Sciences*, vol. 103, no. 40, pp. 14 779–14 784, 2006.

[12] H. S. Markus, "Transcranial doppler ultrasound," *J. of Neurology, Neurosurgery & Psychiatry*, vol. 67, no. 2, pp. 135–137, 1999.

[13] L. Sandra, W. J. Z. Hagen-Ansert, and S. RDM, *Textbook of diagnostic ultrasonography.* St Louis, Missouri: Elsevier Health Sciences, 2006.

[14] J. Molloy, N. Khan, and H. S. Markus, "Temporal variability of asymptomatic embolization in carotid artery stenosis and optimal recording protocols," *Stroke*, vol. 29, no. 6, pp. 1129–1132, 1998.

[15] A. D. Mackinnon, R. Aaslid, and H. S. Markus, "Ambulatory transcranial doppler cerebral embolic signal detection in symptomatic and asymptomatic carotid stenosis," *Stroke*, vol. 36, no. 8, pp. 1726–1730, 2005.

[16] J.-M. Girault, D. Kouamé, A. Ouahabi, and F. Patat, "Micro-emboli detection: an ultrasound doppler signal processing viewpoint," *IEEE Trans. Biomed. Eng.*, vol. 47, no. 11, pp. 1431–1439, 2000.

[17] J. L. Smith, D. H. Evans, L. Fan, P. R. Bell, and A. R. Naylor, "Differentiation between emboli and artefacts using dual-gated transcranial doppler ultrasound," *Ultrasound in Medicine & Biology*, vol. 22, no. 8, pp. 1031–1036, 1996.

[18] M. A. Moehring and J. R. Klepper, "Pulse doppler ultrasound detection, characterization and size estimation of emboli in flowing blood," *IEEE Trans. Biomed. Eng.*, vol. 41, no. 1, pp. 35–44, 1994.

[19] M. A. Moehring, M. P. Spencer, D. L. Davis, and R. P. Demuth, "Exploration of the embolus to blood power ratio model (ebr) for characterizing microemboli

detected in the middle cerebral artery," in *Proc. of IEEE Ultrasonics Symp.*, vol. 2.   Seattle, USA, 1995, pp. 1531–1535.

[20] M. A. Moehring, "Fundamental concepts regarding sizing and discrimination of air bubbles and red cell aggregates using pulsed-doppler ultrasound," *Echocardiography*, vol. 13, no. 5, pp. 567–572, 1996.

[21] H. S. Markus and J. Molloy, "Use of a decibel threshold in detecting doppler embolic signals," *Stroke*, vol. 28, no. 4, pp. 692–695, 1997.

[22] E. Wigner, "On the quantum correction for thermodynamic equilibrium," *Physical review*, vol. 40, no. 5, p. 749, 1932.

[23] E. Chassande-Mottin, A. Pai *et al.*, "Discrete time and frequency wigner-ville distribution: Moyal's formula and aliasing," *IEEE Signal Process. Lett.*, vol. 12, no. 7, p. 508, 2005.

[24] J. Smith, D. Evans, L. Fan, A. Thrush, and A. Naylor, "Processing doppler ultrasound signals from blood-borne emboli," *Ultrasound in Medicine & Biology*, vol. 20, no. 5, pp. 455–462, 1994.

[25] C. Banahan, Z. Rogerson, C. Rousseau, K. V. Ramnarine, D. H. Evans, and E. M. Chung, "An in vitro comparison of embolus differentiation techniques for clinically significant macroemboli: dual-frequency technique versus frequency modulation method," *Ultrasound in medicine & biology*, vol. 40, no. 11, pp. 2642–2654, 2014.

[26] C. Guetbi, D. Kouame, A. Ouahabi, and J. Remenieras, "New emboli detection methods [doppler ultrasound]," in *Proc. of IEEE Ultrasonics Symp.*, vol. 2. Toronto, Canada, 1997, pp. 1119–1122.

[27] N. Aydin, S. Padayachee, and H. S. Markus, "The use of the wavelet transform to describe embolic signals," *Ultrasound in Medicine & Biology*, vol. 25, no. 6, pp. 953–958, 1999.

[28] S. G. Mallat, "A theory for multiresolution signal decomposition: the wavelet representation," *IEEE Trans. Pattern Anal. Mach. Intell.*, vol. 11, no. 7, pp. 674–693, 1989.

[29] S. Marvasti, D. Gillies, and H. S. Markus, "Novel intelligent wavelet filtering of embolic signals from tcd ultrasound," in *Proc. of IEEE Signals, Syst. and Comput.*, vol. 2. Pacific Grove, California, USA, 2004, pp. 1580–1584.

[30] S. Marvasti, M. Ghandi, F. Marvasti, H. S. Markus, and D. Gillies, "Multiple wavelet denoising for embolic signal enhancement," in *Proc. of IEEE Conf. on Telecommun. and Malaysia Int. Conf. on Commun. (ICT-MICC)*. Penang, Malaysia, 2007, pp. 658–664.

[31] J. Cowe, J. Gittins, and D. H. Evans, "Improving performance of pulse compression in a doppler ultrasound system using amplitude modulated chirps and wiener filtering," *Ultrasound in Medicine & Biology*, vol. 34, no. 2, pp. 326–333, 2008.

[32] J. Cowe, E. Boni, S. Ricci, P. Tortoli, and D. Evans, "Coded excitation can provide simultaneous improvements in sensitivity and axial resolution in doppler ultrasound systems," in *Proc. of IEEE Ultrasonics Symp. (IUS)*. San Diego, USA, Oct. 2010, pp. 2286–2290.

[33] X. Lei, Z. Heng, and G. Shangkai, "Barker code in tcd ultrasound systems to improve the sensitivity of emboli detection," *Ultrasound in Medicine & Biology*, vol. 35, no. 1, pp. 94–101, 2009.

[34] J. Li, X. Diao, K. Zhan, and Z. Qin, "A full digital design of tcd ultrasound system using normal pulse and coded excitation," in *Proc. of 1st Global Conf. on Biomedical Eng. & 9th Asian-Pacific on Medical and Biological Eng. (APCMBE)*. Tainan, Taiwan, Oct. 2014, pp. 136–139.

[35] I. Genesis, "The early history of pulse compression radar," *IEEE Trans. Aerosp. Electron. Syst.*, vol. 24, no. 6, p. 825, 1988.

[36] Y. Takeuchi, "An investigation of a spread energy method for medical ultrasound systems: Part one: Theory and investigation," *Ultrasonics*, vol. 17, no. 4, pp. 175–182, 1979.

[37] Y. Takeuchi, "An investigation of a spread energy method for medical ultrasound systems: Part two: proposed system and possible problems," *Ultrasonics*, vol. 17, no. 5, pp. 219–224, 1979.

[38] M. O'Donnell, "Coded excitation system for improving the penetration of real-time phased-array imaging systems," *IEEE Trans. Ultrason. Ferroelectr. Freq. Control*, vol. 39, no. 3, pp. 341–351, 1992.

[39] R. Y. Chiao and X. Hao, "Coded excitation for diagnostic ultrasound: a system developer's perspective," in *Proc. of IEEE Ultrasonics Symp.*, vol. 1. Hawaii, USA, 2003, pp. 437–448.

[40] J. Gu and Y. Jing, "Modeling of wave propagation for medical ultrasound: a review," *IEEE Trans. Ultrason. Ferroelectr. Freq. Control*, vol. 62, no. 11, pp. 1979–1992, 2015.

[41] P. J. Westervelt, "Parametric acoustic array," *J. of the Acoust. Soc. of America*, vol. 35, no. 4, pp. 535–537, 1963.

[42] B. E. Treeby, J. Jaros, A. P. Rendell, and B. Cox, "Modeling nonlinear ultrasound propagation in heterogeneous media with power law absorption using a k-space pseudospectral method," *J. of the Acoust. Soc. of America*, vol. 131, no. 6, pp. 4324–4336, 2012.

[43] M. J. Crocker, *Handbook of acoustics*. New York: John Wiley & Sons, 1998.

[44] Y. Zhou, *Principles and Applications of Therapeutic Ultrasound in Healthcare*. Boca Raton, Florida: CRC Press, 2015.

[45] P. D. Fox, A. Bouakaz, and F. Tranquart, "Computation of steered nonlinear fields using offset kzk axes," in *Proc. of IEEE Ultrasonics Symp. (IUS)*, vol. 4. Rotterdam, The Netherlands, Sept. 2005, pp. 1984–1987.

[46] W. F. Walker and G. E. Trahey, "The application of k-space in medical ultrasound," in *Proc. of IEEE Ultrasonics Symp. (IUS)*, vol. 2. Rotterdam, The Netherlands, Nov. 1995, pp. 1379–1383.

[47] W. F. Walker and G. E. Trahey, "The application of k-space in pulse echo ultrasound," *IEEE Trans. Ultrason. Ferroelectr. Freq. Control*, vol. 45, no. 3, pp. 541–558, 1998.

[48] Y. Jing, T. Wang, and G. T. Clement, "A k-space method for moderately nonlinear wave propagation," *IEEE Trans. Ultrason. Ferroelectr. Freq. Control*, vol. 59, no. 8, pp. 1664–1673, 2012.

[49] M. E. Anderson and G. E. Trahey, "A seminar on k-space applied to medical ultrasound," *Department of Biomedical Engineering, Duke University*, 2000.

[50] Z. Guan, E. Santagati, and T. Melodia, "Ultrasonic intra-body networking: Interference modeling, stochastic channel access and rate control," in *Proc. of IEEE Conf. on Comput. Commun. (INFOCOM)*. Hong Kong, China, Apr. 2015, pp. 2425–2433.

[51] Z. Guan, G. E. Santagati, and T. Melodia, "Distributed algorithms for joint channel access and rate control in ultrasonic intra-body networks," *IEEE/ACM Trans. Netw.*, vol. PP, no. 99, pp. 1–1, 2016.

[52] M. Nakagami, "The m-distribution-a general formula of intensity distribution of rapid fading," *Statistical Method of Radio Propagation*, 1960.

[53] M. Pätzold, *Mobile radio channels*. New York: John Wiley & Sons, 2011.

[54] G. L. Stüber, *Principles of mobile communication*. New York: Springer Science & Business Media, 2011.

[55] S. O. Rice, "Mathematical analysis of random noise," *Bell Syst. Tech. J.*, vol. 24, no. 1, pp. 46–156, 1945.

[56] W. C. Jakes and D. C. Cox, *Microwave mobile communications*. Wiley-IEEE Press, 1994.

[57] R. Clarke, "A statistical theory of mobile-radio reception," *Bell Syst. Tech. J.*, vol. 47, no. 6, pp. 957–1000, 1968.

[58] T. Aulin, "A modified model for the fading signal at a mobile radio channel," *IEEE Trans. Veh. Technol.*, vol. 28, no. 3, pp. 182–203, 1979.

[59] Q. Yao and M. Pätzold, "A novel 3-D spatial-temporal deterministic simulation model for mobile fading channels," in *Proc. of IEEE 14th Proc. on Personal, Indoor and Mobile Radio Commun. (PIMRC)*, vol. 2. Beijing, China, 2003, pp. 1506–1510.

[60] R. Janaswamy, "Angle of arrival statistics for a 3-D spheroid model," *IEEE Trans. Veh. Technol.*, vol. 51, no. 5, pp. 1242–1247, 2002.

[61] Q. Yao and M. Pätzold, "Spatial-temporal characteristics of a half-spheroid model and its corresponding simulation model," in *Proc. of IEEE 59th Veh. Technol. Conf. (VTC)*, vol. 1. Milan, Italy, Sept. 2004, pp. 147–151.

[62] A. Weir, C.-X. Wang, and S. Parks, "3-d half-spheroid models for transcranial doppler ultrasound propagation channels," in *Proc. of IEEE-EMBS Int. Conf. on Biomedical & Health Informatics (BHI)*. Valencia, Spain, 2014, pp. 728–731.

[63] I. Gradshteyn and I. Ryzhik, *Table of Integrals, Series and Products (Corrected and Enlarged Edition prepared by A. Jeffrey and D. Zwillinger)*. New York: Academic Press, 2000.

[64] M. Patzold, U. Killat, F. Laue, and Y. Li, "A new and optimal method for the derivation of deterministic simulation models for mobile radio channels," in *Proc. of IEEE 46th Veh. Technol. Conf. (VTC)*, vol. 3. Atlanta, USA, 1996, pp. 1423–1427.

[65] X. Cheng, C.-X. Wang, Y. Yuan, D. Laurenson, and X. Ge, "A novel 3d regular-shaped geometry-based stochastic model for non-isotropic mimo mobile-to-mobile channels," in *Proc. of IEEE 72nd Veh. Technol. Conf. (VTC)*. Ottawa, Canada, Sept. 2010, pp. 1–5.

[66] A. G. Zajić and G. L. Stüber, "Three-dimensional modeling, simulation, and capacity analysis of space–time correlated mobile-to-mobile channels," *IEEE Trans. Veh. Technol.*, vol. 57, no. 4, pp. 2042–2054, 2008.

[67] A. G. Zajić and G. L. Stüber, "Three-dimensional modeling and simulation of wideband mimo mobile-to-mobile channels," *IEEE Trans. Wireless Commun.*, vol. 8, no. 3, pp. 1260–1275, 2009.

[68] Y. Yuan, C.-X. Wang, X. Cheng, B. Ai, D. Laurenson *et al.*, "Novel 3d geometry-based stochastic models for non-isotropic mimo vehicle-to-vehicle channels," *IEEE Trans. Wireless Commun.*, vol. 13, no. 1, pp. 298–309, 2014.

[69] E. Batschelet, *Circular statistics in biology.* London, UK: Academic press, 1981.

[70] K. V. Mardia and P. E. Jupp, *Directional statistics.* New York: John Wiley & Sons, 2009.

[71] M. Pätzold and B. Talha, "On the statistical properties of sum-of-cisoids based mobile radio channel models," in *Proc. of the 10th Int. Symp. on Wireless Personal Multimedia Commun., (WPMC).* Jaipur, India, Dec. 2007, pp. 394–400.

[72] A. G. Zajic, G. L. Stüber, T. G. Pratt, and S. Nguyen, "Envelope level crossing rate and average fade duration in mobile-to-mobile fading channels," in *Proc. of IEEE Int. Conf. on Commun. (ICC).* Beijing, China, 2008, pp. 4446–4450.

[73] M. K. Simon, *Probability distributions involving Gaussian random variables: A handbook for engineers and scientists.* New York: Springer Science & Business Media, 2007.

[74] P. R. Hoskins, "Simulation and validation of arterial ultrasound imaging and blood flow," *Ultrasound in Medicine & Biology*, vol. 34, no. 5, pp. 693–717, 2008.

[75] K. Surry, H. Austin, A. Fenster, and T. Peters, "Poly (vinyl alcohol) cryogel phantoms for use in ultrasound and mr imaging," *Physics in Medicine and Biology*, vol. 49, no. 24, p. 5529, 2004.

[76] I. E. Commission *et al.*, *Ultrasonics: Flow Measurement Systems; Flow Test Object; International Standard*. Geneva, Switzerland: International Electrotechnical Commission, 2001.

[77] J. Browne, K. Ramnarine, A. Watson, and P. Hoskins, "Assessment of the acoustic properties of common tissue-mimicking test phantoms," *Ultrasound in Medicine & Biology*, vol. 29, no. 7, pp. 1053–1060, 2003.

[78] N. Bilaniuk and G. S. Wong, "Speed of sound in pure water as a function of temperature," *J. of the Acoust. Soc. of America*, vol. 93, no. 3, pp. 1609–1612, 1993.

[79] X. Chen, D. Phillips, K. Q. Schwarz, J. G. Mottley, and K. J. Parker, "The measurement of backscatter coefficient from a broadband pulse-echo system: a new formulation," *IEEE Trans. Ultrason. Ferroelectr. Freq. Control*, vol. 44, no. 2, pp. 515–525, 1997.

[80] M. A. Moehring and M. P. Spencer, "Power m-mode doppler (pmd) for observing cerebral blood flow and tracking emboli," *Ultrasound in Medicine & Biology*, vol. 28, no. 1, pp. 49–57, 2002.

[81] F. Caldicott, *Information: To share or not to share. Information Governance Review*. London UK: Department of Health, 2013.

[82] N. T. Nguyen, G. Zheng, Z. Han, and R. Zheng, "Device fingerprinting to enhance wireless security using nonparametric bayesian method," in *Proc. of IEEE Int. Conf. on Comput. Commun. (INFOCOM)*. Shanghai, China, 2011, pp. 1404–1412.